This is to certify that the
dissertation entitled

Magnetic Scattering in Dilute AgFe Kondo Wires Below the Kondo Temperature

presented by

Gassem Mohammad Alzoubi

has been accepted towards fulfillment
of the requirements for the

Ph.D degree in Physics and Astronomy

Norman O. Birge

Major Professor's Signature

June 19, 2007

Date

Magnetic Scattering in Dilute AgFe Kondo Wires Below the Kondo Temperature

By

Gassem Mohammad Alzoubi

A DISSERTATION

Submitted to
Michigan State University
in partial fulfillment of the requirements
for the Degree of

DOCTOR OF PHILOSOPHY

Department of Physics and Astronomy

2007

ABSTRACT

Magnetic Scattering in Dilute AgFe Kondo Wires Below the Kondo Temperature

By

Gassem Mohammad Alzoubi

The scattering of conduction electrons by magnetic impurities is known as the Kondo effect. In metals, the resistivity normally decreases monotonically with decreasing temperature and reaches a constant residual value at zero temperature. In some cases, a minimum was observed in the resistivity at low temperature. This minimum was attributed to the presence of dilute magnetic impurities in the metal host. In this thesis, we discuss the effect of scattering of conduction electrons by Fe magnetic impurities in AgFe Kondo wires.

In a metal containing a small amount of magnetic impurities, the resistivity is proportional to the total scattering rate, which increases with decreasing temperature and then saturates at very low T, where the inelastic scattering events are frozen out. The inelastic scattering rate, τ_{ϕ}^{-1}, is important for dephasing of electrons, which is important in quantum transport and mesoscopic physics. Until very recently, there was neither experimental data nor theoretical expression to describe the temperature dependence of the inelastic scattering rate, due to dilute magnetic impurities, valid for temperatures T not too far below the Kondo temperature, T_{K}. In this work, our goal is to measure the magnetic inelastic scattering rate over a broad range of temperature, and to stimulate theoretical work in this direction.

In metals, the conduction electron can be scattered in two ways, elastically or inelastically. It is well known that elastic scattering preserves the phase coherence, since there is no energy exchange between the conduction electron and the scattering center. On the other hand, the inelastic scattering destroys the phase coherence of the conduction electron. At low temperature, there are three main sources for the

inelastic scattering in metals; the electron-electron, electron-phonon, and electron-magnetic impurity interactions.

The weak localization magetoresistance (MR) method is used to determine the value of the electron dephasing time τ_ϕ. We have measured τ_ϕ for both types of samples, pure and implanted samples. By subtracting the total dephasing rate of the pure sample from the total dephasing rate of the implanted ones, we extract the magnetic scattering rate, γ_m, of the conduction electrons off Fe impurities. We then compare our data with a recent theory of electron dephasing by dilute magnetic impurities.

The high field magnetoresistance is used in this work to obtain an independent estimate of the Kondo temperature, T_K. At an intermediate field scale, the implanted samples show a negative MR, whereas in pure films it is positive and proportional to B^2. The negative MR observed in the implanted samples is due to the presence of Fe magnetic impurities. From the high field MR data, we find that below 200 mK the magnetoresistivity saturates towards its unitary limit (its value at $T = 0$), indicating that the Fe spin is completely screened by the surrounding conduction electrons. We then compare our high field data with the Numerical Renormalization Group calculations of the MR for spin 1/2 magnetic impurities, provided to us by Theo Costi.

To my family

Acknowledgments

Finally, after being done with this thesis, it is time to thank many people who have contributed directly or indirectly to this work.

I would like to start with a big thanks to my supervisor, Norman Birge, from whom I learned many things during my stay here at Michigan State University. Norman, you are amongst the very few people that truly impressed me, not only in the professional point of view, but also as a person. I have always enjoyed our discussions in the field of physics and in other aspects of life. I learned from you many things about American culture and its values. I would like also to thank you for your financial support and for being so approachable whenever I needed help.

I would like also to thank Achim Rosch and T. A. Costi for providing us with the results of their Numerical Renormalization Group calculations, which were crucial to fit our experimental data for both phase coherence and high field magnetoresistance.

The encouragement I have received from my entire family is really appreciated. I really have to thank all of them individually: my father, my mother, my brother Iyad, who has dedicated his life to support our nuclear family, all of the rest of my brothers; Mustafa, Ali, Abdelah, my sisters : Abeer, who took care of us when we were kids, Amal and here husband, Jawaher, Amani and here husband, Amneh, Eman, Asma, Asrah, my sister and brother I lost Tahani and Omar, and my step mother, Khadeeja. Big thanks go to all my uncles, specifically my uncle Fawoor and his wife, relatives, my ant Dalal and her husband, and my grandmother, who always wants me to finish my PhD and come back as soon as I can. I would like also to thank my father and mother in law for giving me the best gift of my life, my wife Basma. And finally I would like to thank my lovely daughter Abeer for her nice interactions.

Special thanks go to Michael Crosser and Ion Moraru, who have taught me much during the first two years of my work with Norman.

I would like also to thank Baokang Bi for teaching me how to use properly the

critical instruments in the clean room, and Reza Loloee, for his technical support and for always being there to help. I also thank Prof. Pratt for the beneficial discussions we had when I was helping him running the advanced lab, and Prof. Mahanti for helping me understand the physics of local moments in metals and for teaching me two advanced courses in condensed matter physics.

And finally, I would like to thank my best friend Mustafa Alhaj-Darweesh, the one who recommended me to the graduate chairperson to be accepted here at MSU. Mustafa, you are the best friend of mine so far. I will never forget the best period of my life, the period we lived together for three years in Cherry Lane.

Contents

List of Figures

List of Tables

Chapter 1

Introduction

1.1 Introduction

The electron decoherence time (also called dephasing time), τ_ϕ, is a quantity of fundamental interest in mesoscopic systems. This time scale has been the subject of theoretical and experimental investigations for several decades. In mesoscopic physics, τ_ϕ is defined by the specific measurements one performs. In the context of quantum-transport phenomena such as weak localization, τ_ϕ determines the energy and length scales at which quantum behavior is seen. In the last two decades, many theoretical and experimental works have been directed toward understanding the mechanisms responsible for losing phase coherence in mesoscopic systems.

The phase coherence time, τ_ϕ, depends on temperature, disorder, and dimensionality. In quasi-1D wires, τ_ϕ was predicted to have the form $\tau_\phi \propto T^{-2/3}$ [1]. That prediction was proven experimentally on Al wires (at temperatures down to 2 K) in 1986 [2] and on Au wires (down to 100 mK) in 1993 [3]. In 1997, Mohanty *et al.* [4] reported measurements of τ_ϕ in six Au wires. In their study, they showed that τ_ϕ saturated at low temperature, inconsistent with the theoretical prediction mentioned above, where τ_ϕ diverges with decreasing temperature. They attributed this saturation in τ_ϕ to an intrinsic unavoidable source of decoherence, coming from

electron-electron interactions.

In 2003, Pierre *et al.* [5] ruled out the universal dephasing proposed by Mohanty *et al.*. They reported measurements of τ_ϕ for five samples fabricated from Ag and Au source material of 99.9999% purity. In those samples τ_ϕ did not saturate, but rather continued to increase down to 40 mK. Nevertheless, Pierre *et al.* found small saturation in some pure samples below 100 mK. They speculated that this saturation was caused by small amounts of magnetic impurities with low Kondo temperature. This debate of the zero-temperature dephasing has remained a puzzle, which attracted many theoretical and experimental works over the last decade [4, 5, 6, 7, 8, 9, 10, 11, 12]. Since then, people want to know what causes the saturation of τ_ϕ at very low T. One result of that work is that the scattering of conduction electrons by magnetic impurities play a major rule in electronic transport at low T. In this work, I will discuss the temperature dependence of τ_ϕ and resistivity of weakly disordered quasi-1D Ag wires that are intentionally implanted with Fe impurities. Ion implantation of the magnetic impurities allows us to study the Kondo physics in samples with a known concentration of impurities.

1.1.1 Transport in metals

The simple classical model that describes transport in metals is the Drude model. This model of electronic conduction was developed in the 1900s by Paul Drude to explain the transport properties of electrons in materials (especially metals). The Drude model is the application of kinetic theory to electrons in a solid. It assumes that the metal contains immobile positive ions and an electron gas of classical, non-interacting electrons of density n, each of whose motion is damped by a frictional force, due to collisions of the electrons with various scattering sites. These collisions

lead to a finite resistivity which can be expressed as [13]

$$\rho = \frac{m}{ne^2\tau_e} \tag{1.1}$$

where m is the electron mass, e is the charge, n is the electron density, and τ_e is the average time between collisions. The quantity, τ_e, is related to the mean free path l_e by $l_e = v_F\tau_e$, where v_F is the Fermi velocity.

The electrical resistivity of most metals is dominated at room temperature (300 K) by collisions of the conduction electrons with lattice vibrations (phonons) and at liquid helium temperature (4.2 K) by collisions with static disorder such as grain boundaries, impurities, and lattice defects. Assuming that the two rates of these collisions are independent, the total resistivity could be represented by the sum of the two contributions (Matthiessen's rule) [13]

$$\rho_{total} = \rho_0 + \rho_{phonon} \tag{1.2}$$

where ρ_0 is the temperature independent contribution due to static impurities and boundary scattering and the second term ρ_{phonon} is the contribution due to phonons, which is temperature dependent. For temperature much less than the Debye temperature, ρ_{phonon} takes the form $\rho_{phonon} = aT^5$, where a is constant.

In metals, as seen from equation (1.2), the resistivity normally decreases monotonically with decreasing temperature and reaches a constant residual value at zero temperature (see figure 1.1). This general picture of low temperature transport is in good agreement with most experiments done on very pure metals. In some cases, a minimum was observed in the resistivity at low temperature, as shown in figure (1.1). This was attributed to the presence of magnetic impurities and will be discussed in section (1.2).

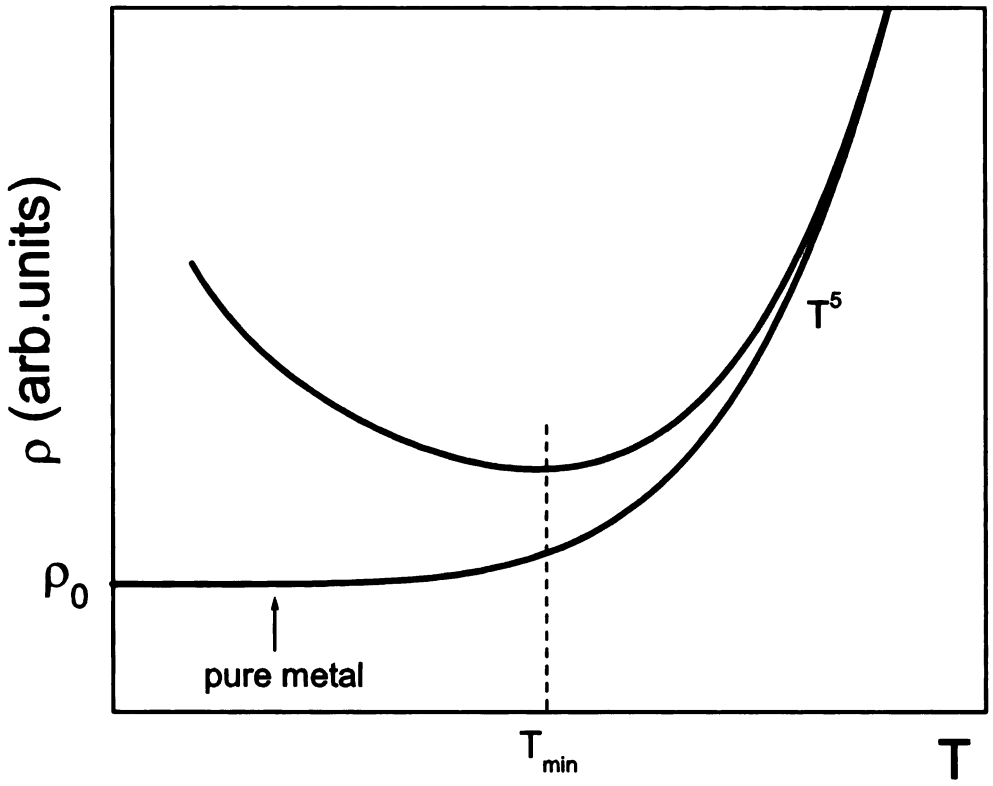

Figure 1.1: Schematic of resistivity vs temperature for pure metal (lower curve) and metal containing residual magnetic impurities (upper curve). The minimum in the upper curve is caused by the presence of magnetic impurities in a metal host.

1.1.2 Scattering mechanisms and phase coherence in metals

The conduction electron can be scattered in two ways, elastically or inelastically. It is well known that elastic scattering preserves phase coherence, since there is no energy exchange between the conduction electron and the scattering center. Typical elastic scattering events are scattering of conduction electron by static impurity atoms or film boundaries. To a good approximation, the elastic scattering is temperature independent and depends only on the amount of disorder in the system. The amount of disorder in a system is usually measured by the diffusion constant D or alternatively by the mean free path l_e. The higher the value of D (or the longer l_e) is , the less the amount of disorder.

On the other hand, the inelastic scattering destroys the phase coherence of the

conduction electron due to the energy exchange between the conduction electron and the scattering center. There are three main sources for the low temperature dephasing in metals; the electron-electron , electron-phonon, and electron-magnetic impurity interactions. It is known that the above three dephasing sources may coexist in real systems, with one or two sources typically dominating, depending on the system dimensionality, the amount of disorder, and the measurement temperature.

In many cases, quantum interference phenomena are observed in weakly disordered systems, in which electrons are able to undergo multiple elastic scattering at low temperatures, before the coherence of their wave function is randomized. The electron dephasing time τ_ϕ (also called phase breaking time) depends on both disorder and temperature. In the diffusive regime, the quantity τ_ϕ is related to the dephasing length L_ϕ (also called phase breaking length) by $L_\phi = \sqrt{D\tau_\phi}$. The electron diffusion constant is given by $D = v_F^2\tau_e/d$, where v_F is the Fermi velocity, τ_e is the elastic mean free time, and d is the effective dimensionality of the system under study. Usually, L_ϕ can be several microns at liquid-helium temperatures in disordered metals.

1.2 Magnetic impurities and Kondo effect

When the spin degree of freedom of both the conduction electrons and the magnetic impurity atoms is taken into consideration, the quantum transport effects become sensitive to the magnetic spin-spin scattering. The spin-spin scattering can originate from scattering of conduction electrons off magnetic impurity atoms. The scattering of conduction electrons by magnetic impurity is know as Kondo effect. In the following three subsections, I will discuss briefly the history of this effect.

1.2.1 Early observations of resistivity minimum and Kondo problem

The minimum in resistivity of some metals as a function of temperature was first observed in 1934 in a Au sample[14]. Other observations [15], with a controlled concentrations of magnetic Fe impurities in Cu samples, have shown that this effect was related to the presence of magnetic impurities in the non-magnetic host metal.

It was not until 1964 that this minimum was shown by J. Kondo [16] to arise from some unexpected features of the scattering of conduction electrons that arise only when the scattering center has a magnetic moment. In such a case the exchange interaction between the conduction electrons and the local moment leads to scattering events in which the electronic spin is flipped (with a compensation change of spin on the local moment). The essential facts that Kondo proposed to explain the resistivity minimum are as follows [16]. First, the low temperature anomalies result from magnetic impurities. Second, the depth of the minimum ($\Delta\rho = \rho_{T=0} - \rho_{min}$) is proportional to the impurity concentration. Third, the value of ρ_{min} itself is also proportional to the impurity concentration; therefore $\Delta\rho/\rho_{min}$ is concentration independent. This is true only if the magnetic impurities dominate the residual resistivity. Fourth, the temperature of the resistivity minimum is almost independent of the impurity concentration.

The Kondo Hamiltonian takes the form

$$H = H_0 + H_{sd} \tag{1.3}$$

where H_0 is the unperturbed Hamiltonian of the conduction electrons and the perturbation H_{sd} describes the interactions between the local moment and the conduction electrons, which is given by

$$H_{sd} = -\sum J\vec{S}_d.\vec{s} \tag{1.4}$$

where J is the coupling constant, $\vec{S_d}$ is the spin of the localized moment and $\vec{s}$ is the conduction electron spin.

Let us first discuss the physics of two spins $\vec{S_1}$ and $\vec{S_2}$ interacting via the Hamiltonian $H = -J\vec{S_1}.\vec{S_2}$, where J is the interaction strength. The total spin is $\vec{S} = \vec{S_1} + \vec{S_2}$, and using $S^2 = S_1^2 + S_2^2 + 2\vec{S_1}.\vec{S_2}$, the total energy can be written as

$$E = -\frac{J}{2}[S(S+1) - S_1(S_1+1) - S_2(S_2+1)] \tag{1.5}$$

consider the special case $S_1 = S_2 = 1/2$, the total energy becomes

$$E = -\frac{J}{2}[S(S+1) - \frac{3}{2}] \tag{1.6}$$

Now for two a spin 1/2 system, the total spin could be 0 (singlet) or 1 (triplet). In the singlet state, the spins favor antiparallel alignment, therefore it is non magnetic, while in the triplet state the spins favor parallel alignment, and hence it is magnetic. The energy difference between parallel and antiparallel configurations is the exchange energy, J. So from equation (1.6) we have

$$E = \begin{cases} \frac{3}{4}J & \text{if } S = 0 \\ -\frac{J}{4} & \text{if } S = 1 \end{cases}$$

From this result, one can see that if $J < 0$, the ground state is an antiferromagnetic singlet. On the other hand, if $J > 0$, the ground state is a ferromagnetic triplet (see figure 1.2). Kondo effect is relevant to the first case, $J < 0$, where the coupling between the conduction electron spin and the local moment spin is antiferromagnetic. The other limit $J > 0$, for ferromagnetic coupling, the perturbation theory converges and the physics is much simpler.

In the first Born approximation (second order in J) it had been shown that H_{sd}

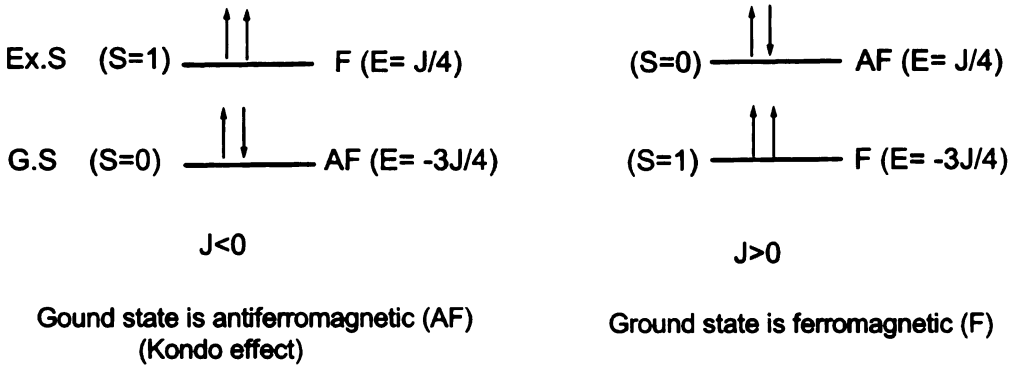

Figure 1.2: Schematic of the energy configurations of two spin 1/2 system. Left : energy levels of the two spins if they are coupled antiferromagnetically, $J < 0$. Right : energy levels of the two spins if they are coupled ferromagnetically, $J > 0$.

does not lead to any anomaly in the resistivity, merely a dependence on J^2. Kondo, however, calculated the resistivity in the second Born approximation (third order in J) and found, for a negative J, a low-temperature correction to the resistivity proportional to $-c\rho_1 \log(T)$, where c is the concentration of magnetic impurities and ρ_1 is constant. The negative value of J means that the ground state of the conduction electron and the localized moment is a singlet, which favors antiparallel alignments (i.e antiferromagnetic coupling). When this new term is added to the other contributions to the resistivity, we find

$$\rho = c_{imp}\ \rho_0 + aT^5 - c_{imp}\ \rho_1 \log\left(\frac{k_B T}{D}\right) \tag{1.7}$$

with $c_{imp} = N_s/N$, where N_s is the number of magnetic impurities and N is the number of sites, and $D = 2\varepsilon_F$ is the bandwidth, where the electronic density of states (DOS) was assumed to be constant. By setting $\frac{d\rho}{dT} = 0$, we have

$$T_{min} = (\frac{\rho_1}{5a})^{1/5} c_{imp}^{1/5} \tag{1.8}$$

it is easily seen that equation (1.7) has a minimum, and thus Kondo was able to explain the resistivity minimum.

Kondo's theory was successful in explaining the resistivity minimum. But looking carefully at equation (1.7), one can see that as $T \rightarrow 0$, the resistivity correction diverges. This divergence in Kondo's theory is termed as the "Kondo problem". On the other hand, the experimental data show that the resistivity increases logarithmically down to some temperature, but it then levels off at some point as shown schematically in figure (1.3). The temperature at which the resistivity is observed to deviate from equation (1.7) is referred to as Kondo temperature, T_K, and in term of the exchange constant, J, can be written as [17]

$$T_K = T_F \; exp \; (-\frac{1}{|J|N(E_F)}) \tag{1.9}$$

where T_F is the Fermi temperature of the host and $N(E_F)$ is the conduction electron density of states at the Fermi level. The characteristic temperature T_K varies wildly from 300 K for Vanadium in Au to 40 mK for Mn in Au or Ag [17]. For a comprehensive review about Kondo effect and related topics, I refer the reader to reference [18].

1.2.2 Solution of the Kondo problem

In the late 60s Anderson was trying to solve the Kondo problem at $T \ll T_K$ using the ideas of scaling. He showed that at temperatures far below the Kondo temperature ($T \ll T_K$), the effective interaction strength between the conduction electrons and local moments becomes infinitely large [19]. Thus as $T \rightarrow 0$, the conduction electrons become localized around the moment forming a spin compensated (i.e nonmagnetic) ground state. Quantitatively, Anderson's approach broke down at low temperatures ($T \ll T_K$) because of the infinite coupling between the conduction electrons and the local moment.

In 1975 [20], Wilson solved the Kondo problem using the numerical renormaliza-

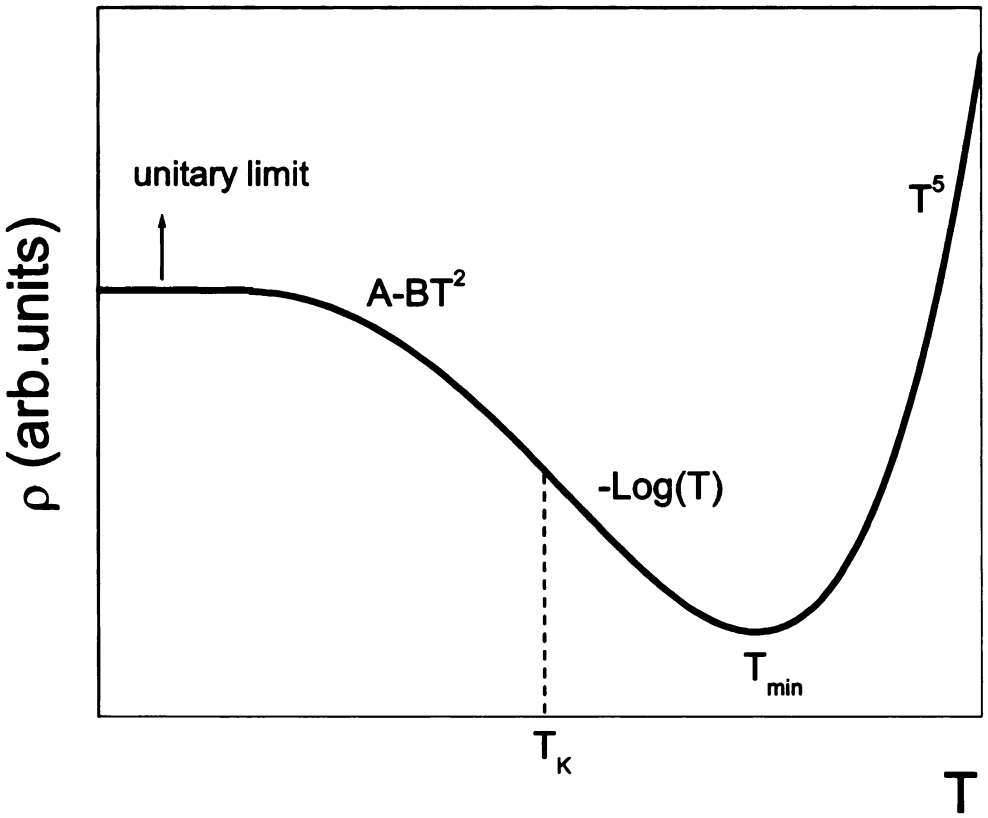

Figure 1.3: Schematic of resistivity vs temperature for metal containing magnetic impurities. At high T, the resistivity is dominated by electron-phonon scattering; at low T by electron-magnetic impurity scattering; and at temperatures far below T_K, the magnetic impurity is completely screened and behaves like static impurity.

tion group technique and ruled out the zero-temperature divergence of the resistivity for $S = 1/2$ magnetic impurity. He showed that at temperatures far below the Kondo temperature ($T \ll T_K$), the spin of the magnetic impurity is totally screened by the conduction electrons. For conduction electrons, the screened impurity appears then as a potential scattering center. Using this non-perturbative approach, Wilson was able to predict the low temperature thermodynamic behavior of dilute Kondo alloys. For the resistivity at $T \ll T_K$, the predicted form is [18]

$$\rho_{imp}(T) = \rho_0 \left[1 - \frac{\pi^4}{16} w^2 \left(\frac{T}{T_K} \right)^2 \right] \tag{1.10}$$

where $w \approx 0.4128$ is Wilson's number, and ρ_0 corresponds to the unitary limit, which is given by

$$\rho_0 = c_{imp} \frac{4m}{e^2 \pi \hbar N(E_F)} \tag{1.11}$$

with m and $N(E_F)$ being the electron mass and the conduction electron total density of states at the Fermi level, and $c_{imp} = N_s/N = n_s/n$ is the concentration of magnetic impurities. The unitary limit is the value of the electrical resistivity at $T = 0$. This value is related to the total scattering cross section at $T = 0$. At zero temperature, the conduction electron scatters only elastically (both energy and spin unchanged) with a scattering cross section $\sigma_e = 4\pi/k_F^2$, where k_F is the Fermi wave number of the host. The elastic scattering is due to scattering of the conduction electron by static disorder with a mean free path $l_e = 1/n\sigma_e$. The residual resistivity then reads

$$\rho_0 = \frac{m}{ne^2\tau_e} \tag{1.12}$$

where τ_e is the elastic mean free time. Using $l_e = v_F \tau_e$ and $p_F = \hbar k_F$, where v_F and p_F are the Fermi velocity and Fermi momentum, ρ_0 becomes

$$\rho_0 = \frac{4\pi\hbar}{e^2 k_F} \tag{1.13}$$

using $N(\varepsilon_F) = mk_F/\pi^2\hbar^2$ in the last equation, we arrive back to equation (1.11).

After this great work of Wilson, the Kondo problem was considered to be solved. His contribution was recognized later in the award of the Nobel prize in 1982. It is time here to mention that all these models developed by Kondo, Anderson, Wilson, and others are valid only for $S = 1/2$ magnetic impurities. For $S > 1/2$, the problem becomes more complicated.

1.2.3 Previous measurements of Kondo contribution to decoherence rate

In a pure but disordered quasi-1D metal, the decoherence scattering rate of the conduction electrons is given by [1, 11]

$$\gamma_\phi(T) = AT^{2/3} + BT^3 \tag{1.14}$$

where the first term describes the electron-electron scattering rate, dominating at lower T, and the second term describes the electron-phonon scattering rate, dominating at higher T. In a metal containing a small amount of magnetic impurities, there is an additional contribution to $\gamma_\phi(T)$ from the scattering of the conduction electrons by the magnetic impurities, $\gamma_m(T)$. Experimentally, the temperature dependence of the magnetic scattering rate, $\gamma_m(T)$, is usually obtained by subtraction of $\gamma_{\phi,pure}(T)$ values for the pure sample from $\gamma_{\phi,doped}(T)$ values for the doped sample as shown schematically in figure (1.4). The figure shows that $\gamma_m(T)$ peaks at $T = T_K$. The magnetic scattering rate, γ_m, is sometimes called the spin-flip scattering rate, γ_{sf}. In this thesis I will use both terms interchangeably.

The magnetic impurity contribution to the conduction electron phase decoherence rate, τ_ϕ^{-1}, was first measured explicitly by two groups in 1987 [21, 22]. C. Van Haesendonck *et al.* [21] measured the spin-flip scattering rate, $\gamma_{sf}(T)$, in very thin Cu films ($t \simeq 5\ nm$), doped with magnetic Cr atoms (with two concentrations of 13, and 40 ppm, respectively). They found a maximum in $\gamma_{sf}(T)$ which is in a good agreement with the Suhl-Nagaoka approximation (see below) near the vicinity of the Kondo temperature $T_K \simeq 2\ K$. In their work, no conclusions can be drawn about the behavior of $\gamma_{sf}(T)$ below the Kondo temperature, since they only have four data points below T_K down to 0.5 K.

R. P. Peters *et al.* [22] measured the spin-flip scattering rate, $\gamma_{sf}(T)$, in Au films

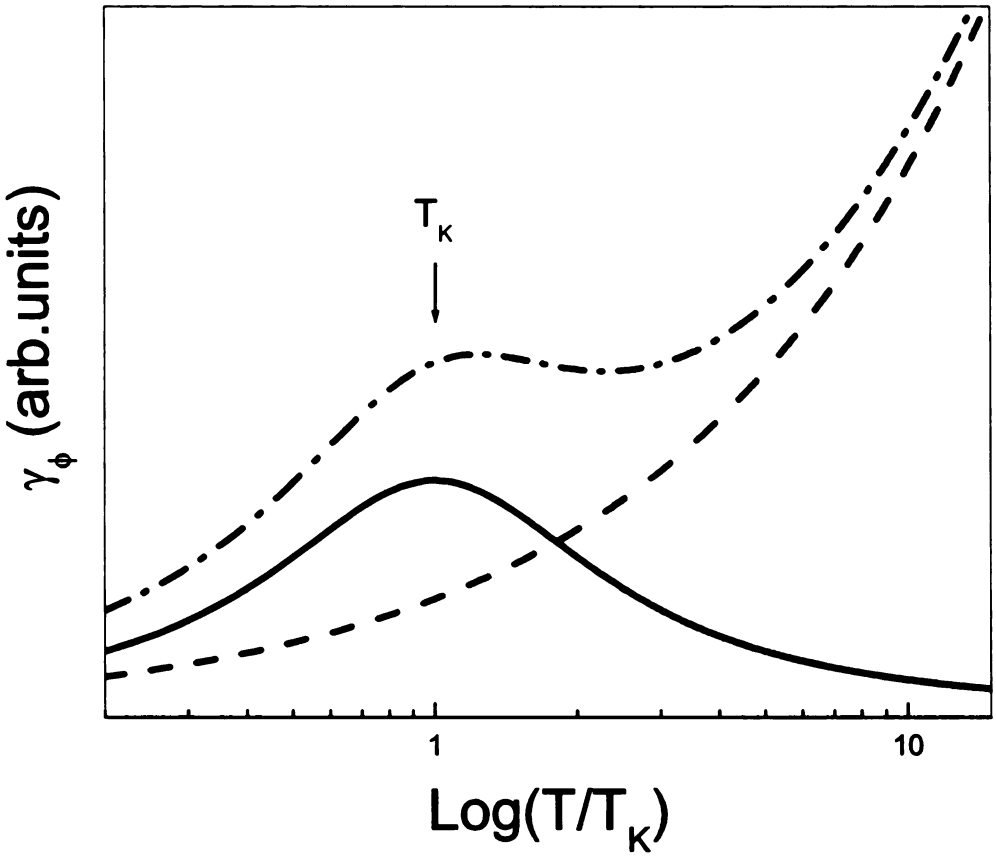

Figure 1.4: Schematic of the total scattering rates as a function of temperature for pure metal (dashed line) and metal containing magnetic impurities (dashed-dotted line). The solid line is the magnetic scattering rate, $\gamma_m(T)$, which is the difference between the other two. At temperatures far below T_K, $\gamma_m(T)$ vanishes, indicating that the magnetic impurity is completely screened and behaves like static impurity.

containing Fe magnetic impurities in the range between 0.08 and 4 K. They found a strong temperature dependence of $\gamma_{sf}(T)$ with a broad maximum at the characteristic temperature $T_K \simeq 1\ K$. The same system, AuFe, has been studied by P. Mohanty *et al.* [23] in 2000 and F. Schopfer *et al.* [24] in 2003, but this time in quasi-1D wires. They both found a maximum near 0.3 K. Again, because of the relatively low Kondo temperature of this system, it was hard to explore the regime where $T \ll T_K$.

1.3 Motivation for current study

The inelastic scattering problem of the conduction electrons in a pure metal was completely solved by Altshuler-Aronov-Khmelntzky (AAK) [1] theory, where there are only two sources of the decoherence, electron-phonon and electron-electron. But adding a small a mount of magnetic impurities to the pure metal makes things complicated and until very recently, no complete solution was available for the complete temperature dependence of the magnetic scattering rate. At $T > T_K$, the experimental data could be described well by the Suhl-Nagaoka expression [17, 21].

$$\frac{1}{\tau_{sf}} = \frac{n_s}{\pi\hbar\nu_F} \frac{\pi^2 S(S+1)}{\pi^2 S(S+1) + \ln^2(T/T_K)} \tag{1.15}$$

with S, T_K, and ν_F respectively the spin and the Kondo Temperature of the magnetic impurity, and the total DOS of the conduction electrons at the Fermi level. On the other hand, for ($T \ll T_K$), Fermi liquid theory predicts a T^2 dependence of γ_m [25], which, however, has never been observed experimentally. This takes the form [26]

$$\frac{1}{\tau_{sf}} \propto \frac{n_s}{\hbar\nu_F} \left(\frac{T}{T_K}\right)^2 \tag{1.16}$$

At the time we started this work, there was neither experimental data nor theory to describe the intermediate regime for T not too far below T_K (see figure 1.5). Our goal was to measure the magnetic scattering rate over a broad range of temperature, and to stimulate theoretical work on the problem.

While we carried out our experiments, a theory [27] was proposed to explain the complete temperature dependence of $\gamma_m(T)$ for conduction electrons scattered by dilute spin- 1/2 magnetic impurities. The theory relates $\gamma_m(T)$ to an earlier calculation [28] of the inelastic scattering cross section, σ_{inel} (ω), by the numerical renormalization group method. The main conclusion of these works is that the magnetic

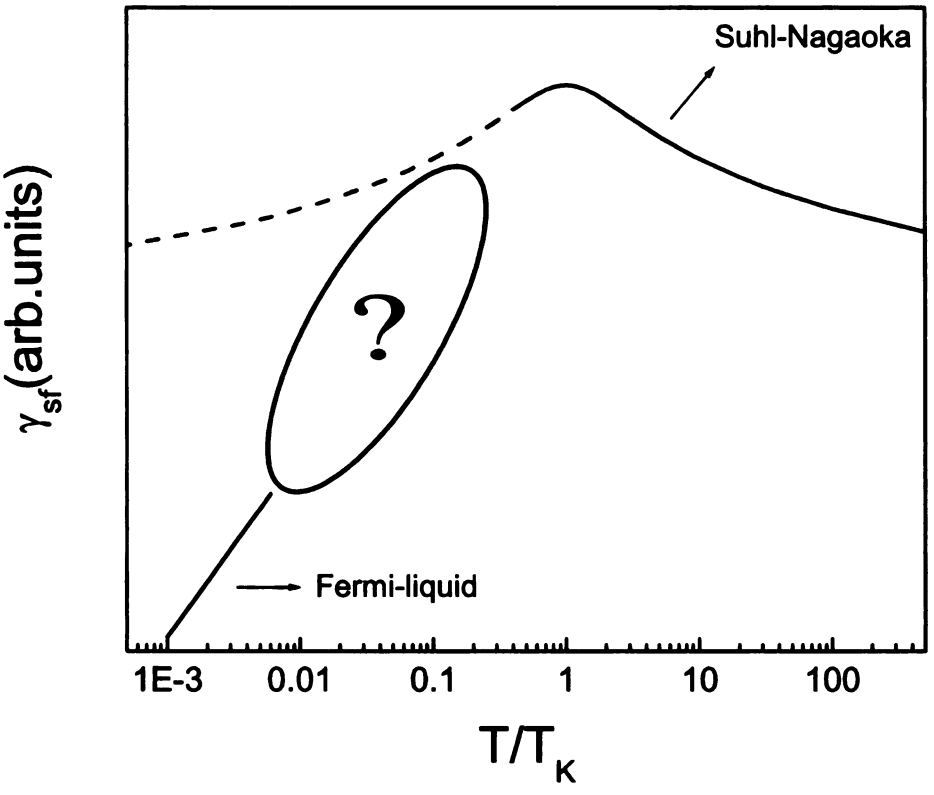

Figure 1.5: Schematic of the theoretical situation of the magnetic scattering rate as a function of temperature (at the time we started this work). At $T > T_K$, the experimental data could be described well by the Suhl-Nagaoka expression. For $T \ll T_K$, Fermi liquid theory predicts a T^2 dependence of γ_m, which falls far below the Suhl-Nagaoka expression.

scattering rate, $\gamma_m(T)$, has only a very weak (logarithmic) temperature dependence above T_K, has a broad maximum around T_K, scales approximately linearly with T for $0.1T_K < T < T_K$, and scales as $\sim T^2$ for $T < 0.1T_K$. These theories can be considered as a major breakthrough for the decoherence problem, as they allow one to compare experimental data with theoretical results for all temperatures, ranging from well above T_K down to $T \ll T_K$.

In addition to the main conclusion, mentioned above, the theory of Micklitz *et al.* [27] predicts that if the density n_s of magnetic impurities is sufficiently low, the magnetic scattering rate, $\gamma_m(T)$, is a universal function of temperature, $\gamma_m(T) \propto$

$n_s f(T/T_K)$, and depends only on two parameters, n_s and T_K.

What is the best candidate Kondo system to start with? In the presence of magnetic impurities, τ_ϕ^{-1}, contains the additional contribution γ_m, which peaks at $T = T_K$. In order to observe this peak in γ_m while keeping the magnetic impurity concentration low enough to avoid interactions between impurities, one must choose a system with T_K below about 10 K; otherwise τ_ϕ^{-1} is dominated by electron-phonon scattering. In order to acquire data far below T_K, however, it is important to keep T_K as high as possible. The optimal range for T_K is a few Kelvins, which is achieved with Fe impurities in Ag [17, 29].

1.4 Outline of thesis

The outline of this thesis is as follows. Chapter 2 covers the theoretical techniques necessary to understand the physics of phase decoherence in pure metals. It includes a brief description of length scales related to our experiment, electron weak localization, spin-orbit coupling, and decoherence mechanisms in pure metals.

Chapter 3 describes the Kondo effect in dilute magnetic alloys. Here we give more details about the scattering of conduction electrons from magnetic impurities.

Chapter 4 discusses the experimental techniques used. First, fabrication of the samples will be presented. This includes wafer processing, e-beam writing and development, evaporation and lift-off, and Ion implantation. Second, the methods used to make measurements on these samples will be shown.

Chapters 5 talks about our phase coherence results for both pure and implanted samples. Specifically, it describes how L_ϕ, and hence τ_ϕ, can be determined from magnetoresistance measurements. Then, we show how the magnetic scattering rate,γ_m, due to dilute magnetic impurities, can be extracted from the measured total dephasing rates, γ_ϕ. And finally, we compare our experimental γ_m data with recent theory [27] of scattering of conduction electrons by dilute magnetic impurities in quasi-1D

wires.

Chapters 6 discusses the high field magnetoresistance measurements for both pure and implanted samples. Specifically, it describes how the Kondo temperature, T_K can be determined independently from analyzing the high field magnetoresistance data in the context of Numerical Renormalization Group (NRG) calculations.

Chapter 7 summarizes this work.

Chapter 2

Theory I: Quantum Transport and Phase Coherence

2.1 Mesoscopic physics and length scales

Mesoscopic physics refers to systems which are somewhere in between macroscopic (i.e. classical) and microscopic (i.e. quantum). Macroscopic systems are considered big enough to be described well by classical mechanics, whereas mesoscopic systems are small enough such that their properties can be described quantum mechanically. In a macroscopic system, any physical quantity can be represented by its average, where fluctuations around the average are negligibly small. On the other hand, the fluctuations in a mesoscopic system become important and sometimes they can be as big as the average itself. In the mesoscopic regime, scattering from static disorder induces quantum interference effects which affect the flow of electrons. A typical example of these quantum effects is the electron weak localization which I will discuss in the next section. For more details about mesoscopic physics, I refer the reader to references [30, 31]. The length scales play a major rule in mesoscopic physics. Next, I will briefly define some of the length, energy, and time scales that are relevant to this work. The system dimensions will be denoted by L, w, and t, where L, w, and

t are the length, the width, and the thickness, respectively. Below I list the most commonly used length, time, and energy scales:

λ_F : Fermi wavelength; wavelength of electrons that carry electrical transport. The corresponding energy scale is the Fermi energy, E_F, which is the energy of the highest occupied electron energy level. In metals, typical values of λ_F and E_F are of order several Å and several eV, respectively.

l_e : electron elastic mean free path; the distance an electron travels before it is elastically scattered by static disorder.The corresponding time scale is the electron mean free time, τ_e. l_e and τ_e are related by $l_e = v_F\tau_e$, where v_F is the Fermi velocity. l_e is considered temperature independent and depends only on the amount of disorder in the system. In weakly disordered metals, l_e is of order 50 nm.

L_ϕ : electron phase coherence length; the distance an electron travels before its phase memory is lost due to inelastic scattering event.The corresponding time scale is the phase coherence time, τ_ϕ. L_ϕ and τ_ϕ are related by $L_\phi = \sqrt{D\tau_\phi}$, where $D = v_F l_e/3$ is the diffusion constant. Both L_ϕ and τ_ϕ are temperature dependent. In metals, L_ϕ can be several microns at liquid He temperature.

τ_{e-e} : electron-electron scattering time; the time it takes for an electron to be scattered inelastically by another electron. This time scale is temperature dependent. At $T \approx 1\ K$, τ_{e-e} can be around 10 ns in pure metals.

τ_{e-ph} : electron-phonon scattering time; the time it takes for an electron to be scattered inelastically by phonon. This time scale is temperature dependent. At $T \approx 1\ K$, τ_{e-ph} can be around 30 ns in pure metals.

τ_{sf} : the spin-flip scattering time; the time between scattering events involving an electron and a magnetic impurity such that the electron's spin is flipped. This

time scale is temperature dependent; it decreases near the Kondo temperature, then increases with reducing temperature. It also depends on concentration of magnetic impurities.

k_BT : electron thermal energy; at room temperature, $k_BT \approx 26$ meV. At 40 mK, $k_BT \approx 3.4$ μeV.

By comparing the mean free path l_e with one of the system dimensions, say L, one can discriminate between two regimes of transport, diffusive and ballistic. The diffusive regime is defined by $\lambda_F \ll l_e \ll L$. On the other hand, $l_e \gg L$ defines the ballistic regime.

2.2 Electron weak localization

2.2.1 Weak localization in disordered metals

Weak localization (WL) is a quantum effect, which occurs in disordered electronic systems at very low temperatures. In weakly disordered systems ($k_F l_e \gg 1$) and at low temperatures, this effect gives rise to higher resistivity than that predicted by the Drude model due to the enhanced backscattering of the electron partial waves. This effect is referred to as weak localization to distinguish it from the strong localization that occurs in highly disordered systems.

In weakly disordered metals, the electron motion is diffusive rather than ballistic. That means an electron does not move along a straight line, but experiences a series of random scatterings off static impurities which results in a random walk. Consider two electron partial waves (1, 2) starting at the origin and traveling diffusively along two different paths in the opposite directions and finally arriving back to the origin (see figure 2.1). In principle there are many paths the two partial waves can follow, but for simplicity we will take only two of them. Along the paths, the two partial waves

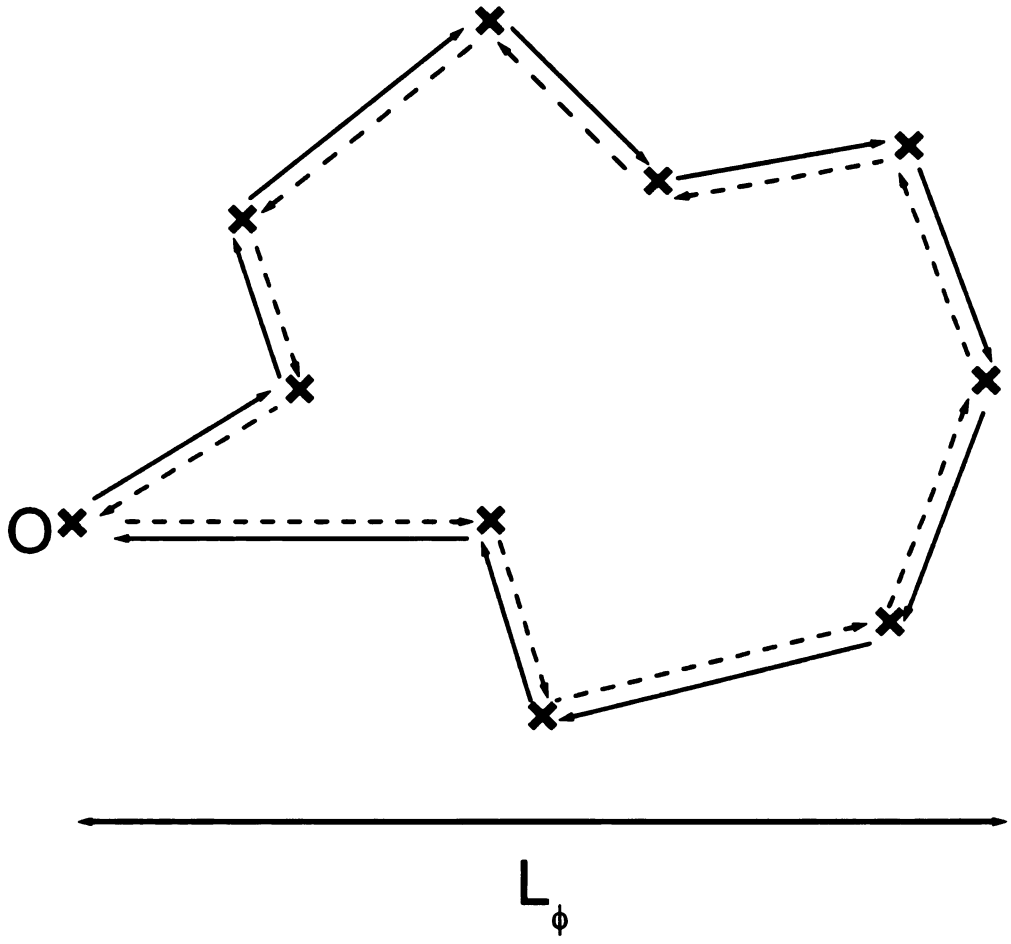

Figure 2.1: Two electron partial waves starting at the origin, moving diffusively along two time-reversed paths, and arriving back to origin coherently. The size of the path is of order L_ϕ. The crosses are the static impurities.

are scattered elastically by static impurities. Let $\mathbf{A_1} = |A_1|e^{i\phi_1}$ and $\mathbf{A_2} = |A_2|e^{i\phi_2}$ be the wave functions of the two partial waves, where ϕ_1 and ϕ_2 are their phases. Classically, the total return probability is the sum of the individual probabilities along the two paths ($W_{classical} = |A_1|^2 + |A_2|^2$). However, quantum mechanically, to find the total probability we have to sum up the quantum-mechanical amplitudes of the two paths rather than the corresponding probabilities. Therefore, the correct formula for return probability, $W_{quantum}$, includes the classical part (individual probabilities of the two diffusive paths) and the interference term (product of the two amplitudes

corresponding to the two different paths). This can be written as [30, 31]

$$\begin{aligned} W &= |\mathbf{A_1} + \mathbf{A_2}|^2 \\ &= (\mathbf{A_1} + \mathbf{A_2})(\mathbf{A_1^*} + \mathbf{A_2^*}) \\ &= |A_1|^2 + |A_2|^2 + 2|A_1||A_2|cos(\phi_1 - \phi_2) \end{aligned} \tag{2.1}$$

The first two terms are the classical probability and the third one is the quantum interference contribution to the backscattering. In the absence of magnetic field, spin-orbit scattering, and dephasing sources along the paths, the classical and quantum interference contributions are equal. Let us assume that the two paths are time reversed; this means the two partial waves traverse the same path in opposite directions. For any two time-reversed paths, $A_1 = A_2$, and since the two waves leave the origin at the same time, cover the same path length, and see exactly the same elastic scattering events along the paths, they arrive back to the origin coherently (i.e $\phi_1 = \phi_2$). Then the total quantum probability reads

$$W_{quantum} = 4|A_1|^2 = 2W_{classical} \tag{2.2}$$

Therefore, the quantum probability is twice the classical one. Because the probability of finding the electron at the origin has been enhanced, its chances for diffusion are reduced thereby increasing the resistivity.

2.2.2 Spin-Orbit scattering (weak antilocalization)

In the absence of spin-orbit coupling the wave functions of the two complementary partial waves are in phase and interfere constructively once they arrive back to origin. The spin-orbit scattering originates from the interaction of the conduction electron's spin with the angular momentum of the host atoms. This interaction rotates the

spin direction of the partial waves. However, quantum theory tells us that spin 1/2 particles have to be rotated by 4π to transfer the spin state back into itself. On the other hand, the rotation of 2π changes the sign of the wave function [32]. The two partial waves, discussed above, experience the same elastic scattering events, but in opposite directions. The spin of the first partial wave is rotated during each scattering process, and when the wave has reached its final state (s'), all rotations add up to finite rotation R. This can be written as [32]

$$s' = R.s \tag{2.3}$$

where the spin rotation R is usually described by three angles , (θ, ϕ, ψ).The second complementary wave experiences the same infinitismal rotations in opposite direction and opposite sequence. This reads

$$s'' = R^{-1}.s \tag{2.4}$$

The two rotations are not equivalent, therefore the final spin states of the two wave functions have different orientations and their scalar product can be written as

$$\langle s''|s'\rangle = \langle s|R^2|s\rangle \tag{2.5}$$

This factor was calculated in references [32, 33, 34, 35], and it was found that in the presence of spin-orbit coupling, the weak localization magnetoresistance is modified by a factor $\overline{Q_{so}}$ which is given by [34]

$$\overline{Q_{so}(t)} = \frac{3}{2}e^{-4t/3\tau_{so}} - \frac{1}{2} \tag{2.6}$$

This results shows that there are two important limits: weak and strong spin-orbit coupling. In the weak spin-orbit limit, where $\tau_{so}/\tau_{\phi} \gg 1$, equation (2.6) gives $\overline{Q_{so}} = 1$.

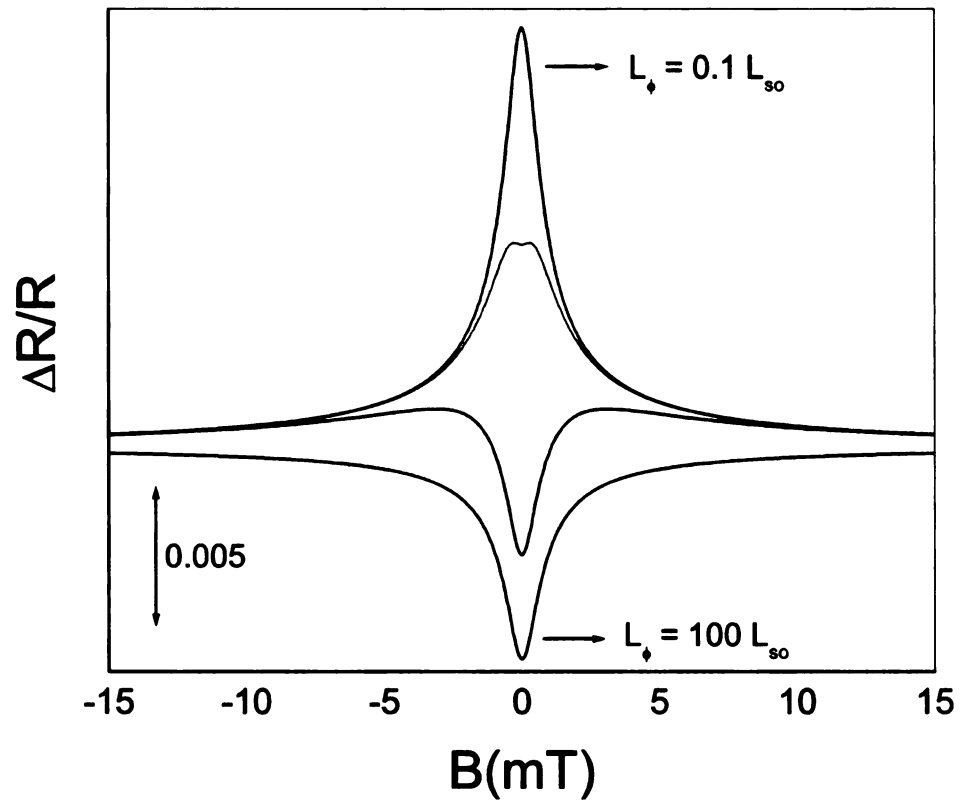

Figure 2.2: The calculated magnetoresistance curves using equation (2.8) of 1 KΩ wire with $L = 100\ \mu m$, $w = 100\ nm$, and $L_\phi = 20\ \mu m$, for different spin-orbit coupling lengths. From top to bottom: $L_\phi/L_{so} = 0.1$, 1, 5, and 100. Notice that for strong spin-orbit coupling, the magnetoresistance is positive (dip), while for weak spin-orbit coupling, it is negative (peak).

This has no effect on the WL magnetoresistance lineshape. In this limit the WL magnetoresistance is expected to be negative (peak at $B = 0$) as shown in figure (2.2). On the other hand, for the strong spin-orbit limit, where $\tau_{so}/\tau_\phi \ll 1$, equation (2.6) gives $\overline{Q_{so}} = -1/2$. This means that the spin-orbit coupling reverses the sign of the weak localization as well as reduces the magnitude of the signal by factor 2. Therefore, the WL magnetoresistance is expected to be positive (dip at $B = 0$). The latter effect is called weak antilocalization, since it changes the sign of the backscattering interference.

It was found that τ_{so}^{-1} depends on Z, the atomic number of the host atom, and

can be written as [36]

$$\frac{1}{\tau_{so}} = \frac{Z^4\alpha^4}{\tau_e} \tag{2.7}$$

where $\alpha = e^2/4\pi\epsilon_0 c\hbar \approx 1/137$ is the fine structure constant and τ_e is the elastic mean free path. Equation(2.7) predicts that spin-orbit coupling is stronger in high Z metals such as Au, $Z = 79$, and it can be neglected in low Z ones. In Ag, $Z = 47$, the spin-orbit strength has a moderate value.

2.2.3 Low-field magnetoresistance

In this section I briefly review the use of weak localization magnetoresistance to determine the low-temperature value of the phase coherence time, τ_ϕ. Physically, τ_ϕ sets the time scale over which the two partial waves, discussed in the last subsection, interfere constructively once they arrive back to the origin (see figure 2.1). In the presence of magnetic field and any time-reversal breakers such as e-e, e-ph, and e-magnetic impurity interactions, the weak localization magnetoresistance will be suppressed. In 1980, Hikami *et al.* [33] showed how the weak localization might be suppressed by an external magnetic field.

In a mesoscopic one dimensional conductor, the weak localization magnetoresistance at a given temperature, $\Delta R(B) = R(B) - R(0)$, is given by [1, 5, 11]

$$\frac{\Delta R(B)}{R} = \frac{2R}{R_K L}\left\{\frac{3}{2}\left[\frac{1}{L_\phi^2} + \frac{4}{3L_{so}^2} + \frac{1}{3}\left(\frac{w}{L_H^2}\right)^2\right]^{-1/2} - \frac{1}{2}\left[\frac{1}{L_\phi^2} + \frac{1}{3}\left(\frac{w}{L_H^2}\right)^2\right]^{-1/2}\right\} \tag{2.8}$$

where R is the resistance of a wire, L and w are its length and width, $R_K = h/e^2$ is the resistance quantum, $L_\phi = \sqrt{D\tau_\phi}$ is the phase coherence length, D is the diffusion coefficient of electrons, $L_H = \sqrt{\hbar/eB}$ is the magnetic length, B is the magnetic field applied perpendicularly to the sample plane, and $L_{so} = \sqrt{D\tau_{so}}$ is the spin-orbit length. The quantity under the square root of the first term in equation (2.8) is called

the triplet term and the quantity under the square of the second term is the singlet one. In the limit of weak spin-orbit coupling ($L_{so} \longrightarrow \infty$), both quantities are equal, whereas in the limit of strong spin-orbit coupling ($L_{so} \longrightarrow 0$), the triplet term has a small contribution and can be ignored (see figure 2.2). Equation (2.8) is valid for metallic wires in the diffusive regime; where $l_e \ll w, t \ll L_H, L_\phi, L_{so} \ll L$, with t the sample thickness [5]. By fitting the low-field magnetoresistance data to equation (2.8), the value of the decoherence length, L_ϕ, can be extracted. The value of the decoherence time, τ_ϕ, is then calculated using the equation, $L_\phi = \sqrt{D\tau_\phi}$.

Figure (2.2) shows typical magnetoresistance curves calculated via equation (2.8). The figure shows how the weak localization can be destroyed by a small magnetic field. We have mentioned before that the two partial waves interfere constructively once they arrive back to origin to produce the enhanced backscattering. The effect of the magnetic field is to create a phase difference between the two partial waves. The phase difference created between the two waves is proportional to the magnetic flux penetrating the area enclosed by the two waves. As the magnetic flux changes, the transmission probability oscillates with a periodicity of hc/e; hence making the magnetoresistance of the two trajectories oscillate with the same periodicity [37]. The oscillatory behavior of the magnetoresistance observed near the zero field at low T is known as the Aharonov-Bohm effect. Summing over all electron trajectories with different areas causes the oscillations to average out everywhere except near $B = 0$, where they are all in phase. The result is a peak or dip in the resistance near zero field, depending on the strength of the spin-orbit coupling.

2.3 Decoherence mechanisms in metals

2.3.1 Electron-Electron scattering contribution to decoherence rate

In this section we discuss briefly the effect of Coulomb electron-electron interaction on the phase coherence time, τ_ϕ, in weakly disordered 1D-systems. Physically, the electron-electron scattering is equivalent to the interaction of a conduction electron with the fluctuating electromagnetic field produced by all other surrounding electrons in the system. Due to the statistical nature of the fluctuating field, the e-e scattering is different for each electron, thus the conduction electron loses its coherence The electron-electron scattering time, τ_{ee}, is defined as the time it takes for an electron to be scattered inelastically by another electron. This time scale is temperature dependent. In clean metals, Fermi liquid theory predicts that for electrons sufficiently close to the Fermi surface and at low T, the e-e scattering rate has a T^2 dependence. On the other hand, in weakly disordered 1D-metals, where screening is less effective, the temperature dependence of the electron-electron scattering rate, γ_{ee} was found to be [1, 11]

$$\gamma_{ee}(T) = AT^{2/3} \tag{2.9}$$

with $A = \hbar^{-1}[\pi k_B^2 R/4\nu_F L w t R_K]^{1/3}$, where ν_F is the total DOS at the Fermi energy. Equation (2.9) predicts that the e-e scattering rate vanishes as $T \to 0$. In pure metals and at low T (roughly below 1 K), the electron-electron scattering dominates other scattering processes (see for example reference [5]).

2.3.2 Electron-Phonon scattering contribution to decoherence rate

When the conduction electron is scattered inelastically by phonons, it loses its coherence due to the energy exchange between the electron and the phonon. At high temperatures, the electron-phonon scattering is the dominating source for the decoherence of conduction electrons. The electron-phonon scattering time, τ_{e-ph}, sets the time scale over which the conduction electron is inelastically scattered by lattice vibration (phonon). Each phonon is characterized by its wave vector $\mathbf{q}$. The magnitude of the wave vector of a typical thermal phonon at temperature T is

$$q_T = \frac{k_B T}{\hbar v_s} \tag{2.10}$$

where v_s is the sound velocity in the metal ($\approx$ 2700 m/s in silver). Based on the quantity, $q_T l_e$, the electron-phonon scattering is usually divided into three different regimes; clean, dirty, and intermediate [38]. In the case of clean limit, $q_T l_e \gg 1$. On the other hand, $q_T l_e \ll 1$ for the dirty limit. In the intermediate regime, $q_T l_e \sim 1$. The phonon wave length is defined by $\lambda_T = 2\pi/q_T$. In silver, this reads

$$\lambda_T = \frac{130}{T(\mathrm{K})}\ \mathrm{nm} \tag{2.11}$$

At liquid Helium temperature, $\lambda_T \approx 31$ nm. In our experiments on silver wires, $l_e \approx 32$ nm. That means our experiment falls into the intermediate regime in the vicinity of 4.2 K. The clean limit might be reached at much higher temperatures, where $\lambda_T \ll l_e$. On the other hand, at 40 mK (the base temperature of the dilution refrigerator used in this experiment), $\lambda_T \approx 3250$ nm $\gg l_e$, indicating that there is cross over to the dirty limit. It should be emphasized here that there is no sharp boundary for crossing over from one regime to another.

The temperature dependence of the e-ph scattering rate, γ_{e-ph} takes the form

$$\gamma_{e-ph}(T) = BT^p \tag{2.12}$$

with the exponent of T , $p \approx 2-4$, depending on the specific system and dimensionality. Experimentally, the temperature dependence of γ_{e-ph} reported by various measurements on different material systems are not always in agreement with one another. This issue becomes even more controversial when the dependence of γ_{e-ph} on disorder is concerned [38].

The phonon has two polarization modes: longitudinal and traversal. For metals, above 0.5 K, the longitudinal phonons dominate transversal ones. In the case of clean limit, with no traverse phonons, the decoherence rate of the e-ph scattering is given by [35, 38, 39]

$$\gamma_{e-ph}(T) = \frac{7\pi\zeta(3)E_F^2\nu_F k_B^3}{9\hbar^3\rho v_s^4 k_F^2}T^3 \equiv BT^3 \tag{2.13}$$

where E_F is the Fermi energy (5.6 eV for silver), ρ is the mass density ($10.5\times10^3 \mathrm{kg/m^3}$ for silver), and $\zeta(z) = \sum_k k^{-z}$ is the zeta function ($\zeta(3) \approx 1.2$). For Ag wires, equation (2.13) yields $B_{thy} \approx 0.002$ $\mathrm{ns^{-1}K^{-3}}$. In our experiments on Ag wires and over a wide range of temperatures (40 mK - 18 K), $B_{exp} \approx 0.026$ $\mathrm{ns^{-1}K^{-3}}$, which is higher than the predicted value of equation (2.13). The relatively big difference between B_{thy} and B_{exp}, indicates that the e-ph scattering is not limited to one regime, instead it crosses over between them. At low temperatures, the clean limit is no longer valid, and one has to consider the complete expression of $\gamma_{e-ph}(T)$, given in reference [39], where the temperature dependence is between T^2 and T^4 instead of T^3.

2.3.3 Electron-Magnetic impurity scattering contribution to decoherence rate

In a metal containing a small amount of magnetic impurities, there is an additional contribution to $\gamma_\phi(T)$ from the scattering of the conduction electrons by the magnetic impurities, $\gamma_m(T)$ (also called $\gamma_{sf}(T)$). This is known as the Kondo effect. The conduction electron interacts with the magnetic impurity via the exchange Hamiltonian $H = -J\vec{S}_d.\vec{s}$, where $\vec{S}_d$ and $\vec{s}$ are the spins of the magnetic impurity and the conduction electron, respectively. This exchange interaction between the conduction electron and the magnetic impurity leads to scattering events in which the electronic spin is flipped (with a compensating change of spin on the magnetic impurity). Since the spin of the conduction electron is modified in this inelastic process, the conduction electron loses its coherence. The spin-flip scattering time, τ_{sf}, is defined as the time between scattering events involving an electron and a magnetic impurity such that the electron's spin is flipped. The temperature dependence of $\gamma_{sf}(T)$ has been discussed briefly in Chapter 1, and we will discuss it in more detail in Chapter 3.

2.4 Electron-Electron interaction contribution to resistivity at low T

In a pure metal and at low T (where e-ph interactions are negligible), there are two contributions to resistance; e-e interactions and weak localization. Experimentally, the weak localization can be suppressed by applying a small magnetic field ($\sim$ 30 mT) perpendicular to the film. On the other hand, the electron-electron interaction (EEI) effect has a very small magnetic field dependence, so EEI can not be subtracted out simply by applying a small magnetic field. The contribution of electron-electron

interactions to resistance is given by [11]

$$\Delta R_{ee}(T) \approx 3.126 \, \frac{R^2}{R_K} \frac{L_T}{L} \equiv \frac{C_{thy}}{\sqrt{T}} \tag{2.14}$$

where $L_T = \sqrt{\hbar D / k_B T}$ is the thermal length.

Experimentally, the measurement of the electron-electron interaction contribution to resistance at low T can be used as a thermometer to check the electron's temperature. This is very important at very low temperatures to avoid heating the electrons. At very low T, the drive, V, must be restricted to $eV \lesssim k_B T$, to avoid significant heating of electrons above their equilibrium temperature. If the measured ΔR_{ee} follows equation (2.14), then this is a good sign of the absence of electron heating (see figure (2.3)). On the other hand, if the measured ΔR_{ee} deviates strongly from equation (2.14) and saturates early, then this means that the electron temperature is higher than the bath temperature, which is a sign of electron heating.

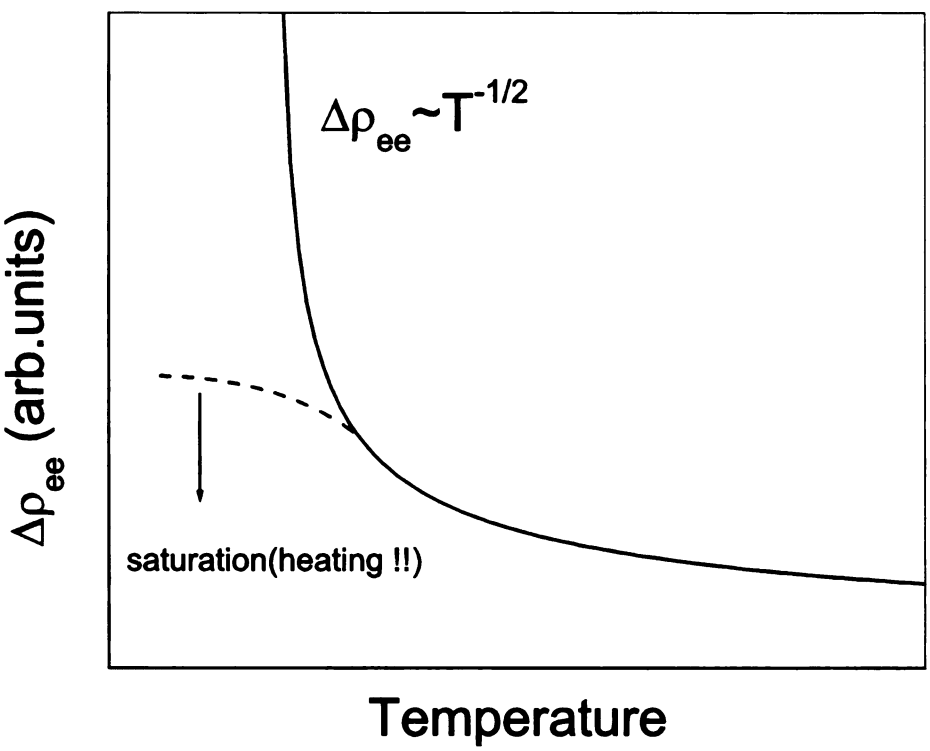

Figure 2.3: Schematic of the contribution of electron-electron interactions to resistivity at low temperatures. The solid line represents equation (2.14), where the electron temperature is the same as the bath one. The dashed line shows the effect of electron heating on the e-e interactions contribution to resistivity.

Chapter 3

Theory II: Kondo Scattering in Dilute Magnetic Alloys

3.1 Magnetic moments in metals

In a pure metal and in the absence of a magnetic field, the ground state of a free electron gas has equal numbers of spin-up ($N_\uparrow$) and spin-down ($N_\downarrow$) electrons. A metal is then nonmagnetic. Introducing a small magnetic field makes the $N_\uparrow \neq N_\downarrow$, hence creating net magnetization given by

$$\mathbf{M} = \chi_P \mathbf{B} \tag{3.1}$$

with $\chi_P = g\mu_B^2 N(\varepsilon_F)/2$ is the temperature independent Pauli susceptibility of the host metal; where $g = 2$ for electrons. Therefore, measurements of the Pauli susceptibility lead to information about the electronic density of states at the Fermi energy.

Experimentally, however, it is often observed that some metals containing a dilute concentration of magnetic impurities show a Curie-Weiss component to the susceptibility, indicating the formation of a local moment. If the system has a number

of magnetic impurities with a concentration of n_s, this component is temperature dependent and has the form [18]

$$\chi_{imp}(T) = n_s \frac{g^2 \mu_B^2 S(S+1)}{3k_B(T+\theta)} \tag{3.2}$$

where g is the Landau g-factor, μ_B is the Bohr magneton, k_B is Boltzman constant, and θ is a constant with a value in the thermal energy range ($0 < \theta < 300\ K$).

In general, the local moment does not always develop, depending on the type of the magnetic impurity and on the metallic host in which the magnetic impurity is embedded. In any Kondo system, the existing models try to answer two basic questions. First, how can a magnetic impurity keep its moment when dissolved in the host metal? Second, if the magnetic moment develops, how does it affect the transport properties of the host? In the next three sections I will use the Anderson model to address the first question and the Kondo model to answer the second question.

3.2 The Anderson model

The Anderson model provides us with a simple picture to understand the mechanism by which it is possible for a 3d transition element to retain a magnetic moment when dissolved in a host metal. For simplicity, consider a $S = 1/2$ magnetic impurity with a single energy level ε_d embedded in a metal host, where $\varepsilon_d < \varepsilon_F$. The Anderson model can be written as [17, 18]

$$H_A = H_c + H_d + H_U + H_{mix} \tag{3.3}$$

Now let us go through the details of each term of the above Hamiltonian.

The first term, H_c, describes the conduction electrons in the host, and using the

second quantization notation, can be written as

$$H_c = \sum_{k\sigma} \varepsilon_k n_{k\sigma} = \sum_{k\sigma} \varepsilon_k c^{\dagger}_{k\sigma} c_{k\sigma} \tag{3.4}$$

where ε_k is the electron energy in state k, $n_{k\sigma}$ is the occupation number of the conduction electrons in state (k,σ), and $c^{\dagger}_{k\sigma}$ and $c_{k\sigma}$ are the creation and annihilation operators for electrons in momentum state k and spin state σ. Using this Hamiltonian, one can easily find the density of states (DOS) of the electrons in the metal host, $DOS(\varepsilon) \propto \varepsilon^{1/2}$. This is shown schematically in figure (3.1). By integrating the quantity, $\varepsilon N(\varepsilon)$, over all filled k and σ states one arrives at the total energy of the conduction electrons in the host.

The second term in the Anderson Hamiltonian, H_d, accounts for the kinetic energy of the d-electrons of the magnetic impurity added to the host and takes the form

$$H_d = \varepsilon_d \sum_{\sigma} n_{d\sigma} = \varepsilon_d \sum_{\sigma} c^{\dagger}_{d\sigma} c_{d\sigma} \tag{3.5}$$

where ε_d is the energy of the d-orbital, $n_{d\sigma}$ is the occupation number of the magnetic impurity in state (d, σ), and $c^{\dagger}_{d\sigma}$ and $c_{d\sigma}$ are the creation and annihilation operators that create or destroy an electron with energy ε_d and spin σ. The number of electrons in the impurity orbital n_d obeys Fermi-Dirac statistics, $n_d = \sum_{d\sigma} n_{d\sigma}$, (i.e. $n_d = 0, 1,$ or 2).

The third term in the Anderson Hamiltonian, H_U, describes the interactions between the d-electrons of the impurity. This term exists only when the impurity is doubly occupied, $n_d = 2$. This term takes the form

$$H_U = U n_{d\uparrow} n_{d\downarrow} = U(c^{\dagger}_{d\uparrow} c_{d\uparrow})(c^{\dagger}_{d\downarrow} c_{d\downarrow}) \tag{3.6}$$

where U is the strength of interaction between the d-electrons.

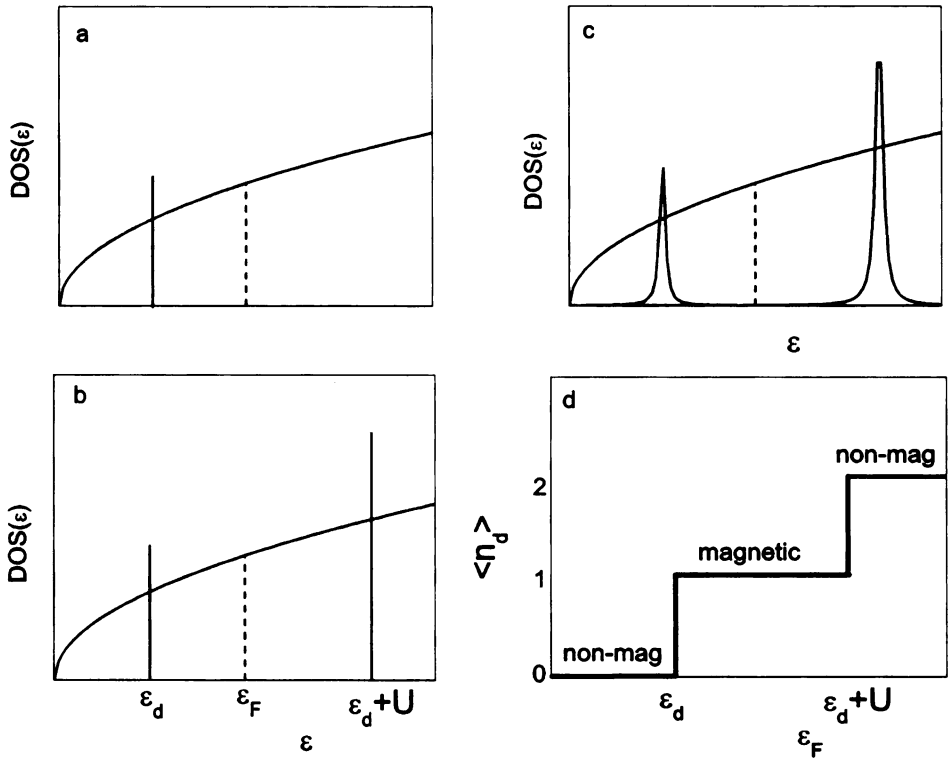

Figure 3.1: Schematic of Anderson model for metal host containing one impurity level, ε_d: (a) DOS for a host metal and an isolated singly occupied impurity level, ε_d. (b) DOS for a host metal and an isolated doubly occupied impurity level, ε_d, with an on site interaction, U. (c) same as in (b), but with mixing between the conduction electrons of the host and the d-electrons of the impurity; this mixing results in an energy broadening of the impurity levels at ε_d and $\varepsilon_d + U$. (d) the average occupation number of the impurity, $\langle n_d \rangle = \langle n_{d\uparrow} \rangle + \langle n_{d\downarrow} \rangle$.

The second and the third terms of the Anderson model, H_d and H_U, describe an isolated magnetic impurity. For an isolated magnetic impurity, there are three energy configurations for the impurity where Fermi-Dirac statistics are obeyed. These configurations depend on the position of the impurity level ε_d relative to the Fermi level ε_F. One can go from one configuration to another by tuning the Fermi energy ε_F around the impurity energy ε_d (see figure 3.1d). First, if $\varepsilon_F < \varepsilon_d$, then the impurity is not occupied with a total energy $E = 0$, since the highest occupied level must be the Fermi level. Second, if $\varepsilon_d < \varepsilon_F < \varepsilon_d + U$, then the impurity is singly occupied with

either spin up or spin down electron with a total energy $E = \varepsilon_d$. Third, if $\varepsilon_d + U < \varepsilon_F$, then the impurity is doubly occupied with a total energy $E = 2\varepsilon_d + U$. Due to partial occupation, the second configuration has two-fold degeneracy corresponding to spin $\frac{1}{2}$, and hence it develops a magnetic moment which will give a Curie law contribution to the susceptibility. The other two configurations are trivial and have no magnetic moments. In this simple picture of the Anderson model, the condition for a local moment to exist is that $\varepsilon_d < \varepsilon_F$, so that it is favourable to add one electron and $\varepsilon_d + U > \varepsilon_F$ so that it is unfavourable to add a second. There is one special case where the single occupation can be non- magnetic. This happens when $\varepsilon_d = \varepsilon_F$, where we have $\langle n_{d\uparrow} \rangle = \langle n_{d\downarrow} \rangle = 1/[exp((\varepsilon_d - \varepsilon_F)/k_B T) + 1] = 1/2$. We will not discuss this case here since we already assumed from the beginning that $\varepsilon_d < \varepsilon_F$.

The last term in the Anderson Hamiltonian, H_{mix}, is the mixing term, which provides a mechanism for electrons in the conduction band to hop onto and off of the impurity site. It can be written as

$$H_{mix} = \sum_{k\sigma} V_{kd}(c^{\dagger}_{k\sigma} c_{d\sigma} + c^{\dagger}_{d\sigma} c_{k\sigma}) \tag{3.7}$$

where V_{kd} is the strength of the interaction. For simplicity, let us assume that V_{kd} is constant, V. This mixing results in an energy broadening of the impurity level ε_d as shown in figure (3.1c).

The transition rate of an electron to hop into and off of the magnetic impurity is given by the Fermi golden rule

$$\frac{1}{\tau} = \frac{2\pi}{\hbar} |\langle V \rangle|^2 N(\varepsilon_d) \tag{3.8}$$

where $N(\varepsilon_d)$ is the DOS of the conduction electrons per spin at the scattering center (i.e. magnetic impurity center). Assuming that $N(\varepsilon_d) = N(\varepsilon_F)$, the total scattering

rate from a number of magnetic impurities with an atomic concentration of c_{imp} is

$$\Gamma = \frac{1}{\tau} = c_{imp}\frac{2\pi}{\hbar}V^2 N(\varepsilon_F) \tag{3.9}$$

using $N(\varepsilon_F) = 1/2\ (3n/2\varepsilon_F)$, this becomes

$$\Gamma = \frac{1}{\tau} = c_{imp}\frac{3\pi n}{2\hbar\varepsilon_F}V^2 \tag{3.10}$$

if $\Gamma \ll U$, it is possible to predict the existence of a local moment in a metal.

The contribution of the magnetic impurities to the resistivity can be calculated from

$$\rho_{imp} = \frac{m}{ne^2}(\frac{1}{\tau}) \tag{3.11}$$

substituting for $1/\tau$ from equation (3.10) we find

$$\rho_{imp} = c_{imp}\frac{3\pi m}{2e^2\hbar\varepsilon_F}V^2 \tag{3.12}$$

This is just a form of potential scattering. It is temperature independent. This result is usually referred as the first Born approximation (second order in the potential strength, V).

In summary, we see that the Anderson model can in principle explain the existence of a local moment for a singly occupied $S = 1/2$ magnetic impurity embedded in a host metal (see figure 3.1d). This model was developed for a single impurity level, ε_d. In the real world, the impurity in principle can have more than one level and furthermore those levels can be split more by the crystal field of the host. Therefore, it seems to be hard to apply this model to real experiments. Nevertheless, it is believed that the Anderson model contains the basic physics one needs to understand other models of transport in Kondo alloys.

3.3 The s-d exchange model

In the previous section and in the context of Anderson model we have discussed the local moment regime, where the magnetic impurity is singly occupied. The condition of single occupation was that $U + \varepsilon_d > \varepsilon_F$ and $\varepsilon_d < \varepsilon_F$. Assuming that the magnetic impurity is in the local moment regime and if the strength of interaction between the localized moment and the conduction electron is sufficiently small (i.e $V_{kd} \ll \varepsilon_d + U$), then the Anderson model goes to what is called the s-d exchange model. The derivation of the s-d exchange model from the Anderson model is referred to as a Schrieffer and Wolff transformation. In the context of the Anderson model, the strength of interaction between the local moment and the conduction electron is described by the parameter V_{kd}. On the other hand, in the s-d exchange model, the interaction strength is described by an effective exchange coupling, $J_{\mathbf{k},\mathbf{k}'}$. The relation between V_{kd} and $J_{\mathbf{k},\mathbf{k}'}$ was first obtained by Schrieffer and Wolff (1966) and takes the form [18]

$$J_{\mathbf{k},\mathbf{k}'} = -|V_{kd}|^2 \left\{ \frac{1}{U + \varepsilon_d - \epsilon_k} + \frac{1}{\epsilon_k - \varepsilon_d} \right\} \tag{3.13}$$

where ϵ_k is the energy of the conduction electron. In the local moment regime, where the magnetic impurity is singly occupied, the effective exchange coupling, $J_{\mathbf{k},\mathbf{k}'}$, between the localized spin and the conduction electron is antiferromagnetic (i.e $J_{\mathbf{k},\mathbf{k}'} < 0$). This can be seen easily from equation (3.13). Since most of the conduction comes from electrons with energies close to Fermi energy, we can set $\epsilon_k \approx \varepsilon_F$. By measuring the energies relative to Fermi energy and setting $\varepsilon_F = 0$, one can see that $\varepsilon_d < 0$ and $U + \varepsilon_d > 0$, hence $J_{\mathbf{k},\mathbf{k}'} < 0$ (i.e antiferromagnetic).

The s-d exchange model already assumes that there is a local moment with spin S which is coupled via an exchange interaction J with the conduction electrons. For

a single impurity in a metal, the s-d exchange Hamiltonian takes the form [18]

$$H_{sd} = -\sum_{\mathbf{k},\mathbf{k}'} J_{\mathbf{k},\mathbf{k}'} \left(\hat{S}^{+} c^{\dagger}_{\mathbf{k},\downarrow} c_{\mathbf{k}',\uparrow} + \hat{S}^{-} c^{\dagger}_{\mathbf{k},\uparrow} c_{\mathbf{k}',\downarrow} + \hat{S}_z (c^{\dagger}_{\mathbf{k},\uparrow} c_{\mathbf{k}',\uparrow} - c^{\dagger}_{\mathbf{k},\downarrow} c_{\mathbf{k}',\downarrow}) \right) \tag{3.14}$$

where $\hat{S}_z$ and $\hat{S}^{\pm} = \hat{S}_x \pm i\hat{S}_y$ are the spin operators of the magnetic impurity with spin S. $J_{\mathbf{k},\mathbf{k}'}$ represents the strength of the interaction between the local moment and the conduction electrons, which will be considered a negative constant, J, in the following derivation. $\mathbf{k}'$ and $\mathbf{k}$ represent the initial and final states of the conduction electron.

The above Hamiltonian contains two types of spin scattering processes; spin-flip and non spin-flip processes (see figure 3.2). While the first two terms in H_{sd}, which includes $\hat{S}^{+}$ and $\hat{S}^{-}$, describe spin-flip processes of the conduction electron, the last term in the parentheses, which includes $\hat{S}^{z}$, describes non spin-flip processes.

To obtain the contribution of the magnetic impurity to the total scattering rate, and hence to the resistivity, we need to calculate the matrix elements of H_{sd} for the four processes mentioned above. Those processes are labeled a, b, c, and d as shown in figure (3.2). For process a, we have

$$\begin{aligned} \langle \mathbf{k}\downarrow | H_{sd} | \mathbf{k}'\uparrow \rangle_a = -J[& \langle \mathbf{k}\downarrow | \hat{S}^{+} c^{\dagger}_{\mathbf{k},\downarrow} c_{\mathbf{k}',\uparrow} | \mathbf{k}'\uparrow \rangle + \langle \mathbf{k}\downarrow | \hat{S}^{-} c^{\dagger}_{\mathbf{k},\uparrow} c_{\mathbf{k}',\downarrow} | \mathbf{k}'\uparrow \rangle \\ & + \langle \mathbf{k}\downarrow | \hat{S}^{z} c^{\dagger}_{\mathbf{k},\uparrow} c_{\mathbf{k}',\uparrow} | \mathbf{k}'\uparrow \rangle - \langle \mathbf{k}\downarrow | \hat{S}^{z} c^{\dagger}_{\mathbf{k},\downarrow} c_{\mathbf{k}',\downarrow} | \mathbf{k}'\uparrow \rangle] \end{aligned} \tag{3.15}$$

The last three terms vanish for the following reasons. In the second term, $c_{\mathbf{k}',\downarrow}$ destroys the state $|\mathbf{k}',\downarrow\rangle$ which is not present, because the initial state is known, $|\mathbf{k}',\uparrow\rangle$. In the third term, $c^{\dagger}_{\mathbf{k},\uparrow}$ creates the state $|\mathbf{k},\uparrow\rangle$ which is not allowed to be created, because the final state is known , $|\mathbf{k},\downarrow\rangle$. The last term has the operator, $c_{\mathbf{k}',\downarrow}$, which destroys the state $|\mathbf{k}',\downarrow\rangle$ which is not present, again because the initial state is known, $|\mathbf{k}',\uparrow\rangle$.

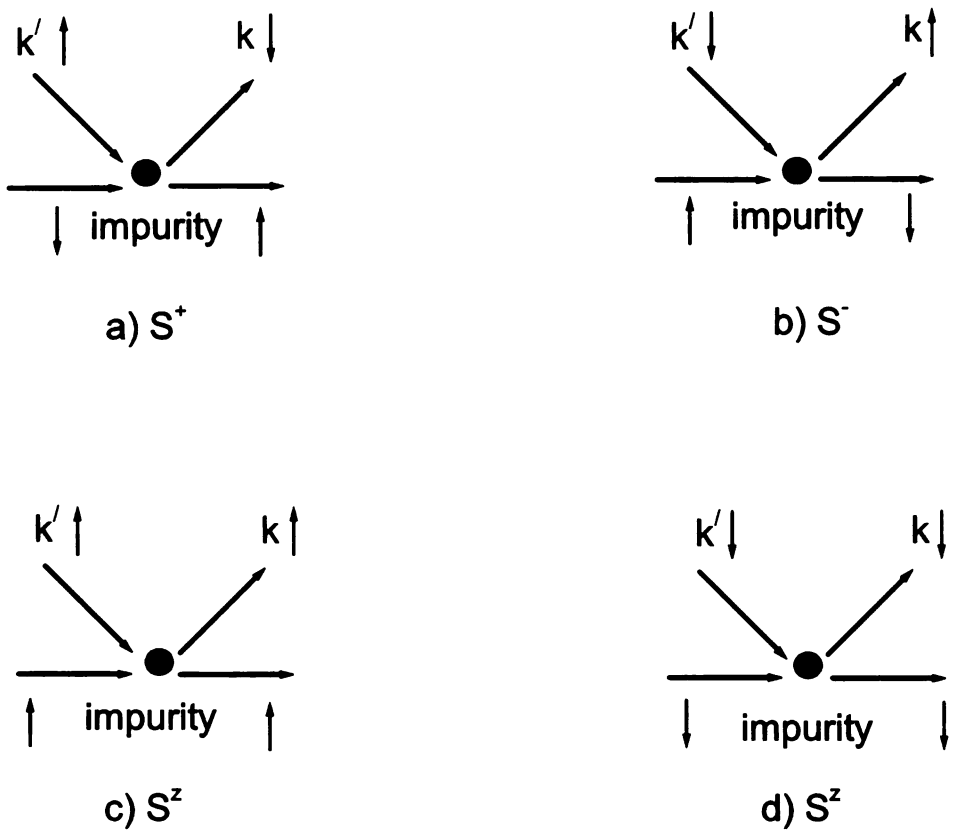

Figure 3.2: Schematic of spin-flip and non spin-flip processes for a conduction electron scattered by magnetic impurity.

Therefore, we end up with the matrix element of the first term only

$$\langle \mathbf{k} \downarrow | H_{sd} | \mathbf{k}' \uparrow \rangle_a = -J\hat{S}^+ \tag{3.16}$$

Similarly for the remaining three processes b, c, and d, we find

$$\langle \mathbf{k} \uparrow | H_{sd} | \mathbf{k}' \downarrow \rangle_b = -J\hat{S}^- \tag{3.17}$$

$$\langle \mathbf{k} \uparrow | H_{sd} | \mathbf{k}' \uparrow \rangle_c = -J\hat{S}^z \tag{3.18}$$

$$\langle \mathbf{k} \downarrow | H_{sd} | \mathbf{k}' \downarrow \rangle_d = +J\hat{S}^z \tag{3.19}$$

The corresponding transition probabilities for the above matrix elements are

$$|\langle \mathbf{k}\downarrow |H_{sd}|\mathbf{k}'\uparrow\rangle_a|^2 = J^2\hat{S}^+\hat{S}^- \tag{3.20}$$

$$|\langle \mathbf{k}\uparrow |H_{sd}|\mathbf{k}'\downarrow\rangle_b|^2 = J^2\hat{S}^-\hat{S}^+ \tag{3.21}$$

$$|\langle \mathbf{k}\uparrow |H_{sd}|\mathbf{k}'\uparrow\rangle_c|^2 = J^2\hat{S}^{z^2} \tag{3.22}$$

$$|\langle \mathbf{k}\downarrow |H_{sd}|\mathbf{k}'\downarrow\rangle_d|^2 = J^2\hat{S}^{z^2} \tag{3.23}$$

where in the last equations I used $(\hat{S}^+)^* = \hat{S}^-$ and $(\hat{S}^-)^* = \hat{S}^+$. The total transition probability, $|\langle V\rangle|^2$, is the sum of the individual probabilities

$$|\langle V\rangle|^2 = J^2(\hat{S}^+\hat{S}^- + \hat{S}^-\hat{S}^+ + 2\hat{S}^{z^2}) \tag{3.24}$$

Using $\hat{S}^+\hat{S}^- + \hat{S}^-\hat{S}^+ + 2\hat{S}^{z^2} = S(S+1)$ and taking matrix elements over the states of the localized spins, we finally find

$$|\langle V\rangle|^2 = J^2S(S+1) \tag{3.25}$$

Substituting this back into equations (3.10) and (3.12), we find for the magnetic impurities contribution to the scattering rate

$$\frac{1}{\tau_m} = c_{imp}\frac{3\pi n}{2\hbar\varepsilon_F}J^2S(S+1) \tag{3.26}$$

And to the resistivity

$$\rho_{imp} = c_{imp}\frac{3\pi m}{2e^2\hbar\varepsilon_F}J^2S(S+1) \tag{3.27}$$

Again this is temperature independent. In summary, it is clear that the first Born approximation is insufficient to explain the anomalies in the resistivity , and hence in the scattering rate. How about going to third order in J ? This is exactly what Kondo did in 1964.

3.4 The Kondo model

Kondo started with the same Hamiltonian of the s-d exchange model discussed in the last section [16]. In addition to the first Born approximation mentioned above, Kondo considered the second Born approximation in his calculations for the scattering rates and found that the scattering of the conduction electrons by magnetic impurities leads to temperature dependent terms in the scattering rates, and hence in the resistivity.

In a metal without magnetic impurities, the conduction electrons can be modeled with the unperturbed Hamiltonian H_0, where the schrodinger equation takes the form

$$H_0\phi_k = E_k^0\phi_k \tag{3.28}$$

where ϕ_k and E_k^0 are the unperturbed wave function and energy of the conduction electron in state k. In the presence of the perturbation H', which is due to dilute magnetic impurities, the schrodinger equation becomes

$$(H_0 + H')\psi_k = E_k\psi_k \tag{3.29}$$

where ψ_k and E_k are the perturbed wave function and energy of the conduction electron in state k. Kondo considered the H_{sd} as the perturbed hamiltonian H' (i.e. $H' = H_{sd}$). Using standard time independent perturbation theory, the solution of the last equation can be written as [40, 41]

$$\psi_k = \phi_k + \sum_n \frac{\langle\phi_n|H'|\psi_k\rangle}{E_k^0 - E_n^0}\phi_n \tag{3.30}$$

It is easily seen that the above solution is not an explicit solution because ψ_k appears on both sides of the equation. To have an approximate solution, the above series solution has to be cut at some order. In the first Born approximation, we stop at the first term, ϕ_k, the wave function of the unperturbed Hamiltonian H_0. This, however,

does not lead to temperature dependent scattering rate as mentioned early. In the second Born approximation, we take the second term into account and in addition we replace ψ_k under the sum by ϕ_k, the unperturbed wave function. Then equation (3.30) becomes

$$\psi_k = \phi_k + \sum_n \frac{H'_{nk}}{E_k^0 - E_n^0}\phi_n \tag{3.31}$$

where H'_{nk} is the transition amplitude $\langle\phi_n|H'|\phi_k\rangle$ of the perturbation H' taken between the unperturbed staes k and n. Now we can use equation (3.31) to calculate the transition probability for an an electron to be scattered from state k to state k' and we get [42]

$$\begin{aligned}
|\langle\phi_{k'}|H'|\psi_k\rangle|^2 &= \langle\phi_{k'}|H'|\psi_k\rangle\langle\phi_{k'}|H'|\psi_k\rangle^* \\
&= \left(\langle\phi_{k'}|H'|\phi_k\rangle + \sum_n \frac{H'_{nk}}{E_k^0 - E_n^0}\langle\phi_{k'}|H'|\phi_n\rangle\right) \times \\
&\quad \left(\langle\phi_k|H'^*|\phi_{k'}\rangle + \sum_m \frac{H'^*_{mk}}{E_k^0 - E_m^0}\langle\phi_m|H'^*|\phi_{k'}\rangle\right)
\end{aligned} \tag{3.32}$$

Using $H'_{k'k} = H'^*_{kk'}$ (i.e. H' is hermitian), the last equation can be written shortly as

$$\begin{aligned}
|\langle\phi_{k'}|H'|\psi_k\rangle|^2 &= \left(H'_{k'k} + \sum_n \frac{H'_{k'n}H'_{nk}}{E_k^0 - E_n^0}\right)\left(H'_{kk'} + \sum_m \frac{H'_{km}H'_{mk'}}{E_k^0 - E_n^0}\right) \\
&= H'_{kk'}H'_{k'k} + H'_{kk'}\sum_n \frac{H'_{k'n}H'_{nk}}{E_k^0 - E_n^0} + c.c + O(H'^4)
\end{aligned} \tag{3.33}$$

Now let us relabel the last equation with the same notations used by Kondo in his original paper [16], where $k = a$, $k' = b$, and $n = c$, then after ignoring the highest order term $O(H'^4)$, we end up with

$$|\langle b|H'|a\rangle|^2 = H'_{ab}H'_{ba} + \sum_c \frac{H'_{ab}H'_{bc}H'_{ca}}{E_a^0 - E_c^0} + c.c \tag{3.34}$$

where a, b, and c denote the initial, the final, and the intermediate states of the

system and E_a, E_b, and E_c are their total energies. Finally, using the Fermi Golden rule, the transition rate from the initial state a to the final state b can be written as

$$W(a \rightarrow b) = \frac{2\pi}{\hbar}\delta(E_a - E_b)\left(H'_{ab}H'_{ba} + \sum_c \frac{H'_{ab}H'_{bc}H'_{ca}}{E^0_a - E^0_c} + c.c\right) \tag{3.35}$$

The first term in the parenthesis, $H'_{ab}H'_{ba} = |H'_{ab}|^2$, represents the first Born approximation, since it involves J^2 as prefactor. The second Born approximation is represented by the second term, where the sum goes over all possible intermediate states c, and it involves J^3 as prefactor. It is the triple product under the sum which yields the temperature dependent scattering rates [42].

Kondo assumed that the scattering of the conduction electron by the magnetic impurity can be divided into two major processes. In the first process, the electron is scattered into an intermediate state by the magnetic impurity which is also scattered to its intermediate state. In the second process, the conduction electron is scattered to its final state while the impurity is scattered back to its original state. The intermediate state may or may not involve spin-flip processes. If the electron spin is flipped in the intermediate state, the impurity spin has to be flipped in order to keep the total spin conserved. It was found only those processes that involve spin-flip result in temperature dependent scattering rates.

Kondo considered four possible configurations for the initial and final states of the conduction electron. The four configurations are $\langle k' \uparrow |H'_{sd}|k \uparrow\rangle$, $\langle k' \downarrow |H'_{sd}|k \downarrow\rangle$, $\langle k' \uparrow |H'_{sd}|k \downarrow\rangle$, and $\langle k' \downarrow |H'_{sd}|k \uparrow\rangle$. In addition, Kondo divided the intermediate state for each configuration into four groups. For more details about those groups, I refer the reader to the original Kondo paper [16]. Starting from equation (3.35) and after a lengthy calculations, Kondo found an expression for the magnetic impurities contribution to the scattering rate given by [16]

$$\frac{1}{\tau_m} = \frac{3\pi n}{2\hbar\varepsilon_F} c_{imp} J^2 S(S+1)\left[1 + 4Jg(\varepsilon_k)\right] \tag{3.36}$$

where

$$g(\varepsilon_k) = \frac{3}{2\varepsilon_F}\left[1 + \frac{k}{2k_F}\ \log\left|\frac{k-k_F}{k+k_F}\right|\right] \qquad \text{for T} = 0, \tag{3.37}$$

This function is singular at $k = k_F$, because the Fermi function has a discontinuity at $k = k_F$. At very low temperatures, $(k - k_F)$ for thermally excited electrons is on average $(k_B T/\varepsilon_F)k_F$. Then equation (3.37) becomes

$$g(\varepsilon_k) = \frac{3}{2\varepsilon_F}\left[1 + \frac{1}{2}\ \log\left|\frac{k_B T}{2\varepsilon_F}\right|\right] \tag{3.38}$$

where I used $k \approx k_F$ and $k + k_F \approx 2k_F$. Substituting this back into equation (3.36), one can see that there are terms in the scattering rate expression proportional to $J^3 \log(T)$. Using equation (3.36) Kondo also calculated the magnetic impurities contribution to the resistivity and found

$$\rho_{imp} = c_{imp}\frac{3\pi m}{2e^2\hbar\varepsilon_F}J^2 S(S+1)\left[1 + 4JN(\varepsilon_F)\ \log\left(\frac{k_B T}{D}\right)\right] \tag{3.39}$$

provided $J < 0$ and $D = 2\varepsilon_F$ is the bandwidth, where the DOS was assumed to be constant. When this magnetic contribution is added to the other contributions to the resistivity, we recover equations (1.7) and (1.8).

Although Kondo successfully explained the temperature dependence of the resistivity not too far below $T = T_{min}$, his calculations break down as $T \to 0$ as discussed in the first chapter. This is known as the Kondo problem. The search for a solution for this problem attracted a lot of theoretical work in the late 60s and early 70s. The main goal of those works was to perform infinite order perturbation in J and sum the most logarithmically divergent terms. In 1965, Abrikosov carried out a summation of these leading order terms for the resistivity [18]. Although he solved the zero temperature divergence in resistivity, he found a more severe divergence, but now, at finite temperature T_K, the Kondo temperature. In summary, the perturbation theory

was good enough to describe the Kondo systems for $T >> T_K$, but could not be extended to the region $T << T_K$. In 1975, Wilson [20] solved the Kondo problem by devising a non-perturbational approach known as the numerical renormalization group (NRG). He showed that at temperatures far below the Kondo temperature ($T \ll T_K$), the spin of the magnetic impurity is totally screened by the conduction electrons. For conduction electrons, the screened impurity appears then as a potential scattering center, hence the resistivity saturates. His approach was successful in predicting most of the thermodynamic properties of many dilute Kondo systems.

3.5 Adding the decoherence rates

Consider two time-reversed paths (1 , 2) that start and end at the origin, and a magnetic impurity, with spin S, sitting somewhere along the path. Let $\vec{R}_{imp}$ be the position of the magnetic impurity relative to the origin. In principle, there is a finite probability for the conduction electron to follow either of the two paths. If the conduction electron follows the first path, it will arrive at $\vec{R}_{imp}$ after a time τ_1 and interact with the magnetic impurity there. On the other hand, if the conduction electron follows the second path (time-reversed path), it will arrive at $\vec{R}_{imp}$ after a time τ_2. As a result, the conduction electron may have two spin-flip events at $\vec{R}_{imp}$. The time difference between the two events is $|\tau_2 - \tau_1|$. During this time difference and due to the dynamics of the magnetic impurity, it may interact with other thermal electrons (with energy of order $k_B T$) from outside the loop, and the spin orientation of the magnetic impurity may change. This means that the spin configuration of the magnetic impurity may or may not be the same for both events. The time scale at which the magnetic impurity re-orients or relaxes is called the Korringa time, τ_K. It was found that the Korringa rate, γ_K, varies linearly with temperature and can be

written as [43]

$$\gamma_K = \frac{1}{\tau_K} = \frac{\pi}{\hbar} J^2 S(S+1) \nu_F^2 k_B T \tag{3.40}$$

where ν_F is the total DOS at the Fermi level. On the other hand, we found early in this chapter that the magnetic scattering rate (in the limit $T > T_K$) scales linearly with the concentration of the magnetic impurities and takes the form

$$\gamma_m = \frac{1}{\tau_m} = \frac{\pi}{\hbar} J^2 S(S+1) \nu_F n_s \tag{3.41}$$

The ratio of the two rates becomes

$$\frac{\gamma_m}{\gamma_K} = \frac{n_s}{\nu_F k_B T} \tag{3.42}$$

Below the Kondo temperature T_K, where the magnetic impurity is screened, the Korringa rate saturates and then the ratio reads

$$\frac{\gamma_m}{\gamma_K} = \frac{n_s}{\nu_F k_B T_K} \tag{3.43}$$

For a Ag host, where $\nu_F = 1.03 \times 10^{47} J^{-1} m^{-3}$ and $k_B = 1.38 \times 10^{-23} J K^{-1}$, this reads

$$\frac{\gamma_m}{\gamma_K} = 4.15 \times 10^{-2} \frac{n_s(ppm)}{T_K(K)} \tag{3.44}$$

where the concentration is now expressed in ppm unit and as usual T_K in Kelvin. In the next section, we will see that the ratio, $\gamma_m/\gamma_K \ll 1$, is the same as the criterion of the validity of Micklitz's theory.

The conduction electron can be treated quantum mechanically as if it is composed of two partial waves traversing the loop in opposite directions. Once the two partial waves arrive back to the origin, they will interfere constructively or destructively depending on the final spin states of the two partial waves . If the two partial

waves do not undergo any spin rotation on the conjugated paths, then their final spin states will be the same and they will interfere constructively. Decoherence results from non-commutation of the spin rotation operators the electron experiences as it traverses the loop in opposite directions. There are two limits to the spin-induced decoherence depending on how fast the impurity will be randomized. The two limits are controlled by the ratio γ_m/γ_K. If $\gamma_m < \gamma_K$, then the impurity spin will randomize quickly after the first spin-flip event, hence the two partial waves will see the same average spin orientations of the magnetic impurities. On the other hand, if $\gamma_m > \gamma_K$, then the magnetic field created by the magnetic impurities is no longer random, hence the decoherence rate is doubled. The contribution of magnetic impurity scattering to the total decoherence rate in the spin-singlet channel of the weak-localization magnetoresistance can be written as [43]

$$\gamma_\phi = \gamma_{in} + \gamma_m \qquad \text{for} \quad \gamma_m < \gamma_K \tag{3.45}$$

$$\gamma_\phi = \gamma_{in} + 2\gamma_m \qquad \text{for} \quad \gamma_m > \gamma_K \tag{3.46}$$

where γ_{in} is the dephasing rate due to electron-electron and electron-phonon scattering. In summary, I want to emphasize that it is the ratio γ_m/γ_K that determines which equation to be used for adding the decoherence rates.

3.6 The theories of Zarand and Micklitz (Numerical Renormalization Group technique)

Although Wilson solved the Kondo problem in 1975, there was no calculation of the inelastic scattering rate until the paper of Zarand *et al.* [28] in 2004. In their work, Zarand *et al.* used the numerical renormalization group (NRG) method to study the complete energy dependence of the inelastic scattering cross-section, $\sigma_{inel}(\omega, T = 0)$,

of the conduction electrons scattered by a spin 1/2 magnetic impurity at $T = 0$. The theory of Zarand predicts that the the inelastic scattering cross-section, $\sigma_{inel}\ (\omega, T = 0)$, has only a very weak (logarithmic) energy dependence above T_K, has a broad maximum around T_K, scales approximately linearly with ω for $0.1T_K < \omega < T_K$, and crosses over to a $\sim \omega^2$ behavior for very small energies, $\omega < 0.1T_K$. The inelastic scattering rate of the conduction electrons scattered by a magnetic impurity, $\gamma_m\ (\omega, T = 0)$, is proportional to the inelastic scattering cross-section, $\sigma_{inel}\ (\omega, T = 0)$. Although Zarand *et al.* computed $\sigma_{inel}\ (\omega, T = 0)$, they believe that $\sigma_{inel}\ (\omega = 0, T)$ has a similar form.

In 2006 Micklitz *etal.* [27] showed that the dephasing rate due to magnetic impurities measured in a weak localization experiment, $\gamma_m\ (T)$, is directly related to the inelastic cross section, $\sigma_{inel}\ (\omega)$, calculated by Zarand *et al.* [28]. In other words $\gamma_m\ (T) \propto \sigma_{inel}\ (\omega)$. According to this theory, the effect of a small concentrations, n_s, of spin 1/2 magnetic impurities on the dephasing rate can be explored from $T \gg T_K$ all the way down to $T \ll T_K$. This theory is valid in the limit of small concentrations, and this condition can be written as

$$\frac{n_s}{\nu_F k_B T_K} \ll 1 \tag{3.47}$$

where ν_F is the DOS at the Fermi level per spin degree of freedom , k_B is the Boltzmann constant, and T_K is the Kondo temperature of the system under study.

Furthermore, the theory of Micklitz predicts that if the density n_s of magnetic impurities is sufficiently low, the magnetic scattering rate, $\gamma_m(T)$, is a universal function, $\gamma_m(T) \propto n_s f(T/T_K)$, and depends only on two parameters, n_s and T_K. The calculated magnetic scattering rate, $\gamma_m(T)$, for a weakly disordered 1D-system is shown in figure (3.3). The figure shows that $\gamma_m(T)$ is almost constant for $T > T_K$. For $T \lesssim 0.3\ T_K$, $\gamma_m(T)$ varies linearly in T and at very low temperatures, one obtains the expected T^2 behavior. The figure also shows that the maximum value of $\gamma_m(T)$ occurs

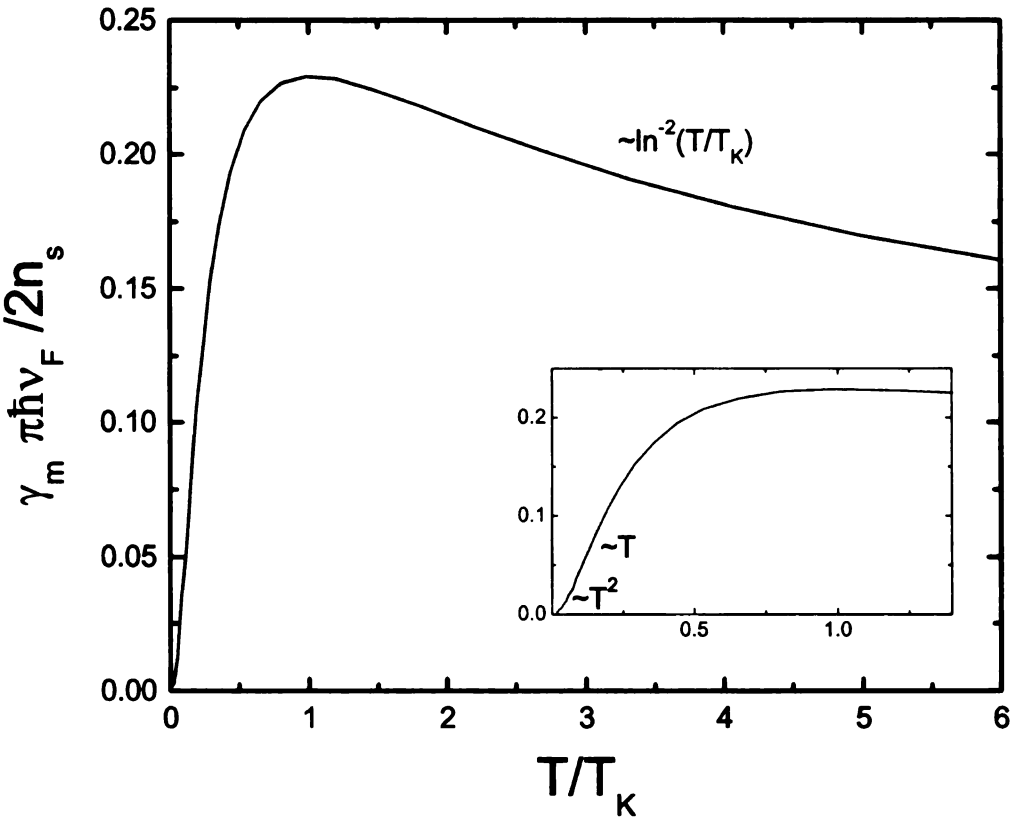

Figure 3.3: Magnetic scattering rate due to diluted magnetic impurities embedded in weakly disordered 1D-metal host calculated via NRG [27]. The inset is a blow up of the low temperature region.

at $T = T_K$. This maximum scales linearly with the concentration of the magnetic impurities and can be written as

$$\gamma_m^{max}(T = T_K) = 0.23 \times \frac{2n_s}{\pi\hbar\nu_F} \tag{3.48}$$

For a Ag host, where $\nu_F = 0.515 \times 10^{47} J^{-1} m^{-3}$, this reads

$$\gamma_m^{max}(T = T_K) \approx 1.59 \times n_s(ppm)\ ns^{-1} \tag{3.49}$$

In our work, we compare our results with Micklitz's theory, which provides us with the calculated dephasing rate due to magnetic impurities in a weakly disordered metal

as measured in a weak localization experiment.

In any Kondo system, there are three major sources of electron dephasing; electron-electron, electron-phonon, and electron-magnetic impurity interactions. Assuming that the three rates are independent, then the total scattering rate will be the sum of them (Matthiessen's rule). In the context of Micklitz's theory, this is not strictly correct. The theory of Micklitz provides us with a new way of adding the dephasing rate due to e-e interactions with the rate due to all other processes including γ_m. At very low temperatures, where the e-ph interaction is negligible and assuming that there are only two sources of dephasing; e-e and e-magnetic impurity interactions, the total dephasing rate, in the context of Micklitz's theory, can be written as [27]

$$\gamma_\phi = \kappa T \sqrt{\frac{1}{\gamma_\phi}} + \gamma_m \tag{3.50}$$

where the first term represents the e-e contribution to the dephasing rate and the second term describes the dephasing rate due to the magnetic impurities, $\kappa = A^{3/2}$, where $A = \hbar^{-1}[\pi k_B^2 R/4\nu_F L w t R_K]^{1/3}$ (see equation 2.9). Rearranging the last equation yields γ_m

$$\gamma_m = \gamma_\phi - \kappa T \sqrt{\frac{1}{\gamma_\phi}} \tag{3.51}$$

We see that the last equation deals only with two dephasing sources ; e-e and e-magnetic impurity interactions. However, experimentally, the total dephasing rate, γ_ϕ, may contain additional dephasing sources such as scattering of the conduction electrons by both phonons and low T Kondo impurities. Those additional sources are non avoidable, and they exist in both the pure and the implanted samples, since all of our samples have been evaporated from the same source and at the same time. In our work, we first fit the total dephasing rate of the pure sample, assuming that it contains three dephasing sources; e-e, e-ph, e- low T Kondo impurity interactions, then we subtract this total dephasing rate out from the implanted samples to end

up with, γ_m, the scattering rate due to the implanted magnetic impurities. We have compared the results of analyzing our data with equation (3.45) and with equation (3.50), and we found that the difference is at most 15% for the 2 ppm sample at the lowest temperature.

3.7 Impurity-Impurity interaction

So far, we have been talking about the Kondo effect, which deals with non-interacting or very dilute magnetic impurities dissolved into a non-magnetic metals. This is called the Kondo regime, where the magnetic impurity concentration has to be very small to avoid impurity-impurity interactions. It is also sometimes called the single impurity limit. Historically, a reasonable approximation for this regime is to work at impurity concentrations below 100 ppm [44] .

In practice, the single impurity limit is difficult to realize, since the impurity-impurity interaction is present and falls off rather slowly as $(1/r^3)$. This coupling between the magnetic impurities is known as Ruderman, Kittel, Kasuya, Yosida (RKKY) interaction, named after its discoverers [45, 46, 47]. In highly concentrated Kondo alloys, the RKKY interactions lead to a spin glass transition at a temperature T_{sg}, which is given by [48]

$$T_{sg} = \frac{4n_s}{\pi k_B \nu_F \ln^2(v_F \hbar n_s^{1/3}/k_B T_K)} \tag{3.52}$$

where ν_F and v_F are the total DOS at the Fermi level and the Fermi velocity of the host. For Ag host, where $\nu_F = 1.03 \times 10^{47} J^{-1} m^{-3}$ and $v_F = 1.39 \times 10^6 m s^{-1}$, we find

$$T_{sg} = \frac{5.285 \times 10^{-2}\ n_s(ppm)}{\ln^2(413.295\ n_s^{1/3}(ppm)/T_K(K))} \tag{3.53}$$

where again the concentration is expressed in ppm unit and both T_K and T_{sg} are in

Kelvin. For Fe impurities with a concentrations of 2 and 10 ppm , and assuming that $T_K = 4K$, the corresponding T_{sg}'s are 4.5 and 18 mK, respectively. To avoid the RKKY interactions, one has to work at temperatures higher than the spin glass transition temperature of the system under study, i.e. $T > T_{sg}$. In our experiment, the working temperatures is always higher than 40 mK, which is the base temperature of the Oxford dilution refrigerator used in this work, hence our experiment is not sensitive to the RKKY interactions.

Chapter 4

Experimental Methods

4.1 Introduction

In this chapter I discuss the experimental methods used in this work to fabricate, characterize, ion-implant, and measure our samples. First, I will go over sample fabrication. This includes wafer processing, electron-beam writing, evaporation and lift-off, and ion implantation. Second, I will discuss the measurement methods. The latter includes testing the samples at room temperature, dilution refrigeration, and weak localization magnetoresistance circuitry. Finally, I discuss the use of weak localization magnetoresistance to determine the phase coherence time of conduction electrons in our samples.

4.2 Sample fabrication

4.2.1 Wafer processing

In this work, I used 4-inch oxidized silicon wafers. The thickness of the oxide layer was 300 nm. The first thing to do was to cut the wafer into pieces 5 $mm \times 5$ mm in size using a MicroAutomation 1006 Dicing Saw. But before dicing, we have to protect the surface of the wafer from scratches, residuals that may come off during

Material	Silicon
Wafer Diameter (mi)	4000
Wafer thickness (mi)	20
Tape thickness (mi)	4
First index (mm)	5
second index (mm)	5
Hight (mi)	16
depth of cut (mi)	8
Angle (deg)	90
Feed speed (rpm)	200

Table 4.1: The parameters used to programm the dicing Saw to cut 4 inches Silicon wafer into 5 mm squares. 1 inch = 1000 mils.

the dicing process, or from any other contamination sources. To do that I first cover the surface of the wafer by a thick layer of e-beam resist, bake it for half an hour, and then take it to be cut. All sample fabrication steps were done inside the clean room except the dicing which was done outside where the Saw is located. The wafer was then placed, facedown, on a sheet of kapton film with holes punched through to allow a vacuum chuck to hold the wafer on the saw. The kapton film is important to reduce scratching of the surface and to help sliding the wafer to the edge while the vacuum is on, after the dicing is done. This is important, because once the dicing is done if one turns the vacuum off, the wafer will pop up and break apart. Instead one has to slide the kapton film to the edge while the vacuum is on, and then take out the wafer. I usually dice the wafer from the back side, since the wafer will be covered again by e-beam resist for writing purposes, and I do not dice it deeply. The depth of cut was usually taken to be one-third of the thickness of the wafer. In this way, the wafer would not break apart if handled carefully. The Saw can be programmed to define the characteristics of both the wafer and the size of the chips need to be cut. Table (4.2.1) lists the parameters used in dicing 4 inch Silicon wafers.

Once the wafer is cut not too deeply from the back side, I take it back to the clean room to create a bi-layer of resist which will be used in the e-beam writing process. Having two layers of resist is crucial to form a nice undercut. The two

types of resist were chosen in a way that the lower resist has higher sensitivity to both electron exposure and developer than the top layer. Therefore, the lower layer will be removed more easily than the top, forming an undercut (see figure 4.1b). In this work, I used two type of resists to create the lower and the top layers. The lower layer was created by dropping copolymer of P(MMA(8.5)MAA) 9% in ethyl lactate on the surface of the wafer (see figure 4.1a). The wafer is then spun at 6000 rpm for 50 seconds. The centrifugal force spreads the resist across the wafer, and a desired thickness of the resist can be achieved by selecting an appropriate spin speed. Spinning the wafer this way removes excess material and forms a smooth, uniform layer across most of the wafer. After spinning the resist, the wafer is placed on top of a hotplate and baked at 170 degrees Celsius for half an hour. The e-beam resist is suspended in solvent, therefore by baking the wafer, the solvent will evaporate leaving a hard layer of resist sitting on the Silicon substrate. The second layer of resist was created by dropping 495 PMMA 4% in chlorobenzene on top of the first layer. The wafer is then spun at 6000 rpm, and baked at 170 degrees Celsius for one hour.

Now the wafer is ready to be broken apart into small squares ($5\ mm \times 5\ mm$). Since the thickness profile of the resist on the Silicon substrate is not uniform near the edges of the wafer, I discard the chips which are far away from the center and close to the edge of the wafer. Then I check each single chip using the optical microscope to find which chips are clean enough to be used in the writing process.

4.2.2 Electron beam lithography; preparing the electron microscope for writing

SEM column description

Electron-beam lithography is the technique that enables small patterns to be transferred to a substrate. Once the resist is baked, the chip is ready to be loaded into

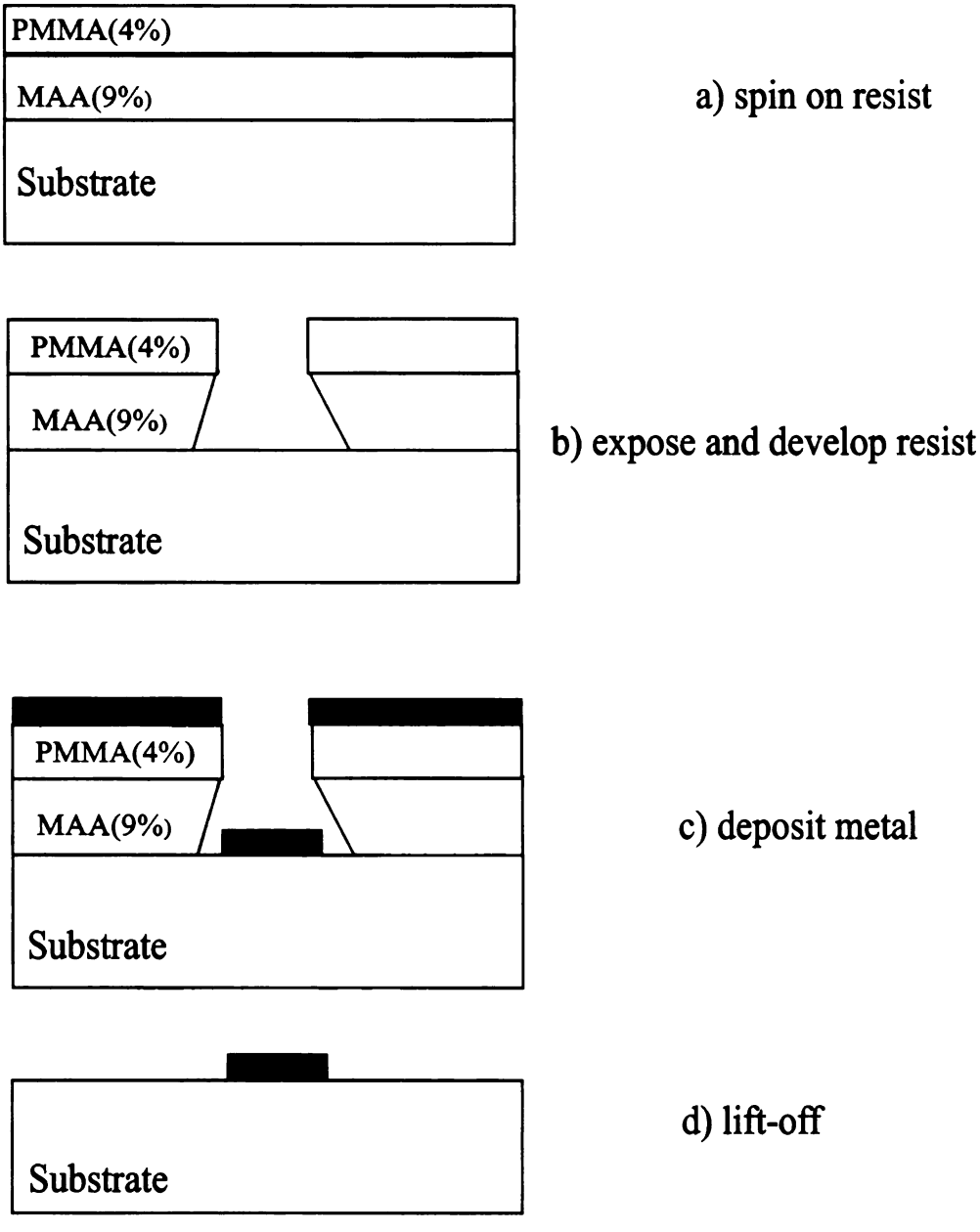

Figure 4.1: Cartoon showing the basic steps in EBL. (a) Covering the substrate by bi-layer resists. (b) Exposing and developing the resist. (c) Metal deposition. (d) lifting-off the resists and excess metal.

the electron microscope. In this work, I used a JEOL model JSM-840A scanning electron microscope with a tungsten filament. The electron microscope column is the most critical part of any electron beam lithography system. It consists of the electron source, an alignment system for centering the beam in the column, apertures, a beam blanker for shuttering the beam, several lenses for focusing the electron beam, and a stigmator used for correcting astigmatism in the beam [49]. A typical electron beam column is shown in Figure (4.2).

Saturating the filament and beam current stability

After loading the sample into the microscope, I usually wait from 5-10 minutes for the column to pump down to $\sim 1 \times 10^{-6}$ Torr, then I start slowly saturating the filament. The tungsten filament is heated by passing current through it and electrons are emitted thermionically from it. The current passing through the filament is called filament current. It may take around 5 minutes to fully saturate the filament. The filament itself is kept at high negative voltage compared with the anode, which is at ground or zero potential. Therefore, the anode is positive with respect to the filament, causing the electrons emitted from the filament to be accelerated toward the anode. In all samples I fabricated, both the accelerating voltage and the working distance were fixed to 35 keV and 25 mm, respectively. The anode has a small hole (aperture), which allows some electrons to pass through and travel down the column forming what is called the beam current. Some small holes in the sample holder were designed to measure the beam current. I focus the beam into one of the holes, and turn on the current meter to watch the beam current. Initially, I set the beam current to around ~ 7 pA and wait at least half an hour for the current to be stable. For a new filament, it may take from 1-2 hours for the beam current to get stable. On the other hand, after a few runs, the filament will be cooked well and then it takes less time for the beam current to get stable.

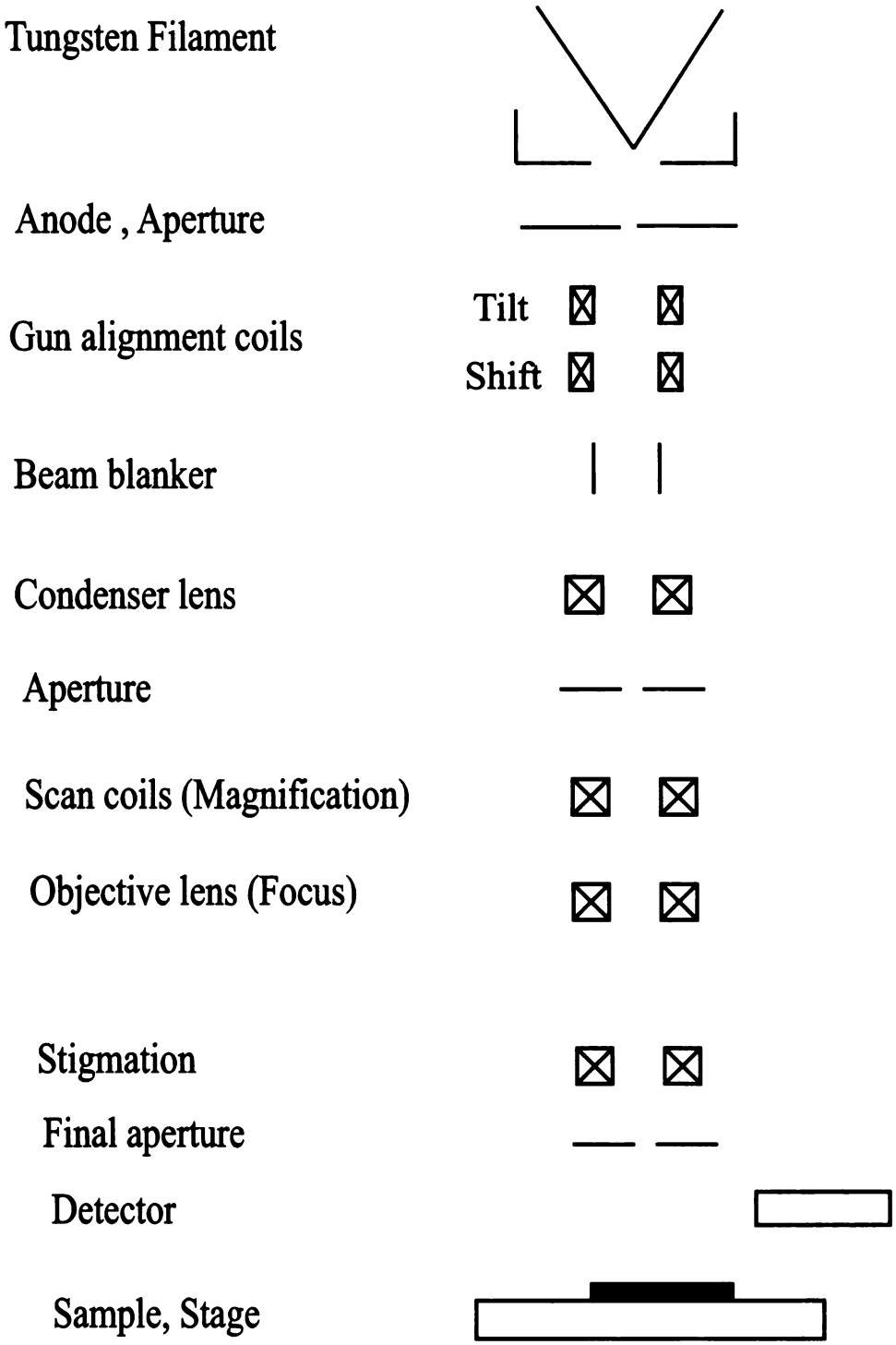

Figure 4.2: Schematic diagram showing the basic components of the JEOL microscope column.

Gun alignment and beam current adjustment

Once the current becomes stable, I check the gun alignment to maximize the current in the column. The gun is properly aligned if the direction of the beam current is parallel to the axis of the column. This is important because I use three current settings in writing my pattern; low current setting (25 pA) to write the smallest features (wires), intermediate current setting (0.5 nA) to write the intermediate features (leads), and high current setting (40 nA) to write the big features (pads). If the gun is not properly aligned, the high current setting will not be reached. On the other hand, if the filament has been used many times, it will not provide high currents; in this case the filament needs to be replaced. While checking the high current setting, I usually check the performance of the beam blanker. The beam blanker is used to turn off or blank the beam. This is necessary when the beam needs to be moved from one part of the wafer to another. Typical ramp times for the beam blanker are 3 - 5 μs.

Focusing and stigmating the beam

Next, I start focusing and stigmating the beam. To do this, I use a test sample that contains circles, horizontal and vertical lines of 120 nm thick Ag. I usually focus and stigmate at the same current used to write the smallest features in my pattern (namely at $I \approx 25$ pA). I start this process by focusing on Ag lines which are at right angles with the magnification all the way up to 100,000, then I use the two stagmator correction knobs (x, y), in combination with the focus knob to get the sharpest image. I repeat this step several times at higher magnifications, until a sharp image is obtained at 300,000. Then I go to the real chip to focus on it. For this purpose, I usually make two scratches at the right and left sides of the chip to be used for focus purposes. I first focus on the right scratch and record the angular position of the focus knob, second I focus on the left scratch and record the the angular position of the focus knob, and finally I set the focus knob in between the two position to

correct for tilting the substrate. Now the microscope is ready to start the writing process. At this point I usually turn off both the detector and the current meter to reduce the amount of noise inside the chamber.

Pattern design, run file creation, and pattern writing

The JEOL - SEM I used is fed with the Nanometer Pattern Generation System (NPGS), which controls the pattern generation process. This process can be divided into three main steps; designing the pattern, creating the parameter run file, and writing the pattern [50]. My patterns were designed using DesignCAD LT2000. Once the pattern is designed, NPGS creates a run file which is used to record the exposure conditions for each layer in the pattern. A typical run file contains information about the dose, the magnification, and the measured beam current for every single layer in the pattern. In writing the pattern, I used two types of doses; area dose ($\mu C/cm^2$) and line dose (nC/cm). The line dose was used to write the smallest features (i.e the wires). A typical line dose was 6.5 nC/cm. The area dose was used to write the small four-terminal pads attached to the wire, the leads, and the big pads. A typical area dose was 250 $\mu C/cm^2$. If the user enters the dose into the run file, the point exposure time will be calculated automatically.

My pattern consists of four main layers. The first layer contains information about the parameters used to write the wire. This layer was written at magnification of 800. The line dose and the measured beam current were 6.5 nC/cm and 25 pA, respectively. The second layer represents the small pads attached to the wire. This layer was written also at the same magnification and the measured beam current of the first layer, but instead with an area dose of 250 $\mu C/cm^2$. The third layer was used to write the small leads which are close to the wire. This layer was written at a magnification of 100. The area dose and the measured beam current of this layer were 250 $\mu C/cm^2$ and 0.5 nA, respectively. Finally, the last layer was used to write the

outer leads, the big pads, and the guards. This layer was written at a magnification of 20. The area dose and the measured beam current of this layer were 250 $\mu C/cm^2$ and 40 nA, respectively. The run file also provides an option to correct for the unwanted offset that occurs when the magnification or the beam current is changed between different layers. This option allows the origin of a single layer of a pattern to be offset from the origin of the total pattern, which is always at the center of the field of view of the microscope. This offset has to be tested experimentally, and then corrected for in the run file. In my pattern, when the magnification and the beam current change from 800 and 25 pA to 100 and 0.5 nA, the offset was (-33, -15) μm. To correct for this shift, I entered (33, 15) μm in the run file. Similarly, when the magnification and the beam current change from 100 and 0.5 nA to 20 and 40 nA, the offset was (-191, -82) μm. Again, to correct for this shift, I entered (191, 82) μm in the run file.

Once the run file has been created, the NPGS program starts the writing process. This program reads the run file and calls the writing program (PG). Typical total writing time of my pattern was around 8 minutes. Each chip contains two identical samples (two patterns), so the total writing time for each chip is around 16 minutes. After writing each layer in the pattern, the program asks the user's permission to start writing the second layer. Before hitting enter, one can change quickly the magnification and the beam current as desired.

4.2.3 pattern development, evaporation and lift-off

After the patterns have been written by EBL, the exposed areas have to be removed from the surface using the appropriate developer. When the electron beam interacts with the resist, it breaks the bonds inside the resist, which makes it more soluble in an organic solvent (developer). In this work, the developer used was methyl isobutyl ketone (MIBK), 99+% pure. This MIBK developer was diluted to 1:3 with isopropyl alcohol (IPA). To develop the patterns, I use three small beakers. The first beaker is

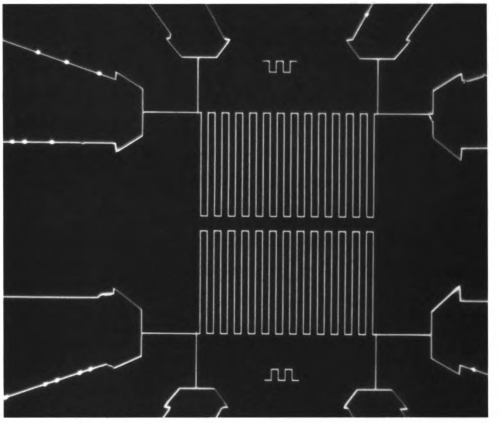

Figure 4.3: Optical microscope picture of the pattern after development.

filled with the developer(MIBK) and placed inside an ultrasonic bath. The second and third beakers are filled with alcohol (IPA) and deionized water (DIW), respectively. To develop, I swirl the chip for 50 s in the MIBK solution, 10 s in the IPA, and finally 20 s in the DIW. Then I take it out and immediately dry it with N_2 gas. To check the development performance, I look at the chip using the optical microscope. If the pattern is not completely developed, I follow the above procedure for 5-10 s as needed. Figure (4.3) shows the pattern after it had been developed. Once the patterns have been developed properly, the chips are ready to be transferred to the thermal evaporator for Ag deposition.

An Edwards 306 thermal evaporator was used for this purpose. In this run, I loaded 18 chips into the evaporator, to be evaporated at the same time. All sam-

ples were evaporated at the same time to make sure that all of them have the same microstructure and the same amount of disorder (i.e same diffusion constant). Each chip contains two samples on it, so in total I have more than 30 samples. A Molybdenum boat was used on which pellets of 99.9999% pure Ag are placed. The chips are mounted about 30 cm directly above the source. The chamber is then pumped down for one hour to a vacuum of about 10^{-6} Torr. After one hour of pumping down and keeping the shutter closed, I melt the source by passing a current of about 1.8 A into the boat. At this point the source melts and the chamber pressure goes up, therefore I wait one more hour for the chamber pressure to come down to 10^{-6} Torr. Melting the source first helps cleaning the source and baking the chamber at the same time. This step is important to get very pure Ag samples. One hour after melting the source, I add Liquid N_2 to the cold trap. This helps lowering the pressure by freezing the water vapor and other contaminations to the walls of the cold trap. One hour after adding liquid N_2, the chamber pressure goes down to around 10^{-7} Torr. The total pumping time from closing the chamber to starting a real evaporation is around three hours.

Now the chamber is ready to start the evaporation. I start the evaporation process by passing the current slowly into the Molybdenum boat. I usually increase the current by 0.2 A every 15 s. During this heating process and if the chamber pressure goes up, I wait until the pressure falls again. When the current reaches roughly 1.8 A, the Ag starts to evaporate at a small rate. The evaporation rate is measured using a crystal thickness monitor, which is placed next to the mounted chips. Once the evaporation rate approaches 2 $\mathring{A}/s$, I open the shutter and zero the thickness monitor. When the desired thickness (45 nm) is deposited, I close the shutter and decrease the current fast. Then I wait around 20 minutes to let the chamber cool down before I open it to air.

Once the samples are taken out of the evaporator, they are ready for lift-off of the

excess metal. First, I fill a small beaker with Acetone, and then set it on a hotplate. Once the Acetone starts boiling (at $65°C$), I take the beaker out of the hotplate and immediately place one sample face up at the bottom of the beaker. One may need to agitate the solution by rotating the beaker and using an eyedropper to speed up the process by flushing the surface with hot Acetone. After a few minutes, the excess metal and the resist will be removed, then I take the sample out and immediately wash it with IPA and dry it with N_2 gas. Finally, I use the optical microscope to check the sample quality. One can use the dark image option in the optical microscope to check the continuity of the wire and the other leads. It is not recommended to use the SEM to check the sample, since the electron beam may harm the wire. I follow the same procedure to lift-off the other samples. Figure (4.4) shows one of the evaporated wires. Once done, I keep my samples in a safe holder and then take them outside the clean room to start preparing for the next step; ion-implantation of the samples.

4.2.4 Ion implantation

Ion implantation is a process by which ions of a material are accelerated to a high energy and speed to be injected into a solid. A typical ion implantation experiment consists of an ion source, where ions of the desired element are produced, an accelerator, where the ions are accelerated to a high energy, and a target, where the dopant ions come to rest. When the ions collide with the surface, they lose their energy due to collisions with target electrons, and finally come to rest at some depth in the target. The penetration depth depends on the ion type, ion energy, and the composition of the target.

The amount of ions that is delivered to the target is known as the dose and this can be accurately measured by monitoring the ion beam current. The total number of ions incorporated into the solid is determined by the ion flux and the duration of implantation. In this work, the target was Ag and the implanted ions were Fe. The

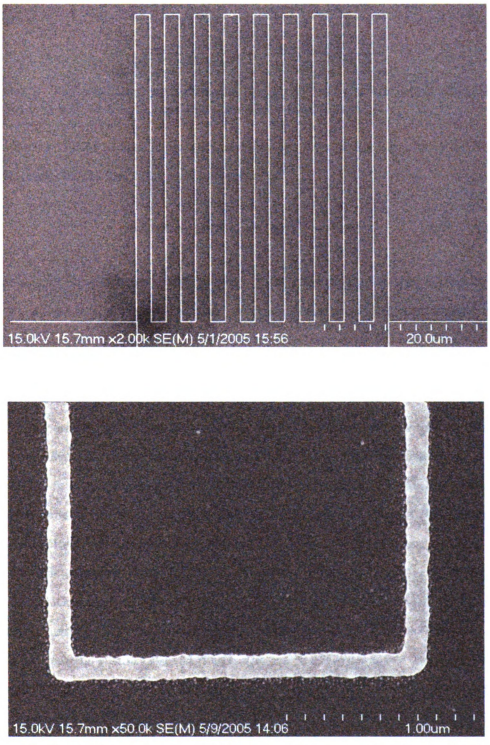

Figure 4.4: SEM picture of silver wire after evaporation and lift-off. The width of the wire is around 130 nm.

$n_s(ppm)$	$n_s(cm^{-3})$	$Area\ Dose(cm^{-2})$
2	11.8×10^{16}	0.53×10^{12}
6	35.4×10^{16}	1.59×10^{12}
10	59×10^{16}	2.66×10^{12}

Table 4.2: The calculated area doses for three different concentrations of the implanted ions into 45 nm Ag host, calculated from equation (4.1).

area dose is defined as the concentration of the ions incorporated into the solid times the thickness of the film. This can be written as

$$AreaDose(cm^{-2}) = n_s(cm^{-3}) \times t(cm) \tag{4.1}$$

where $n_s(cm^{-3}) = n_s(ppm) \times 10^{-6} \times n(cm^{-3})$, n is the particle density of the target (for Ag $n = 5.9 \times 10^{22} cm^{-3}$), $n_s(ppm)$ is the concentration of the implanted ions expressed in units of ppm, and t is the thickness of our wires (45 nm). Table 4.2.4 lists the calculated area doses for three different concentrations of the implanted ions into 45 nm Ag host.

Before performing the ion implantation, we have to know what is the ion energy needed to have most of the implanted Ions stopped in the thickness of the wire. If the ions energy is small, the ions will not be able to penetrate deeply inside the wire. On the other hand, if the ions energy is high, most of the ions will escape to the substrate under the wires. To simulate the ion penetration through the thicknesses of both the wire and the substrate, I used SRIM-2003 software. This program is fed with the type and thickness of each layer involved in the system, and the type of the ion and its energy used in the implantation. In this work, the 45 nm Ag wire represents the first layer, and the silicon oxide (300 nm), which sits underneath the wire, represents the second layer. The results of these simulations indicate that at an ion energy of 70 keV, about 90% of the implanted ions stay in the Ag wires, with the rest going into the silicon oxide layer (see figure 4.5).

All the evaporated samples were divided into four batches. One of them was kept

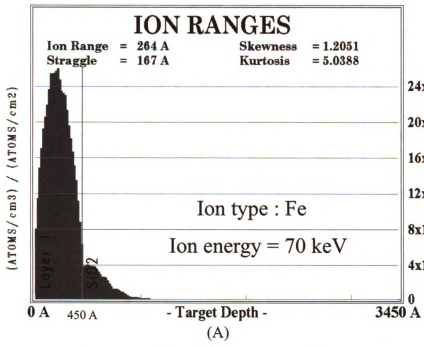

Figure 4.5: The distribution of the implanted Fe Ions in the target. The energy of the Fe Ions is 70keV. Notice that most of the implanted Ions come to rest at the middle of the wire.

pure, and the rest were sent to be ion implanted with 2, 6, and 10 ppm of Fe impurities, respectively. The samples which needed to be ion implanted, were mounted on silicon wafers. Each wafer holds three samples. The samples then were sent to IMPLANT SCIENCE corporation for ion implantation. Unfortunately, the 6 ppm batch did not survive, and here we report data taken on a pure sample and samples with 2 and 10 ppm Fe impurities.

4.3 Measurement methods

4.3.1 Mounting and testing samples at room temperature

Once done with sample fabrication, the sample is then mounted on top of a sample holder as shown in figure (4.6a). The sample holder has a sheet of copper-kapton with

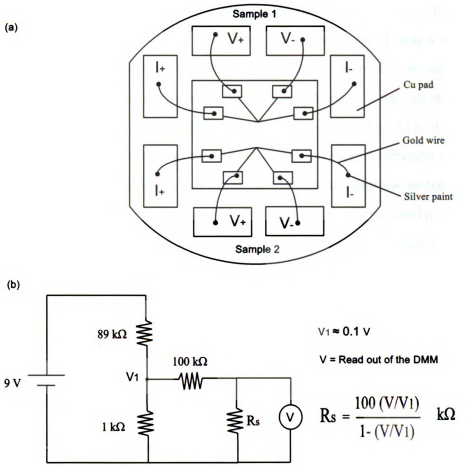

Figure 4.6: Schematic diagram showing a) the sample holder and b) The circuit used to test samples at room temperature.

copper etched away forming 9 distinct pads. The sample is glued to the central pad by silver paint. The remaining 8 pads are used for electrical connections. Gold wires are used to connect the sample pads with the copper pads by silver paint. The copper pads have Cu wires soldered to them. The other ends of the Cu wires are connected to 6-pin Microtech connectors. Each chip has two samples on it, where each sample is connected to 6-pin Microtech connector. While mounting the two samples, I keep them shorted together by shorting the two 6-pin Microtech connectors together and to ground through an external cable. The grounding shorts are important to ensure that

static electricity does not flow through the sample and destroy it, but rather through the ground: the easy path. When I start working on the sample, I wear a wrist strap to short my body to ground. The working area is also shorted to ground through a grounding pad. To attach the gold wires to sample pads, I use the dental pick. Each time I need to use a dental pick, I touch it to the grounding pad to discharge it. Once all the gold wires are connected to both samples, I carefully transfer the sample holder to the probe, which is also grounded to the wall through the switch box.

The probe has a total of 18 wires, 4 of which are used for thermometry, 10 of which for measurements, and the remaining 4 were previously for thermometry, but recently have been modified for other purposes. The 10 measurement leads are divided into 4 sets. The first two sets of twisted pairs are used for voltage measurement, and the remaining two sets of twisted triples are typically used for currents. To reduce the noise in the leads, we use two types of filters; LC-π filters and RC low-pass filters. Each lead has these two filters. The LC-π filter is a commercial filter with 1.75 nF capacitance and a 50 dB roll-off at 100 MHz. This filter sits at the top of the cryostat. The RC low-pass filters are located at the lower part of the probe, with a resistance of 2.2 kΩ and a capacitance of 1 nF.

Once the sample is mounted and wired properly to the probe, it is ready to be tested for electrical continuity at room temperature. To check the electrical continuity, we perform two-terminal measurements with the current passing through the sample less than 1 μA. To get such a small current, we use the circuit shown in figure (4.6b). All samples are made in a way that the outer pads are shorted together by metal guards. So before testing the sample, the guards have to be removed by scratching them carefully with a dental pick, while the sample is grounded. If the sample is electrically continuous and has a reasonable value of resistance, then it is ready to be lowered into the cryostat.

4.3.2 $He^3 - He^4$ Dilution refrigeration

The dilution refrigerator is a powerful tool to reach very low temperatures where many interesting effects in mesoscopic physics take place. To cool the fridge down from room temperature to 77 K, we use liquid nitrogen. Once the core of the fridge reaches 77 K, the liquid nitrogen is replaced by liquid helium which cools the fridge down to 4.2 K. To achieve lower temperatures, one can pump on the helium. The lower the pressure above the liquid helium, the lower the boiling point of the liquid helium. By pumping on the helium, it is possible to reduce the temperature to around 1.2 K. The liquid helium undergoes a superfluid transition at 2.2 K. To reach temperatures below 1.2 K, a different isotope of helium (He^3) is used. This isotope boils at atmospheric pressure at 3.2 K. By pumping on liquid He^3 only, temperatures of 300 mK can be reached. Even lower temperatures can be reached by mixing the He^4 and He^3 in a dilution refrigerator. For the principle of operation of our dilution refrigerator, I refer the reader to reference [51].

Most of my samples were measured in a top-loading $He^3 - He^4$ dilution refrigerator. The base temperature of this refrigerator is around 35 mK. The probe, which is around 0.6 inch in diameter, has a ruthenium thermometer from Oxford Instruments calibrated from 4.2 K down to the base temperature. The thermometer is placed very close to the substrate. Both sample and thermometer are immersed in the $He^3 - He^4$ bath. Conductance bridges were used to record the conductance of the thermometer which is converted to temperature using a Labview program (TemperatureRecord.vi) and calibration table. The mixing chamber is surrounded by a superconducting magnet provided by American Magnetics. The maximum field obtained by this magnet is around 9 Tesla. This magnet provides vertical fields (up and down). Once the current passing through the magnet is known, the magnetic field can be calculated using the relation B(Tesla)=0.11884 I (Amps), where I is the current in Amperes. A mixing chamber heater was used to control the temperature between 35 mK and 4 K.

Measurements above 4.2 K were performed using a pumped He^4 cryostat (1K-Cryostat) which has a base temperature of around 1.3 K. This cryostat has a Germanium thermometer calibrated in the temperature range of 1.4 to 100 K. The conductance of the Germanium resistor was recorded using a Labview program (TemperatureRecord-Ge.vi). This Cryostat is equipped with an American Magnetics magnet with a maximum field of around 9.0 Tesla. The magnetic field generated by this magnet can be calculated from the relation B(Tesla)=0.12066 I (Amps), where I is the current in Amperes.

4.3.3 Sample characterization

To calculate the phase coherence time, τ_ϕ, of a sample, we need to know the dimensions of the sample (L, w, t) and its diffusion constant, D. Table (4.3) lists the Geometrical and electrical characteristics of the measured samples. The resistivity was calculated using Ohm's law, $\rho = Rwt/L$, where R is the sample resistance measured at 1.2 K .

The diffusion constant, D, was determined from the resistivity and the Einstein relation $\rho^{-1} = e^2 D \nu_F$, with the density of states in Ag $\nu_F = 1.03 \times 10^{47} \mathrm{J}^{-1}\mathrm{m}^{-3}$. The uncertainty in D mostly comes from the uncertainty of measuring the width of the wire, w, where $\delta D/D = \sqrt{(\delta R/R)^2 + (\delta L/L)^2 + (\delta w/w)^2 + (\delta t/t)^2}$. The width was measured using SEM with an accuracy of around 10 %. The thickness was measured using AFM with an accuracy of less than 3 %. The mean free path, l_e, was then calculated using the relation $D = v_F l_e/3$, with the Fermi velocity in Ag $v_F = 1.39 \times 10^6$ m/s.

4.3.4 Low field magnetoresistance

Weak localization is a powerful technique used to measure the phase coherence time, τ_ϕ in metallic wires. The change in the resistance $\Delta R(B)$ as a function of applied

Sample	L (μm)	t (nm)	w (nm)	R (Ω)	ρ ($\mu\Omega cm$)	D (cm^2/s)	l_e (nm)	c_{imp} (ppm)
Ag	780	47	130	3307	2.59	146	32	-
AgFe1	780	47	110	3890	2.59	146	32	2
AgFe2	780	47	185	2330	2.59	146	32	10

Table 4.3: Geometrical and electrical characteristics of the measured samples at 1.2 K. L, t, and w are the sample dimensions obtained from the SEM and AFM measurements. R and ρ are the resistance and resistivity of the measured samples. D is the diffusion constant and c_{imp} is the implanted Fe concentration.

magnetic field, B, was measured using the circuit shown in figure (4.7). The applied magnetic field, B, was perpendicular to the film. The size of the typical resistance correction due to weak localization is around 10^{-3} R or less. Since we are interested in measuring the change in the resistance, $\Delta R(B)$, rather than the resistance itself, R, a ratio transformer was used to enhance the lock-in sensitivity. The change in the resistance was measured using a standard ac four-terminal technique with a lock-in amplifier.

The drive signal at the output of the lock-in was taken to two different paths. In the first path the drive signal is fed into the AC input of the sum box, which breaks the ground of the input signal and divides it by 100. The DC input of the sum box was shorted. The output of the sum box goes into a current limiting resistor (Ballast resistor) of 1 MΩ, passes through the sample, and finally goes back to the ground of the lock-in. An NF (LI-75A) preamplifier with a gain of 100 was used to measure the voltage drop across the sample. The input voltage noise of the preamplifier is 1.5 nV/$\sqrt{\text{Hz}}$. The output of the preamplifier was then taken to the A-input of the lock-in. In the second path (see figure 4.7), the drive signal was passed through an isolation transformer to break its ground and then passed through a ratio transformer, whose gain could be adjusted to balance the sample resistance. The output of the ratio transformer was then fed into the B-input of the lock-in. The ratio transformer enables us to subtract the B-input from the A-input of the lock in. By adjusting the

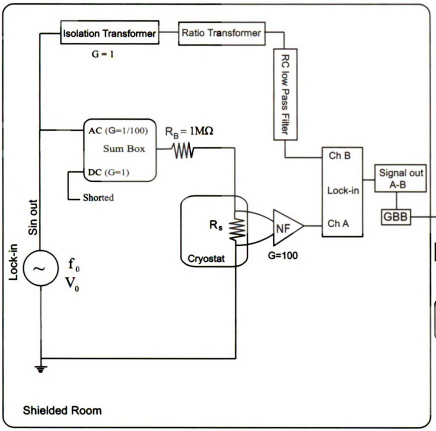

Figure 4.7: Schematic diagram showing the circuit used to measure the change in the resistance due to weak localization. The ground breaking box (GBB) is a differential amplifier which breaks the ground between the lock-in output signal and the shielded room.

ratio transformer gain and setting the lock-in to be in (A-B) mode, the X-channel of the lock-in will read essentially zero. In this case we can view the change of the resistance at much higher sensitivity. A low pass filter was introduced at the output of the ratio transformer to adjust for the phase shift of the signal of interest. The capacitance of this filter was fixed to 0.02 μF and the resistance was varied between 1 and 10 kΩ, to minimize the Y-channel of the lock-in. At C = 0.02 μF and R = 1 kΩ, the low pass filter has a roll-off of about 8 kHz, which is well above the drive frequency (f_0 = 228 Hz). Therefore, the filter does not attenuate the signal much at the output

of the ratio transformer, it mainly shifts its phase. This phase shifter compensates for the phase shift in the measured voltage signal across the sample. The phase shift in the measured signal originates from the capacitance in the circuit which mainly comes from the capacitance of the low-pass filters. Using this set up, the lock-in measures a voltage signal corresponding to the resistance difference between the sample and a reference value set by the ratio transformer. The output of the lock-in can be written as

$$\begin{aligned} V_{lock-in} &= V_A - V_B \\ &= V_0 \left(G_{sum} \frac{R_s}{R_B + R_s} \times G_{NF} - ratio \right) \end{aligned} \tag{4.2}$$

where G_{sum} and G_{NF} are the gains of the sum box and the NF preamplifier, R_s and R_B are the resistances of the sample and the Ballast resistor, and *ratio* is the ratio transformer setting. A typical value of the ratio transformer setting depends on the value of R_s. For example, if $R_s = 2330\ \Omega$, the ratio transformer setting would be $ratio = 0.00233$.

All samples were measured at the same drive frequency ($f_0 = 228$ Hz). The voltage drop across the sample was limited to $eV \leq k_B T$, to avoid heating the electrons in the wires. Measurements of weak localization magnetoresistance below 500 mK, required using longer time constants ($\tau = 3$ sec) to have better signal to noise ratio. Above 500 mK, one can drive harder, and hence use shorter time constants ($\tau = 1$ sec, or 0.3 sec). The output of the lock-in goes through ground breaking boxes, and then is fed into a Keithley 199 model digital multimeter. The output of the Keithley was recorded by Labview program (XYchartrecorder.vi).

The magnetic field was applied perpendicular to the surface of the film (z-direction). Figure (4.8a) shows the circuit used to generate magnetic fields in the z-direction. By connecting the two magnet power supplies (1, 2) in parallel, one can change the cur-

rent direction in the solenoid, hence changing the field direction. To reduce the sweep rate, four shunt resistors were connected in parallel to the power supplies with several configurations. The slowest sweep rate (0.0015 A/s) was achieved by connecting the four shunt resistors in parallel (see figure 4.8b). The current through the superconducting magnet was determined by measuring the voltage across the 0.1 Ω resistor connected in series with the magnet. This 0.1 Ω resistor can handle currents up to 15 A. The voltage across the 0.1 Ω resistor was recorded by Labview program (XY-chartrecorder.vi), where the X-channel measures the voltage across the 0.1 Ω resistor and the Y-channel measures the voltage across the sample. Figure (4.9) shows typical magnetoresistance data for the pure sample taken at 1.6 K.

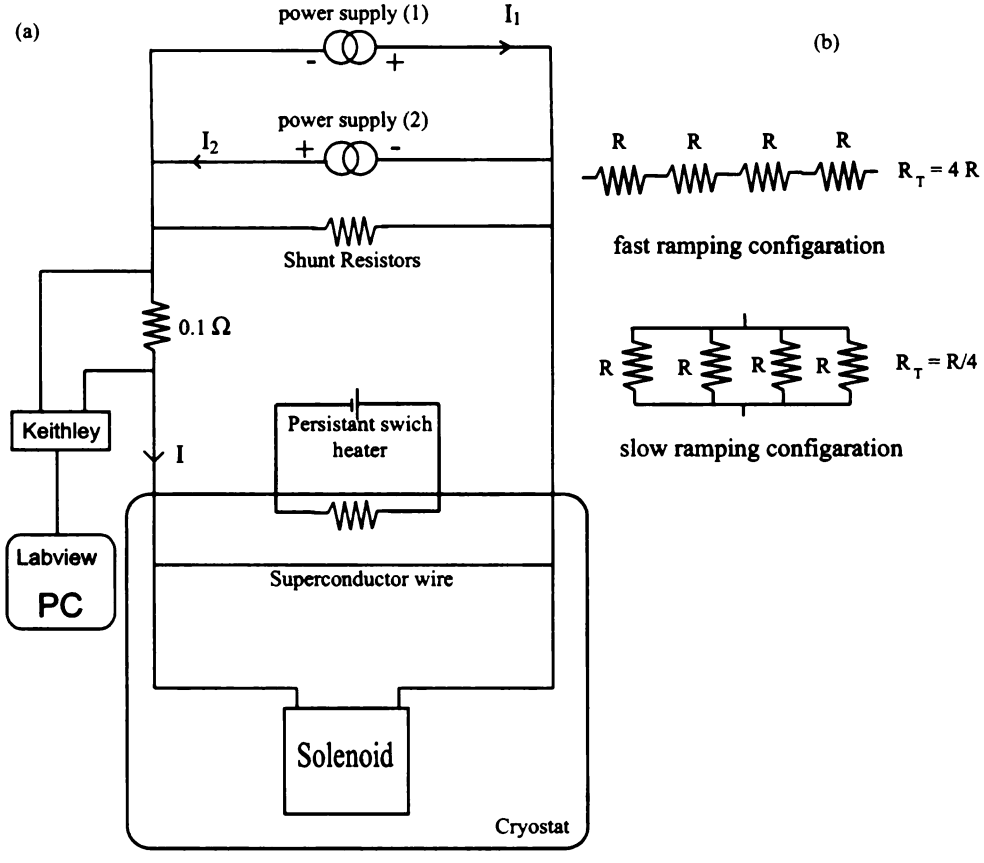

Figure 4.8: (a) Schematic of the circuit used to generate magnetic fields in the z-direction. (b) Two different configurations for connecting the shunt resistors to control the sweep rate. Typical value of the shunt resistor (R) is around 1 mΩ.

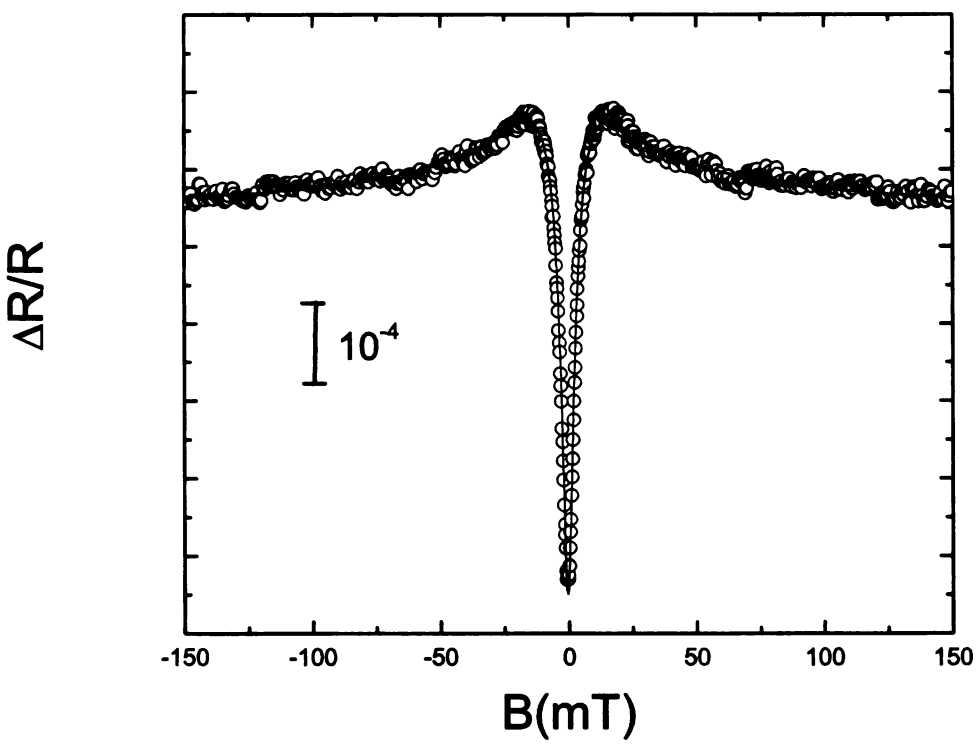

Figure 4.9: Typical magnetoresistance trace of the pure sample taken at 1.6 K. the solid line is the fit to the 1D-weak localization expression

Chapter 5

Results and Discussions I: Phase Coherence

5.1 Introduction

In this Chapter, we first discus how L_ϕ, and hence τ_ϕ, can be determined from magnetoresistance measurements on our quasi-1D Ag wires. Then, we show how the magnetic scattering rate γ_m, due to the implanted Fe impurities, can be extracted from the measured total dephasing rate, γ_ϕ. And finally, we compare our experimental γ_m data with a recent theory [27] of scattering of conduction electrons by dilute magnetic impurities in quasi-1D wires.

5.2 Weak localization and phase coherence

Our wires are quasi-1D in the sense that $w, t \ll L_\phi \ll L$. In our wires, the electron motion is diffusive due to scattering off static disorder. The phase coherence length of the conduction electrons, L_ϕ, depends on both disorder and temperature. All our samples, presumably, have the same amount of disorder, since they were evaporated simultaneously. The disorder dependence shows in the value of the diffusion constant,

D. Here, we investigate the temperature dependence of the phase coherence length, L_ϕ, and hence the phase coherence time, τ_ϕ ($L_\phi = \sqrt{D\tau_\phi}$), in two type of samples; pure and implanted samples. Typically, L_ϕ can be several microns in pure metallic wires at liquid helium temperature [5]. The most reliable way to estimate L_ϕ is to use the method of weak localization magnetoresistance (WLM). The WLM signal is proportional to L_ϕ. Measuring L_ϕ at low T provides information about the scattering mechanisms of the conduction electrons.

In the presence of magnetic field perpendicular to the wires, the weak localization contribution to the resistance will be suppressed, as discussed in Chapter 2. The magnetoresistance is the change in the resistance of the wire due to an applied magnetic field. In pure weakly disordered wires, the field scale of this effect is around 0.03 Tesla, therefore it is called low-field magnetoresistance. However, in samples containing small amount of magnetic impurities, the field scale depends on L_ϕ. We have mentioned in Chapter 4 that the size of the resistance correction due to this effect is around $\Delta R(B)/\mathrm{R} = 10^{-3}$ or less. In the low-field limit, the classical magnetoresistance due to the Lorentz force, $\Delta R(B)/\mathrm{R} \approx (\omega_c\tau)^2$ [13], where $\omega_c = eB/m$ is the cyclotron frequency, is negligibly small. In our wires where $l_e \approx 32$ nm, in a magnetic field of 1 T this classical magnetoresistance is of the order of 10^{-5} R, which is typically two order of magnitudes smaller than the weak-localization magnetoresistance. By scanning the magnetic field between -0.03 Tesla to 0.03 Tesla, one can measure the resistance change due to electron weak localization, hence indirectly measure L_ϕ.

5.2.1 Total dephasing rate : pure samples

In this work, two pure samples were measured in two different cryostats. The first pure sample was measured in an Oxford dilution refrigerator between 40 mK and 4.0 K. I will call this sample (puresample1). This sample was measured directly after the evaporation. The diffusion constant of this sample was 146 cm^2/s. Unfortunately,

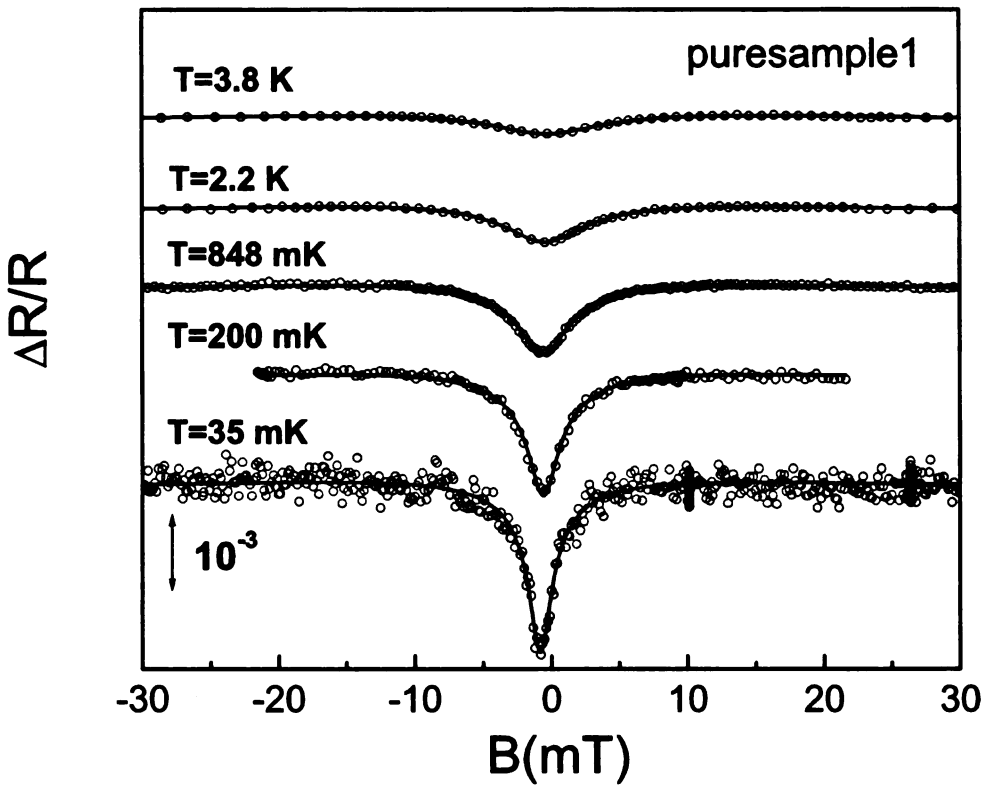

Figure 5.1: Magnetoresistance data of puresample1 and fits to equation (2.8). This sample was measured in the dilution refrigerator. The Ag wires were made from source materials of nominal purity 6N (99.9999%). The geometrical and electrical characteristics of this sample is the same as the Ag sample given in table (4.3). The spin-orbit length extracted from the MR fits was 0.76 μm. The B offset is due to trapped flux in the superconducting magnet.

this sample did not survive to be measured again in the high temperature cryostat (1K-cryostat). Therefore, we had to measure another pure sample to acquire data above 4.0 K. The second pure sample was measured using a pumped He^4 cryostat (1K-cryostat) between 1.3 K and 18.0 K. I will call the second sample (puresample2). This sample was measured five months after the evaporation. The diffusion constant of this sample was 120 cm^2/s. The lower value of the diffusion constant of this sample could be due to some oxidation of the silver wire.

Figures (5.1) and (5.2) show magnetoristance data and fits to equation (2.8). Magnetoristance data for each sample were fit using the following procedure [52]. We

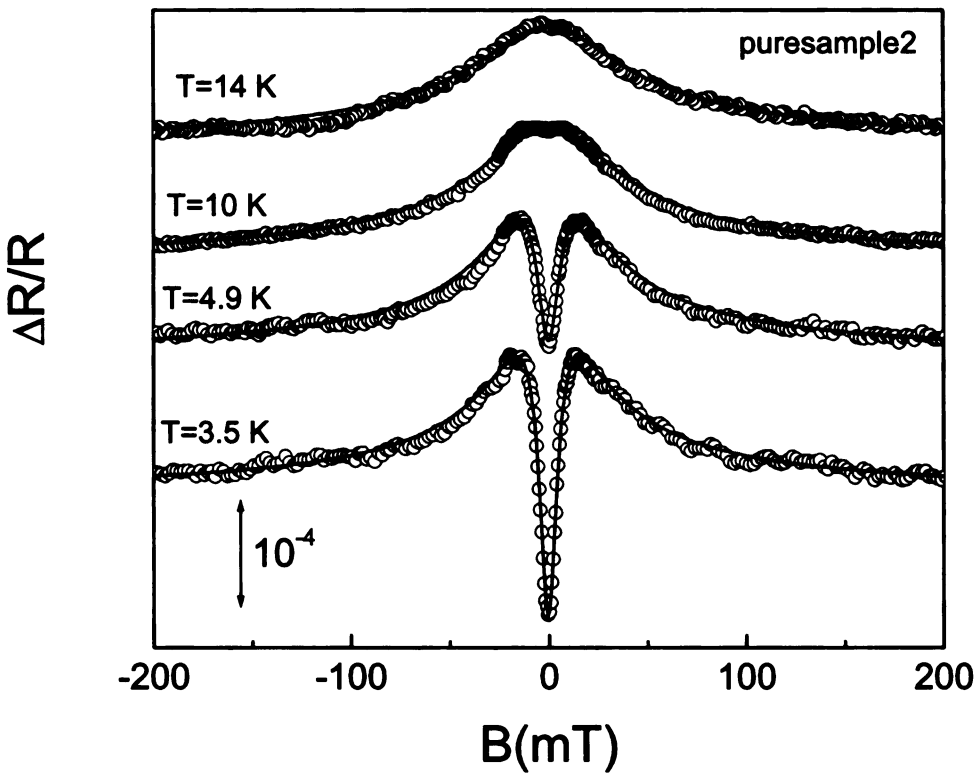

Figure 5.2: Magnetoresistance data of puresample2 and fits to equation (2.8). This sample was measured in the 1K-cryostat. The geometrical and electrical characteristics of this sample are: $L = 780$ μm, $w = 137$ nm, $t = 47$ nm, $D = 120$ cm^2/s, $L_{so} = 0.72$ μm, and $R = 3824$ kΩ. The Ag wires were made from source materials of nominal purity 6N (99.9999%).

have mentioned in Chapter 2 that what determines the MR lineshape (peak or dip around the zero field) is the strength of the spin-orbit coupling. Silver is considered to have moderate spin-orbit scattering [53] ($\tau_{so} \approx 40$ ps for all of our samples). At low T, where $\tau_\phi \gg \tau_{so}$, the MR is positive (dip). At higher temperatures, where $\tau_\phi < \tau_{so}$, the MR starts out positive but then turns around at a field scale $B \approx$ 20 mT (see figure 5.2). Data at several temperatures in this higher temperature range (which was different for each sample) were first fit with three free parameters: $L_\phi = \sqrt{D\tau_\phi}$, where D is the diffusion constant, $L_{so} = \sqrt{D\tau_{so}}$, and the sample width, w. Furthermore, the MR data are known only up to an additive constant which was adjusted to fit each MR curve. For each sample, these fits gave consistent values of

L_{so} and w over a broad temperature range. We then fixed those values of L_{so} and w, and fit the MR curves for all temperatures with L_ϕ as the only free parameter. The difference between the width measured from the scanning electron microscope (SEM) and the best fit value of w, was found to be always less than 20%. To calculate the diffusion constant, D, we used the width value measured from the SEM. Using the value of D obtained from the resistance and sample dimensions, we finally obtain τ_ϕ as a function of temperature for each sample. Figures (5.1) and (5.2) also show that the size of the weak-localization signal increases with decreasing temperature due to the progressive freezing of the inelastic scattering events, specifically e-ph scattering events.

Figure (5.3) shows the total dephasing rate, γ_ϕ, as a function of temperature for both puresample1 and puresample2. From now on, I will refer to this figure shortly as puresample or Ag sample, which will be used in the comparison with the implanted samples. Furthermore, the parameters of puresample1 given in table (4.3) will be used in future calculations. In pure metallic wires, as discussed in chapter 2, the total dephasing rate takes the form, $\gamma_\phi(T) = AT^{2/3} + BT^3$ [1, 11], where the first term describes the electron-electron scattering rate, dominating at lower T, and the second term describes the electron-phonon scattering rate, dominating at higher T. The e-ph scattering rate (BT^3) corresponds to the clean limit ($q_T l_e \gg 1$), where q_T is the wave vector of a typical thermal phonon at temperature T, and l_e is the elastic mean free path of conduction electrons. The clean limit approximation is usually valid at high temperatures. The expected values of the prefactors A_{thy} and B_{thy} are 0.32 $\text{ns}^{-1}\text{K}^{-2/3}$ and 0.002 $\text{ns}^{-1}\text{K}^{-3}$, respectively. The solid line in the figure is the fit of $\gamma_\phi(T)$ data to this functional form. It can be seen from the figure that the e-e interactions dominate the scattering below 1 K, and the e-ph interactions dominate at temperatures above 1 K. The inset shows the output of the prefactors A_{exp} and B_{exp} extracted from the least-square fit. While the prefactor $A_{exp} \approx 0.36$ $\text{ns}^{-1}\text{K}^{-2/3}$ is in good agreement with

the expected value, $A_{thy} \approx 0.32$ ns^{-1}K$^{-2/3}$ [52], the prefactor $B_{exp} \approx 0.026$ ns^{-1}K^{-3} is higher than the predicted value, $B_{thy} \approx 0.002$ ns^{-1}K^{-3} by roughly one order of magnitude. As discussed in Chapter 2, the relatively big difference between B_{thy} and B_{exp}, indicates that the e-ph scattering is not limited to one regime (clean limit) over the temperature range of 40 mK – 18 K, instead it crosses over between them (see the discussion of e-ph interactions given in Chapter 2). The γ_ϕ data, as seen from the figure, follow the model above 200 mK, with a modest amount of saturation at lower temperature. This, however, may possibly be attributed to the presence of extremely dilute magnetic impurities with low Kondo temperatures, T_K, in the source material, Ag(6N) [5].

At low temperatures, the scattering of conduction electrons by magnetic impurities plays a major rule in electron dephasing. In the presence of extremely dilute magnetic impurities ($c_{imp} \ll 1$ ppm) with low T_K, the total dephasing rate takes the form, $\gamma_\phi(T) = AT^{2/3} + BT^3 + \gamma_{sf}(T)$ [5], where γ_{sf} is the spin-flip scattering rate of conduction electrons. Above T_K, the spin-flip scattering rate can be described well by the Suhl-Nagaoka (SN) expression [17, 21] (see equation 1.15). Looking carefully at this expression (SN expression), one can see that the spin-flip scattering rate, γ_{sf}, increases when T approaches T_K from above. On the other hand, the e-e scattering rate, $\gamma_{ee}(T)$, decreases with decreasing temperature. The competition between these two rates creates a nearly constant dephasing rate above T_K. This might be responsible for the observed saturation seen in the pure samples below 200 mK.

To test this hypothesis and to have an estimate of the concentration of the proposed magnetic impurities in our pure wires, we refitted the total dephasing rate, $\gamma_\phi(T)$, taking into account the additional contribution of spin-flip scattering interaction due to extremely dilute low T_K magnetic impurities, as well as the two major sources of electron dephasing at low T, e-e and e-ph interactions. Assuming the existence of Mn magnetic impurities, for example, with s=5/2 and T_K = 40 mK [5],

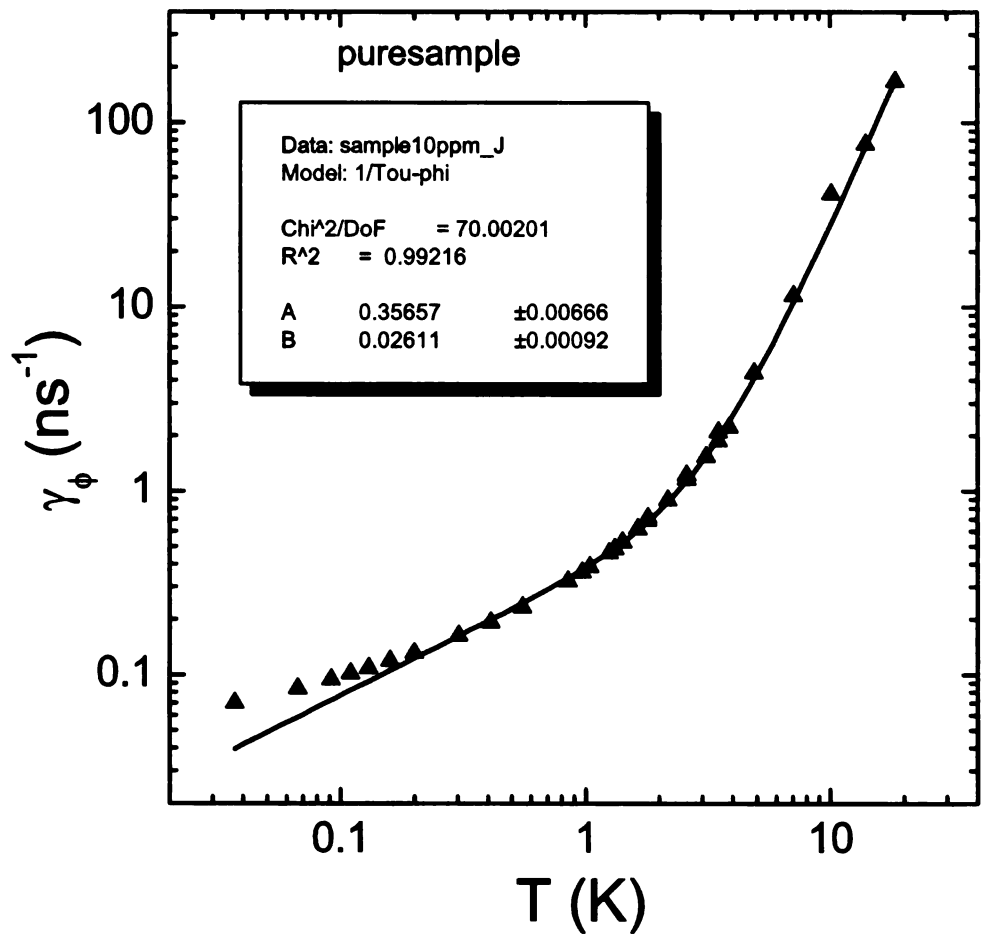

Figure 5.3: The total dephasing rate, γ_ϕ, as a function of temperature for both puresample1 and puresample2. The solid line is the fit of γ_ϕ to the form $\gamma_\phi(T) = AT^{2/3} + BT^3$, assuming that our wires are free of magnetic impurities. The inset is the output of the least square fit of the two prefactors, A and B.

and using the Suhl-Nagaoka expression for $\gamma_{sf}(T)$ and leaving the concentration c as a free parameter, the fit is improved below 200 mK, as shown in figure (5.4). The parameter $c \approx 0.01$ ppm in the inset is the concentration of the Mn magnetic impurities, extracted form the fit, expressed in units of ppm. This concentration is about 100 times smaller than the nominal total impurity concentrations of any silver source available in the market. Such a small concentration is undetectable by any means other than measuring the phase coherence time in films [5]. A similar fit was obtained by assuming the presence of Cr magnetic impurities with $s = 2$ and $T_K = 10$ mK. The

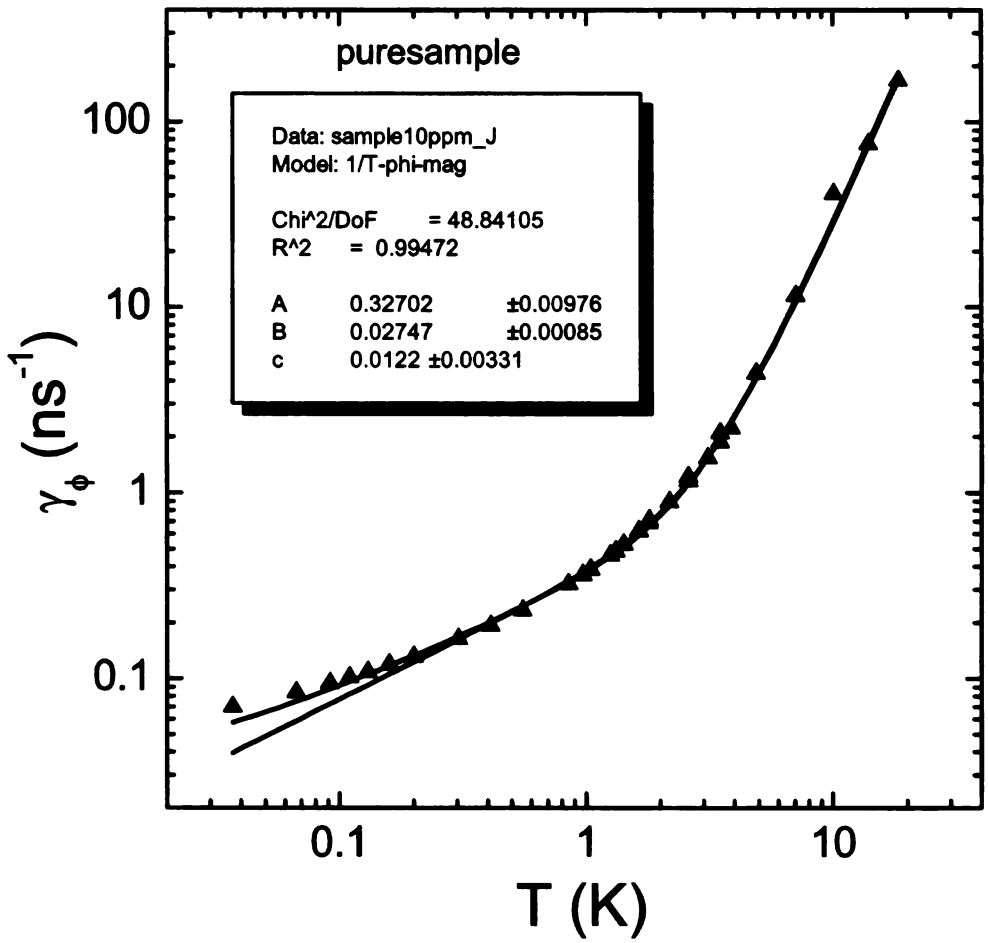

Figure 5.4: The total dephasing rate, γ_ϕ, as a function of temperature for both puresample1 and puresample2. The lower solid line is the fit of γ_ϕ to the form $\gamma_\phi(T) = AT^{2/3} + BT^3$, assuming that our wires are free of magnetic impurities. The upper solid line is the fit of γ_ϕ to the form $\gamma_\phi(T) = AT^{2/3} + BT^3 + \gamma_{sf}(T)$, where γ_{sf} is the spin-flip scattering rate of conduction electrons due to extremely dilute magnetic impurities, ($c_{imp} \ll 1$ ppm). The parameter $c \approx 0.01$ ppm in the inset is the concentration of the Mn magnetic impurities, extracted form the fit, expressed in units of ppm. Similar fit was obtained by assuming the presence of Cr magnetic impurities with $s = 2$ and $T_K = 10$ mK. Notice how the fit is improved with the addition of a very small number of magnetic impurities.

issue of electron dephasing by extremely dilute magnetic impurities was discussed in detail in reference [5], in the context of the debate over zero-temperature dephasing in disordered metals [4].

In summary, the total dephasing rate of our pure wires was measured in the temperature range of 40 mK - 18 K. In the next sections, this total dephasing rate of the pure wires will be subtracted from the measured total dephasing rate of the implanted samples, to extract the magnetic scattering rate (spin-flip scattering rate) due to the implanted Fe magnetic impurities.

5.2.2 Total dephasing rate : 2 ppm sample

In the implanted samples, the phase coherence length, L_ϕ, must be shorter due to the scattering of conduction electrons by Fe magnetic impurities. How short L_ϕ is depends on the concentration of the magnetic impurities. As discussed in Chapter 4, 2 ppm of Fe magnetic impurities were introduced into the thickness of the wires by ion-implantation. The area dose equivalent to this concentration was 0.53×10^{12} cm^{-2}. This sample was measured only in the dilution refrigerator from 37 mK - 4 K. Figure (5.5) shows the MR curves of this sample taken at different temperatures.

Figure (5.6) shows the total dephasing rate, γ_ϕ, as a function of temperature for the 2 ppm sample. Notice that γ_ϕ decreases with decreasing temperature. According to theory, the total dephasing rate must vanish at zero temperature, where all inelastic scattering events freeze out. At the lowest accessible temperature (35 mK in this work), $\gamma_\phi \approx 0.2$ ns^{-1} for this sample (see figure 5.6). As will be discussed later in this Chapter, the Kondo temperature of our system (AgFe) is around 5 K [52], therefore the γ_ϕ data of this sample (2 ppm) falls below T_K. Far below T_K, Fermi liquid theory predicts a T^2 dependence of γ_ϕ [25]. This, however, has never observed experimentally. The phase coherence length, L_ϕ, of this sample at the base temperature was around 9.1 μm, which is shorter than that of the pure sample ($L_\phi = 14.6$ μm). This decrease

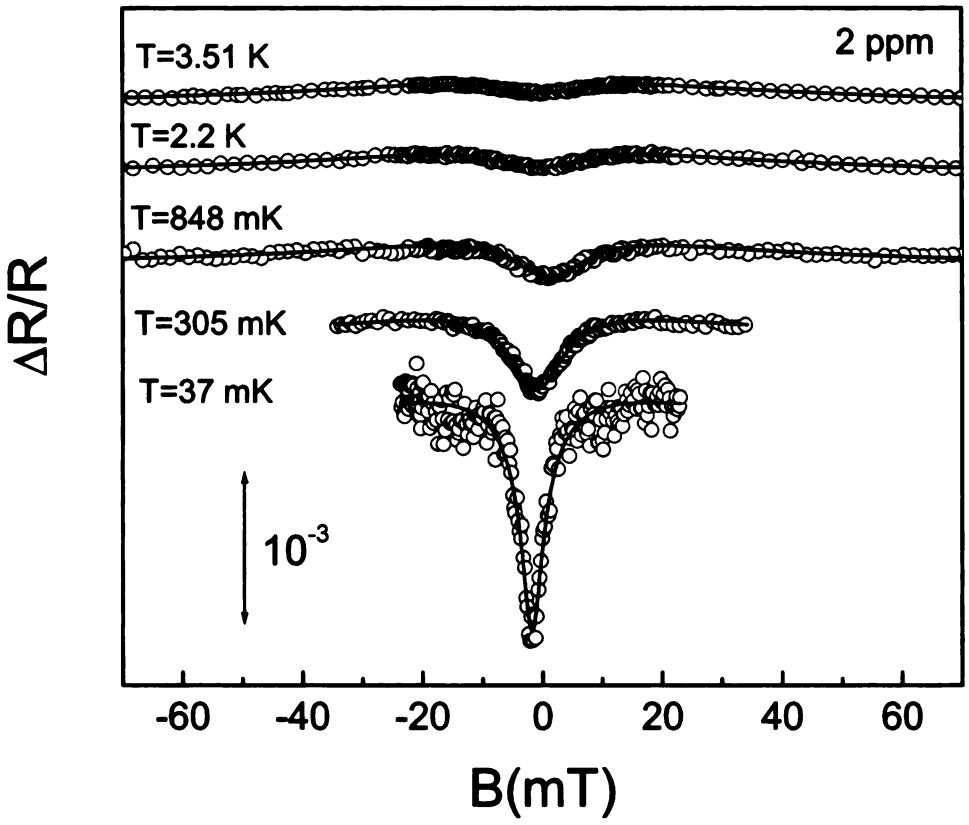

Figure 5.5: Magnetoresistance data of the 2 ppm sample and fits to equation (2.8). This sample was measured in the dilution refrigerator between 37 mK and 4 K. The geometrical and electrical characteristics of this sample are listed in table (4.3) under the name "AgFe1". The spin-orbit length extracted from the fit was 0.86 μm. The B offset is due to trapped flux in the superconducting magnet.

in L_ϕ is due to the addition of 2 ppm of Fe magnetic impurities.

5.2.3 Total dephasing rate : 10 ppm sample

This sample was ion-implanted with 10 ppm Fe magnetic impurities. The area dose equivalent to this concentration was 2.66×10^{12} cm^{-2}. The sample was first measured in the dilution refrigerator between 35 mK and 4 K. The magnetoresistance data of this sample are shown in figure (5.7). The geometrical and electrical characteristics of this sample are given in table (4.3), under the name "AgFe2". The phase coherence length, L_ϕ, of this sample at the base temperature was around 4.1 μm, which is

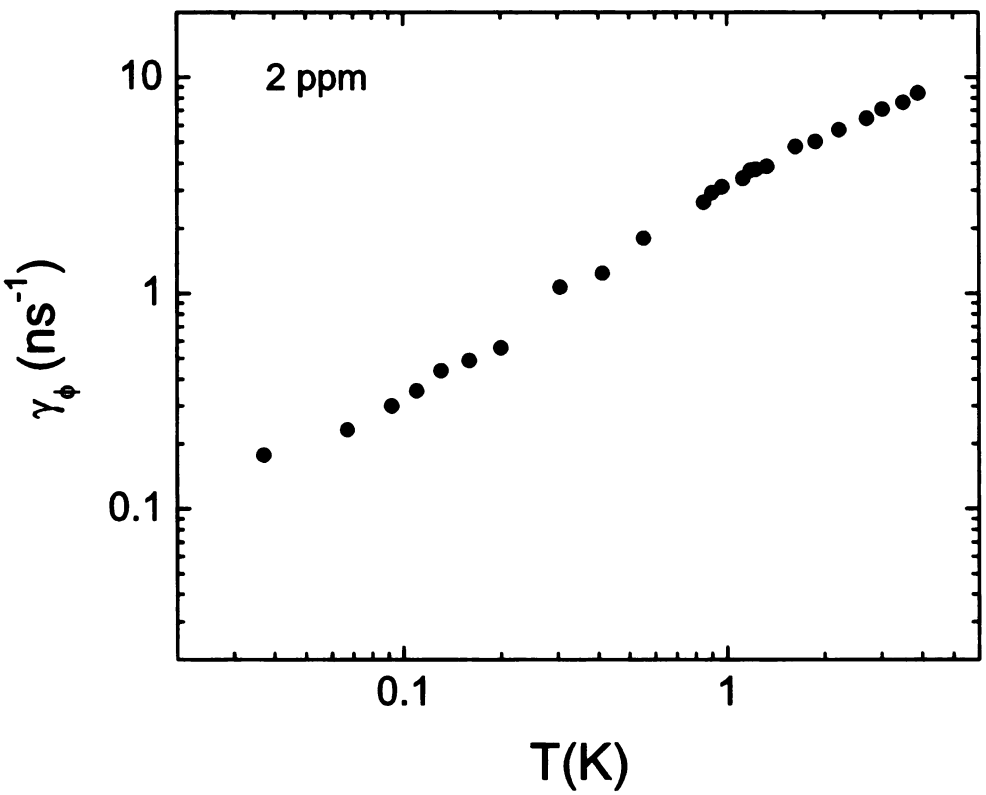

Figure 5.6: The total dephasing rate, γ_ϕ, as a function of temperature for the 2 ppm sample in the temperature range of 37 mK - 4 K. Notice that γ_ϕ continue to decrease and vary lineally with temperature over almost on decade. The fit of data will be discussed later in this chapter.

shorter than both the pure and the 2 ppm samples. This decrease in L_ϕ again is due to the addition of 10 ppm of Fe magnetic impurities.

To acquire data above 4 K, the sample was then measured again in the high temperature cryostat (1K-cryostat). The magnetoresistance data of this sample, above 4 K, are shown in figure (5.8). Unfortunately, the sample resistance went up from 2330 kΩ to 3879 kΩ. This may have happened during the mounting process. Even one single bad spot created on the wire can take the resistance up by this magnitude. The effect of this jump in the resistance of the wire reduced the measured diffusion constant of the sample from 146 cm^2/s to 87 cm^2/s. Nevertheless, after fitting the MR data carefully in this high temperature regime, above 4 K, we found that the γ_ϕ

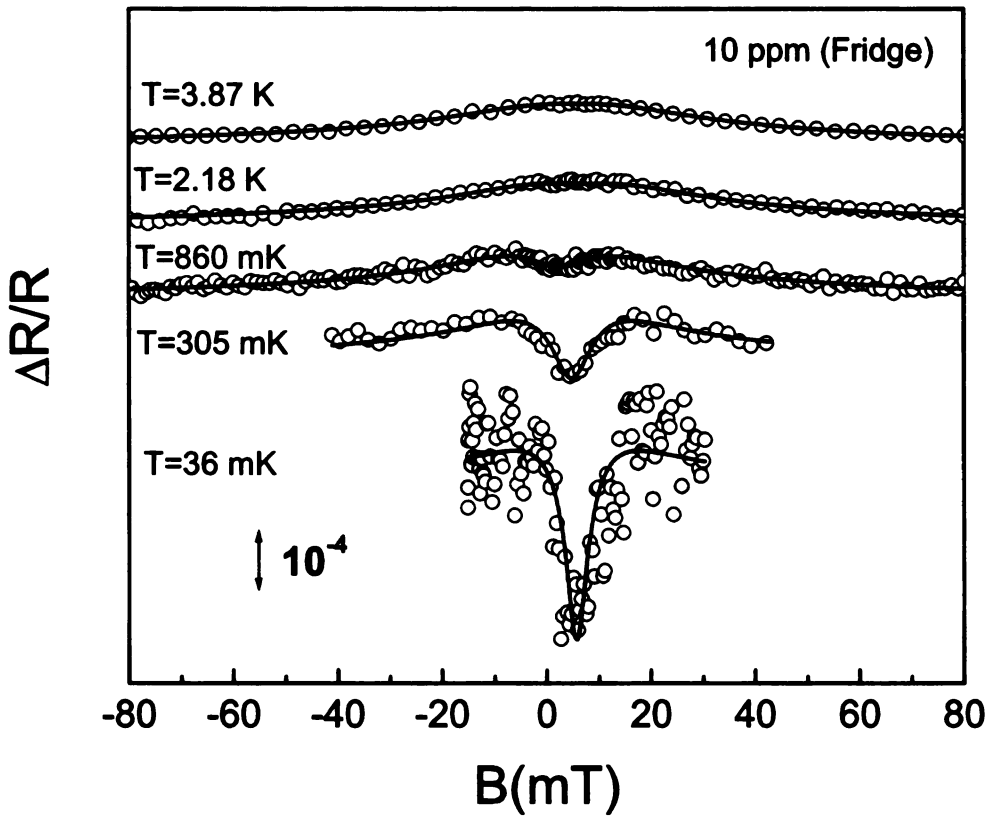

Figure 5.7: Magnetoresistance data of 10 ppm sample and fits to equation (2.8). This sample was measured in the dilution refrigerator. The geometrical and electrical characteristics of this sample are listed in table (4.3) under the name "AgFe2". The spin-orbit length extracted from the MR fits was 0.72 μm. The MR data at 36 mK are noisy due to the fact that the voltage across the wire was limited to $eV \lesssim k_B T$, to avoid heating the electrons in the wire. The B offset is due to trapped flux in the superconducting magnet.

data, extracted from fitting the MR data taken in the 1K-cryostat match well with the γ_ϕ, extracted from fitting the MR data taken in the dilution refrigerator, below 4 K, (see figure 5.9).

The total dephasing rate of this sample, as shown in figure (5.9), decreases as T approaches T_K from above, has a plateau around the Kondo temperature ($T_K \approx 5$ K), and decreases linearly with T below T_K. Again the T^2 behavior of γ_ϕ, predicted by Fermi liquid theory [25], was not reached down to the lowest accessible temperature (35 mK).

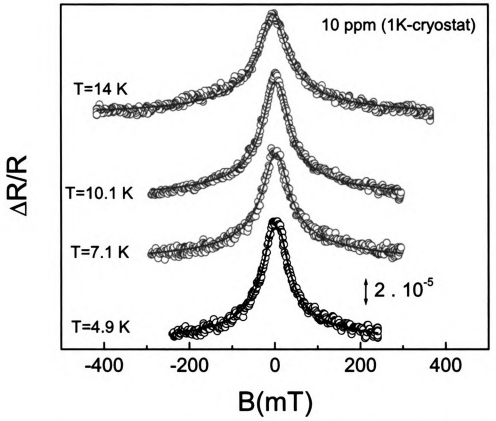

Figure 5.8: Magnetoresistance data of the 10 ppm sample and fits to equation (2.8). This sample was measured in the 1K-cryostat. The geometrical characteristics of this sample are the same as the AgFe2 sample given in table (4.3). The electrical characteristics of this sample are: $R = 3879$ kΩ, $D = 87$ cm^2/s. The spin-orbit length extracted from the MR fits was 0.49 μm. The B offset is due to trapped flux in the superconducting magnet.

5.3 Extracting the magnetic scattering rate from the total dephasing rate

In the presence of a small amount of magnetic impurities, there is an additional contribution to $\gamma_\phi(T)$ from the scattering of the conduction electrons by the magnetic impurities, $\gamma_m(T)$. As discussed in Chapter 1, the temperature dependence of the magnetic scattering rate, $\gamma_m(T)$, is usually obtained by subtraction of the total dephasing rate of the pure sample from the total dephasing rate of the implanted sample

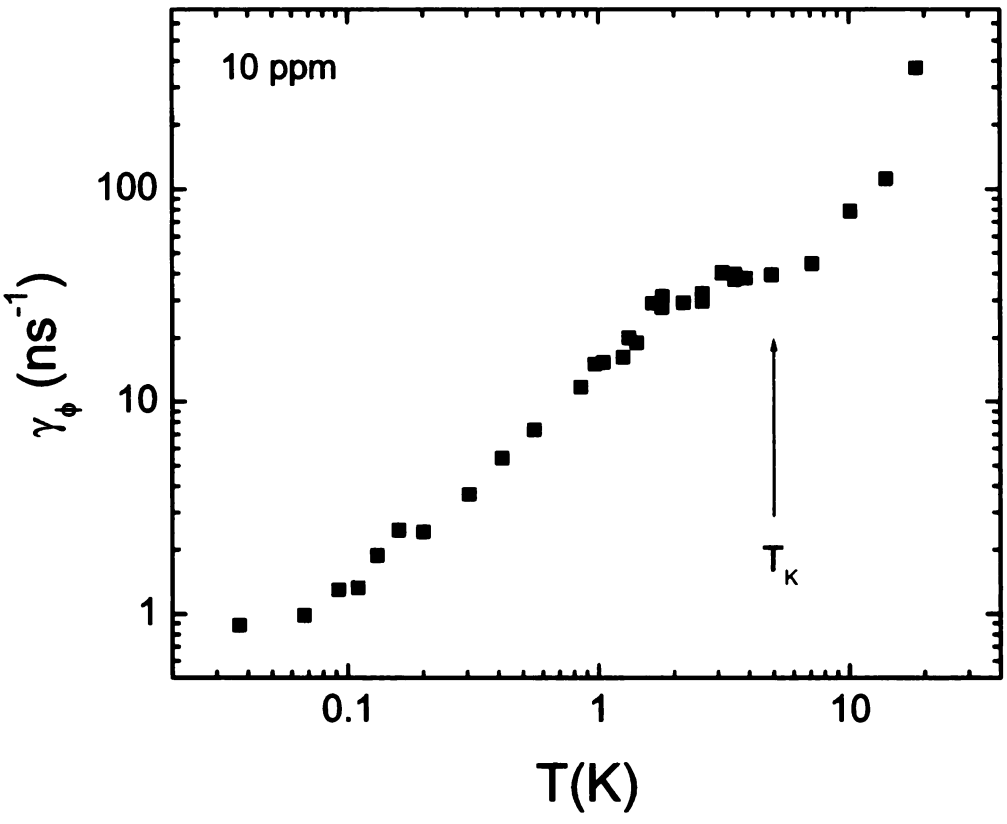

Figure 5.9: The total dephasing rate, γ_ϕ, as a function of temperature for the 10 ppm sample in the temperature range of 36 mK - 18 K. Notice that γ_ϕ decreases with decreasing temperature, has a plaeau around T_K, and continues to decrease linearly with temperature over almost one decade below T_K. The fit of data will be discussed later in this chapter.

(see figure 1.4). The method of addition (subtraction) of the total dephasing rates was discussed in detail in Chapter 3, where we showed that there are two ways of adding them (see equations 3.45 and 3.46), depending on the ratio γ_m/γ_K, where γ_K is the Korringa scattering rate [43]. If $\gamma_m < \gamma_K$, equation (3.45) should be used for adding the dephasing rates. On the other hand, if $\gamma_m > \gamma_K$, then equation (3.46) should be used instead.

Below the Kondo temperature, T_K, the Korringa rate saturates and the ratio reads $\gamma_m/\gamma_K = n_s/\nu_F k_B T_K$, where n_s is the concentration of magnetic impurities and ν_F is the total DOS at the Fermi level. For the 2 ppm sample, and assuming

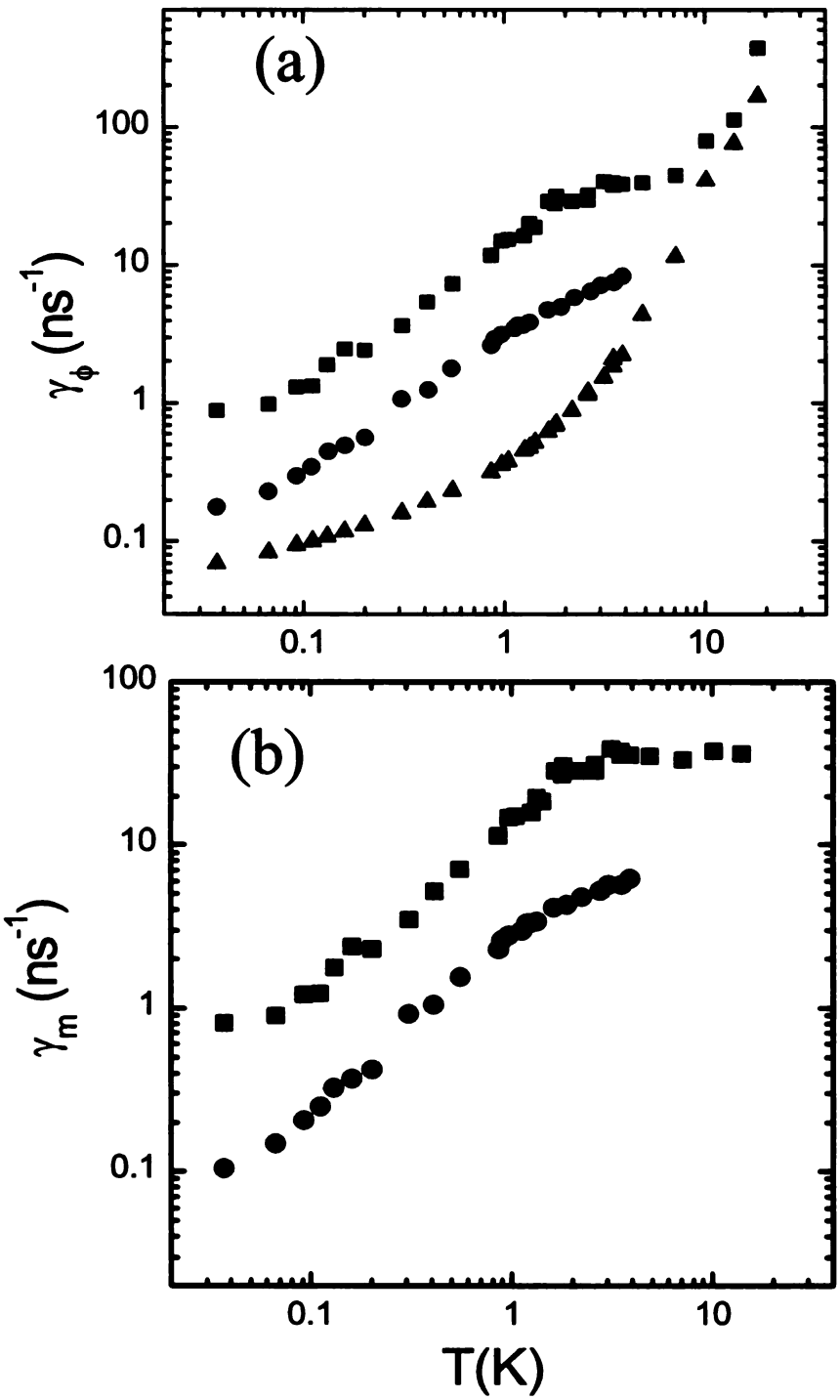

Figure 5.10: a) Total dephasing rate vs. temperature for a pure Ag sample (▲), and for samples with implanted Fe concentrations of 2 ppm (•) and 10 ppm (■). b) Magnetic scattering rate vs. temperature for samples with implanted Fe concentrations of 2 ppm (•) and 10 ppm (■), after subtracting the total dephasing rate of the pure sample.

$T_K \approx 5$ K (to be shown later), $\gamma_m/\gamma_K = 0.02 \ll 1$; hence we should use equation (3.45) to extract $\gamma_m(T)$ from $\gamma_\phi(T)$. Similarly for the 10 ppm sample, the ratio reads $\gamma_m/\gamma_K = 0.2 < 1$; hence equation (3.45) should be used again to extract $\gamma_m(T)$ from $\gamma_\phi(T)$. Figure (5.10b) shows the magnetic scattering rate for both 2 ppm and 10 ppm samples after subtracting the total dephasing rate of the pure sample.

5.4 Fitting the magnetic scattering rate to theory of Micklitz *et al.*

In this section, we fit our magnetic scattering data to the theory of Micklitz *et al.* [27]. This theory, as mentioned earlier, uses the numerical renormalization group (NRG) method to calculate the complete temperature dependence of the magnetic scattering rate of the conduction electrons from dilute magnetic impurities, in weakly disordered metals. This theory was originally developed to describe the effect of a small concentration, n_s, of spin 1/2 magnetic impurities on the dephasing rate from $T \gg T_K$ all the way down to $T \ll T_K$. However, in our wires, n_s is small but $s = 2$ instead. As predicted by this theory, the magnetic scattering rate, $\gamma_m(T)$, due to very dilute magnetic impurities is a universal function, $\gamma_m(T) \propto n_s f(T/T_K)$, and depends only on two parameters, n_s and T_K. This theory has maximum predictive power if both the concentration , n_s, and the Kondo temperature, T_K, are known. In this work, only the concentration, n_s, is known from the ion-implantation process. Therefore, T_K, will be a free parameter in the following fit. The following chapter will discuss our attempt to obtain an independent estimate of T_K.

The criterion $\gamma_m/\gamma_K \ll 1$ is a necessary condition for the theoretical approach of Micklitz *et al.* [27] in their NRG calculations of γ_m. In this work, our γ_m data are within this limit, therefore we used equation (3.45) to add the dephasing rates due to all mechanisms (Matthiessen's rule). Figure (5.11) shows γ_m for the 2 ppm

and 10 ppm samples obtained from the γ_ϕ data using the equation ($\gamma_m = \gamma_\phi - \gamma_{in}$), with γ_{in} obtained from the data on the nominally pure sample (figure 5.3). The 2 ppm data is multiplied by 5 to scale it with the 10 ppm sample. The two data sets are consistent with each other, indicating that our measurements of γ_ϕ for both samples were accurate. This figure summarizes our work for the phase coherence in the implanted samples [52].

The dotted line in the figure is the Suhl-Nagaoka (SN) approximation for s=1/2 magnetic impurities. As seen from the figure, the SN approximation describes well our γ_m data for $T > T_K$. On the other hand, for $T < T_K$, the SN approximation does not come close to reproducing the temperature dependence of γ_m, consistent what was observed in reference [54].

The solid line in figure (5.11) shows a fit of the NRG calculation from [27] to our data at temperatures above 0.4 K only. Our fit was restricted to $T > 0.4$ K, because including data below 0.4 K makes the overall fit distorted. Fitting to the 2 ppm (10 ppm) data alone gives $T_K = 4.8$ K (5.4 K). The Kondo temperature here represents the temperature at which the magnetic scattering peaks. This peak is broad around the Kondo temperature, as predicted by theory. The NRG theory of Micklitz *et al.* [27] fits the data reasonably well over the temperature range $T/T_K = 0.1 - 2$ [52]. This fit is much better than that obtained using the SN approximation for the decade below T_K. For $T/T_K < 0.1$, the NRG theory of Micklitz deviates strongly from the γ_m data. Above T_K, γ_m data is almost constant. Below T_K, γ_m varies linearly in T. Below 0.1 T_K, the temperature dependence of γ_m is much weaker than that given by theory, and it certainly doesn't approach the T^2 behavior predicted by Fermi liquid theory [25].

According to theory of Micklitz, the maximum value of γ_m, occurring at $T = T_K$, is equal to $0.23 \times 4n_s/(\pi\hbar\nu_F)$. For the 10 ppm sample, the predicted maximum of γ_m is $\gamma_m^{max} = 16$ ns^{-1}, whereas the data in figure (5.11) show a maximum value about

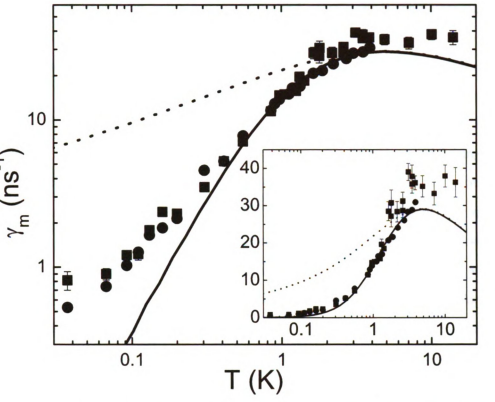

Figure 5.11: Inelastic scattering rate due to magnetic impurities for the 2 ppm (•) and 10 ppm (■) samples. Data for the 2 ppm sample are multiplied by 5. The solid line is the theoretical calculation of Micklitz *et al.* [27] fit to the data for $T > 0.4$ K. The dotted line is the Suhl-Nagaoka approximation for s=1/2. Inset: Same plot with a linear vertical scale. Uncertainties are larger for the 10 ppm sample due to smaller signal-to-noise in the measurements.

twice as large (≈ 34 ns^{-1}). This factor 2 difference between theory and experiment could be due to the inadequacy of the spin-1/2 theory of Micklitz *et al.* [27] to account for the large spin (s=2) of Fe impurities in Ag. On the other hand, previous measurements of the magnetic scattering rate, γ_m, in Ag samples implanted with Mn impurities [5], with s=5/2, were consistent with the theoretical estimate. Due to the low Kondo temperature of Mn in Ag ($T_K \approx 40$ mK), those data were analyzed with the SN approximation, which is in close agreement with the theory of [27] for $T > T_K$. We conclude that the inelastic scattering cross section of Fe in Ag is roughly twice that of Mn in Ag.

The most serious discrepancy between theory and experiment is the flattening of $\gamma_m(T)$ for $T/T_K < 0.1$, shown in figure (5.11). The NRG calculations of Micklitz were based on the assumption that for spin 1/2 magnetic impurities and at temperatures far below T_K, the magnetic impurities are totally screened by conduction electrons. This state is called compensated state, with ($n = 2S$) [18], where n is the number of channels and S is the spin of magnetic impurity; hence $n = 1$ in this model (single-channel Kondo model). For Fe, which has 6 electrons in the 3d orbital, the ground state according to Hund's rule has a spin S=2, so there will only be perfect spin compensation ($n = 2S$) if the number of channels is 4 (n-channel Kondo model) [18]. Sacramento and Schlottmann showed that a multi-channel Kondo model with S=2 and n=4 gave a good fit to data for several equilibrium quantities in the Ag:Fe and Cu:Fe systems [29]. A calculation of the phase decoherence rate in that model might resolve the discrepancy between theory and experiment shown in figure (5.11). The issue of screening for Fe in Ag is unclear. The Fe spin (S=2) is coupled to the conduction electrons through five channels corresponding to the d-orbitals of Fe, so the S=2 Fe spin should be overscreened. In reality, however, the different channels have different coupling constants, and the impurity spin and orbital degeneracies are broken by crystal fields and spin-orbit scattering. A recent calculation of the inelastic scattering cross section for the the case where screening is incomplete (with S=1 and n=1) shows that such a model can not fit our data for $0.1 < T/T_K < 1$ [55]. The multi-channel Kondo model of Fe magnetic impurities in Ag has been recently investigated in [56] for both underscreened ($n < 2S$) and overscreened ($n > 2S$). Those authors conclude that neither underscreened nor overscreened models can fit the low-temperature inelastic scattering rate. Pedro Schlottmann believes that the flatting of γ_m in our samples may be a finite-size effect [57]. As the temperature is decreased, the effective dimensionality of the Ag wire seen by the Kondo impurity may cross over from 3D to 2D or even 1D.

Chapter 6

Results and Discussions II: High Field Magnetoresistance

6.1 Introduction

In this chapter we first show our data of the resistivity as a function of temperature for both pure and implanted samples . Then we discuss the high field magnetoresistance of our samples. Specifically, we show how the Kondo temperature, T_K, can be determined independently from analyzing the high field magnetoresistance data in the context of Numerical Renormalization Group (NRG) calculations of reference [58].

6.2 Resistivity vs temperature

The electrical resistivity of a pure metal is dominated at high temperatures by collisions of the conduction electrons with phonons. On the other hand, at lower temperatures, the electrical resistivity is dominated by collisions of the conduction electrons by static disorder (static impurities, film boundaries, ...). Figure (6.1) shows the resistivity as a function of temperature of puresample2 measured between 1.3 K-32 K.

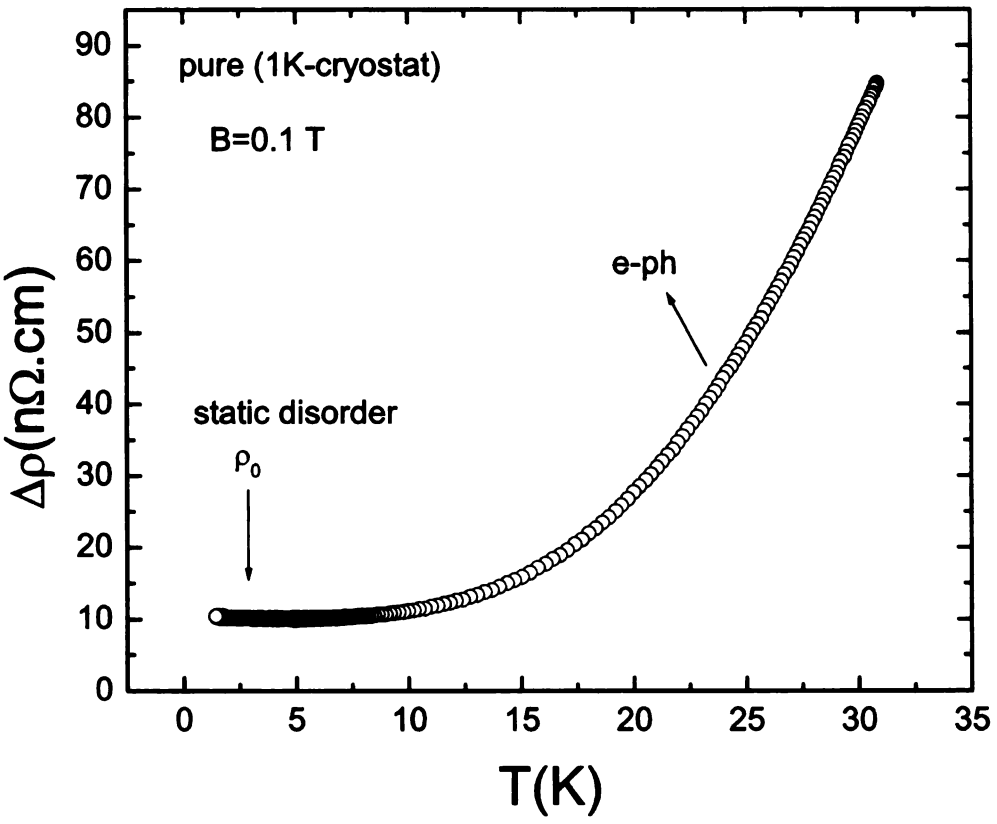

Figure 6.1: Resistivity vs temperature of puresample2 measured between 1.3 K-32 K. The resistivity was measured in a finite magnetic field of 0.1 T to suppress the weak localization magnetoristance. The data do not have the right offset, so the value of ρ_0 shown in the figure is not the correct one. To calculate ρ_0, one has to use Ohm's law, $R = \rho_0 L/wt$, where R is the measured resistance at low T, and L,w, and t are the sample dimensions.

A magnetic field of 0.1 T was applied to suppress the weak localization contribution to the resistance. As seen from the figure, the resistivity decreases monotonically with decreasing temperature and reaches a constant residual value at low temperatures ρ_0.

In the presence of a small amount of magnetic impurities, the electrical resistivity shows anomalous behavior, whereby it increases when the temperature is lowered [16]. The temperature at which the resistivity starts increasing is called the resistivity minimum, T_{min} (see figure 6.2). This minimum is due to the competition between scattering of conduction electrons by phonons dominating at high T and by magnetic impurities dominating at low T. Below the minimum, the resistivity was found

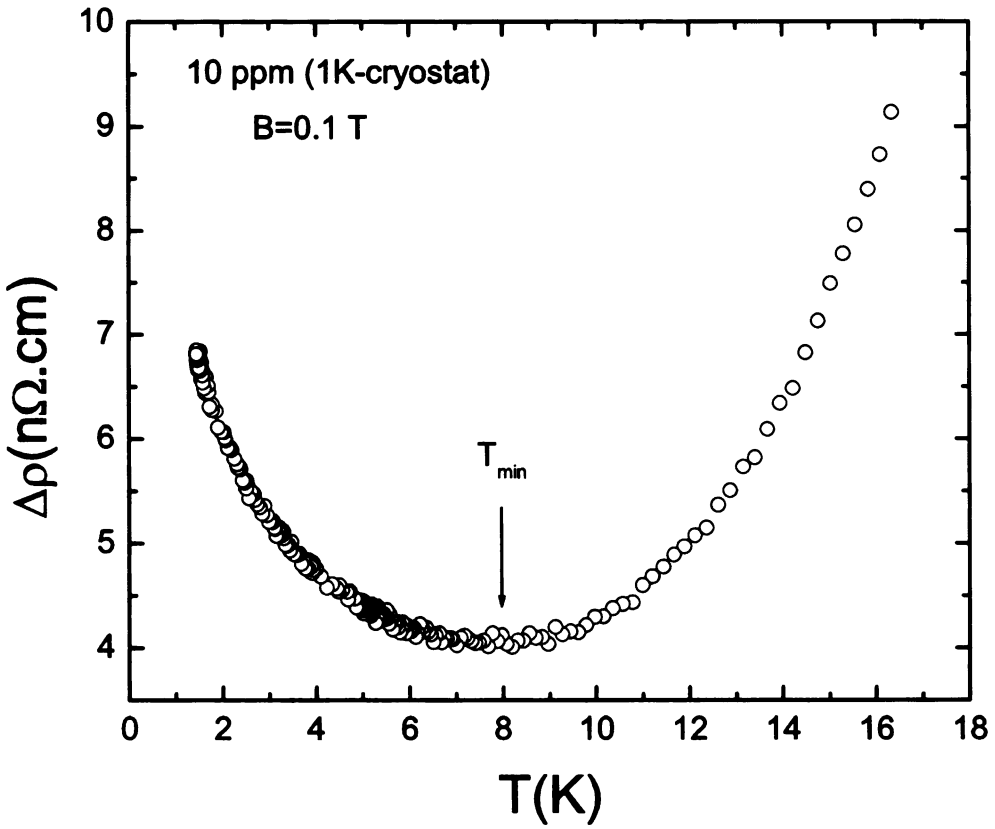

Figure 6.2: Resistivity vs temperature for 10 ppm Fe magnetic impurities in Ag measured at a finite magnetic field of 0.1T to suppress the weak localization magnetoresistance. This sample was measured in the 1K-cryostat between 1.3 K-18 K. Notice that the resistivity minimum occurs at around 8 K. The increase in the resistivity below the minimum is due to the presence of Fe magnetic impurities.

to increase logarithmically $(-\ln T)$ when the temperature is lowered. Figure (6.2) shows the electrical resistivity as a function of temperature for 10 ppm Fe magnetic impurities in Ag measured at a finite magnetic field of 0.1 T between 1.3 K-18 K. The resistivity minimum of this sample occurs around 8 K. To extract the Kondo contribution to resistivity, one has to subtract the e-ph scattering contribution to resistivity from figure (6.2). Ideally, one has to measure the same sample before and after ion-implantation to be able to subtract the e-ph contribution to the resistivity properly. However, for this sample, the e-ph contribution to resistivity was not measured before the ion-implantation. Furthermore, it was hard to compare the resistivity data of the

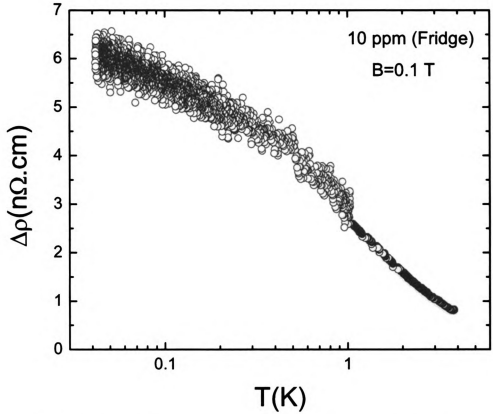

Figure 6.3: The e-e and the magnetic impurities contributions to the resistivity for the 10 ppm sample measured between 40 K - 4 K. This sample was measured in the dilution refrigerator at a finite magnetic field of 0.1 T. This magnetic field (0.1 T) is big enough to kill the weak localization (antilocalization) effects, but small enough to not polarize the magnetic impurities. The resistivity data below $\sim$ 1 K are noisy due to the fact that the voltage across the wire was limited to $eV \lesssim k_B T$, to avoid heating the electrons in the wire.

pure sample with this sample; since the two samples are totally different. Due to these reasons, we could not extract the Kondo resistivity and fit it to the empirical formulas given in reference [17] to extract the Kondo temperature,T_K.

At low temperatures (T $\lesssim$ 4 K), the e-ph contribution to the resistivity is small. On the other hand, the e-e contribution to resistivity increases with decreasing temperature, and it dominates below 1 K (see equation 2.14). Figure (6.3) shows the e-e and the magnetic impurities contributions to the resistivity for the 10 ppm sample below 4 K. The temperature dependence of the magnetic impurities contribution to

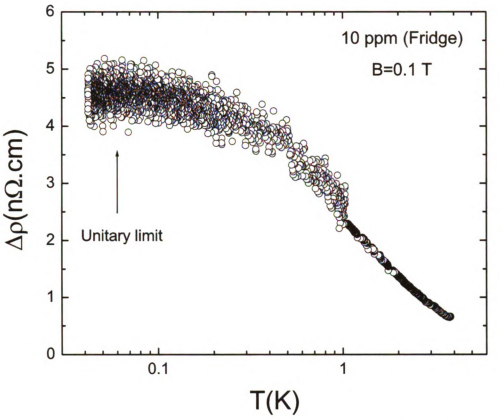

Figure 6.4: The magnetic impurities contribution to resistivity for the 10 ppm sample after subtraction of the e-e contribution to resistivity using equation (2.14). Notice that the resistivity saturates below ~ 0.2 K, approaching its unitary limit (its value at $T = 0$). The resistivity data below ~ 1 K are noisy due to the fact that the voltage across the wire was limited to $eV \lesssim k_B T$, to avoid heating the electrons in the wire.

the resistivity for the same sample (10 ppm) is shown in figure (6.4) after subtraction of the e-e contribution to resistivity using equation (2.14). This sample was measured in the dilution refrigerator at a finite magnetic field of 0.1 T between 40 mK - 4 K. This magnetic field (0.1 T) was big enough to kill the weak localization (antilocalization) effects, but small enough not to polarize the magnetic impurities. As seen from the figure, the resistivity increases with decreasing temperature down to 0.2 K and then levels off, approaching its unitary limit (its value at $T = 0$). The unitary limit observed here is a sign of the formation of the singlet state proposed by Wilson [20], where he showed that at temperatures far below the Kondo temperature ($T \ll T_K$),

the spin of the magnetic impurity is totally screened by the conduction electrons; hence the impurity becomes non-magnetic. For conduction electrons, the screened impurity appears then as a potential scattering center. The Kondo temperature is the temperature at which the Kondo resistivity drops to half its value at $T = 0$ (unitary limit [17]). The data shown in figure (6.4) have an unknown vertical offset, so we do not know where the zero is. Guessing where to assign the value $\Delta\rho = 0$ is not reliable for our samples, since the e-ph scattering contribution to resistivity starts to grow significantly when $T > 8\ K$, before the Kondo contribution has completely died out [52].

Although figures (6.2) and (6.3) are for the same sample (10 ppm) measured in two different cryostats, they do not match in the overlap temperature range. This, however, is due to the fact that the sample was initially measured in the dilution refrigerator and a few months later when the sample was measured again in the high temperature cryostat (1K-cryostat), it was found that its resistance had increased by around 50%. Therefore, our resistivity data are not reliable enough to be used to extract the Kondo temperature. Nevertheless, the resistivity data serve to show some experimental signatures of the Kondo effect such as the resistivity minimum, unitary limit, and the logarithmic rise of the resistivity below the minimum. In the following sections, we will discuss our efforts for obtaining an independent estimate of the Kondo temperature from the high field magnetoresistance.

6.3 High field magnetoresistance and NRG calculations

6.3.1 High field MR data

At high temperatures ($T \gg T_K$), the magnetic moment of the Fe impurity behaves like a free magnetic moment. Below the Kondo temperature, T_K, the magnetic moment of the Fe impurity is progressively screened by the surrounding conduction electrons as the temperature is lowered. Far below the Kondo temperature ($T \ll T_K$), the Fe impurity is completely screened; hence it behaves like a static scatterer. In this limit, the scattering of the conduction electrons by the Fe impurity is pure elastic, and the resistivity saturates towards its unitary limit. This transition from magnetic to nonmagnetic state is not a sharp transition but happens gradually. It was found that this transition results in the anomaly in the resistivity of the Kondo alloys. In the previous section, we found that for 10 ppm Fe in Ag, the resistivity saturates below 0.2 K, indicating that the unitary limit was reached below this temperature (0.2 K). In this section, we discuss the anomalies (negative MR) observed at high magnetic fields for 10 ppm Fe in Ag. Then we show how the Kondo temperature can be obtained from fitting the high field MR data to the theory of reference [58].

In a pure metallic film, the classical magnetoresistance due to the Lorentz force takes the form $\Delta R(B)/\mathrm{R} \approx (\omega_c \tau)^2$ [13], where $\omega_c = eB/m$ is the cyclotron frequency and τ is the elastic mean free time. At low magnetic fields, this classical MR is negligible. The classical B^2 dependence of one of the pure samples measured in the dilution refrigerator below 4 K is shown in figure (6.5). This is a positive magnetoresistance. The big spikes seen at $|B| < 0.03$ T are due to the weak localization magnetoresistance. The inset of the figure shows how the resistance changes with decreasing temperature at zero magnetic field. This increase in the resistance with decreasing temperature is mainly due to the contribution from e-e scattering as T is

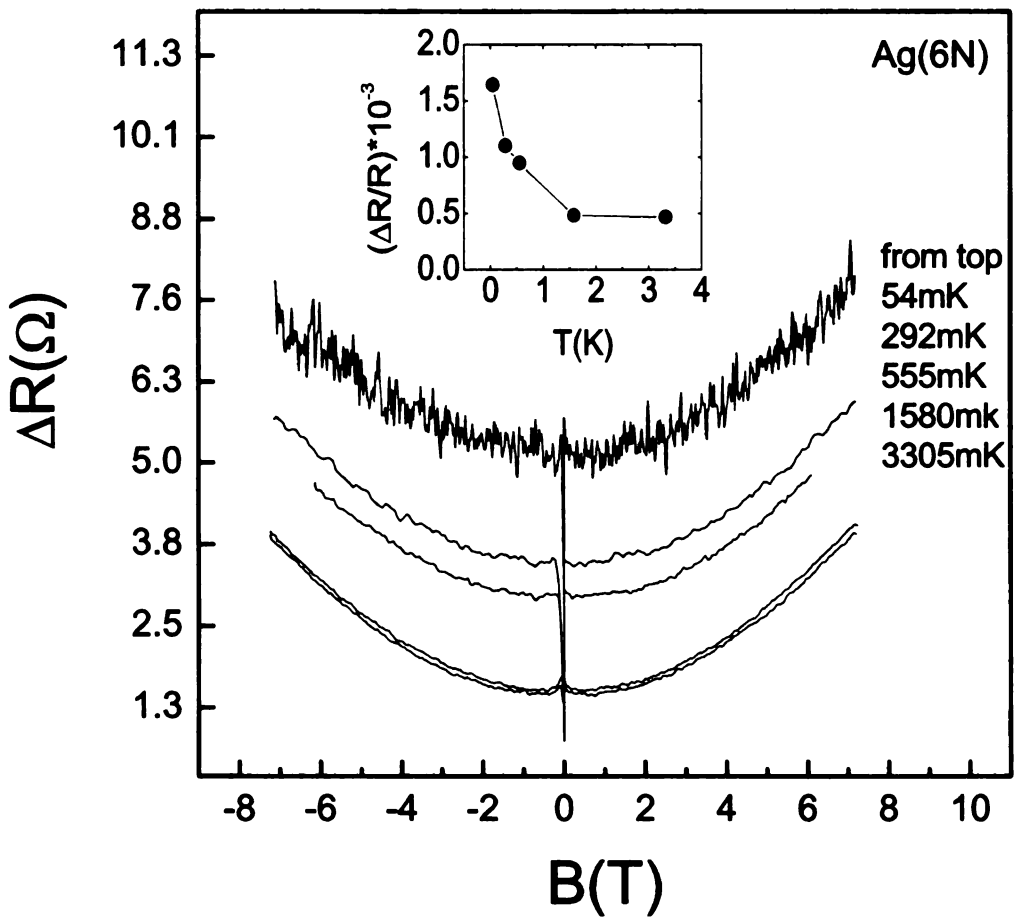

Figure 6.5: High field magnetoresistance of a pure sample measured in the dilution refrigerator between 54 mK - 3.3 K. The geometrical and electrical characteristics of this sample are: $L = 780$ μm, $t = 47$ nm, and $R = 3147$ kΩ. This wire was very rough, where its width was between 50 nm - 200 nm when measured using the SEM. Therefore, this sample will not be used in future calculations. However, it is still good to show the behavior of the classical MR in pure films. The inset shows the increase in the overall resistance with decreasing temperature at $B = 0$. This increase is mainly due to e-e interactions (see text).

lowered. In Chapter 2, we mentioned that the e-e interaction contribution to resistance takes the form $\Delta R_{ee} \propto 1/\sqrt{T}$. From this expression one can see that ΔR_{ee} dominates the temperature dependent resistivity below 1 K, consistent with what is seen in the inset of figure (6.5). Unfortunately, when this sample was later observed under the SEM, the wire was very rough, so the results of this sample will not be used in future calculations or comparisons. Nevertheless, the high field data of this sample is good for demonstration and to show the behavior of the classical MR in pure metallic wires.

Adding a small number of Fe magnetic impurities to Ag results in an anomaly in the high field data, where the magnetoresistance is now negative at an intermediate fields scale. This negative MR is totally due to the scattering of conduction electrons by Fe magnetic impurities (Kondo scattering). Figure (6.6) shows the high field magnetoresistivity data for 10 ppm Fe impurities in Ag measured in the dilution refrigerator between 83 mK - 1.88 K. Again, the spikes seen at low field are due to the weak localization magnetoresistance ($B < 0.03$ T). Notice that below 200 mK, where $\tau_\phi > \tau_{so}$, the spikes are downward, whereas above 550 mK, where $\tau_\phi < \tau_{so}$, the spikes are upward. At intermediate fields, the magnetoresistivity curves are negative. At fields bigger than 4 T, the classical magnetoresistivity dominates the Kondo scattering. This, however, is expected because at very high magnetic fields, the spins of magnetic impurities are completely polarized to the direction of the applied magnetic field; hence the magnetic moments lose their dynamics and behave like static impurities. Notice here how the peak amplitude increases with decreasing temperature, indicating that the Kondo scattering is stronger at lower temperatures. This is consistent with the Kondo effect, where the resistivity increases with decreasing temperature below T_{min}. Looking carefully at the lowest two data sets (83 mK and 188 mK), one can see that the amplitudes of magnetoresistances are almost equal, indicating that the unitary limit was reached below 200 mK, consistent with the ρ vs

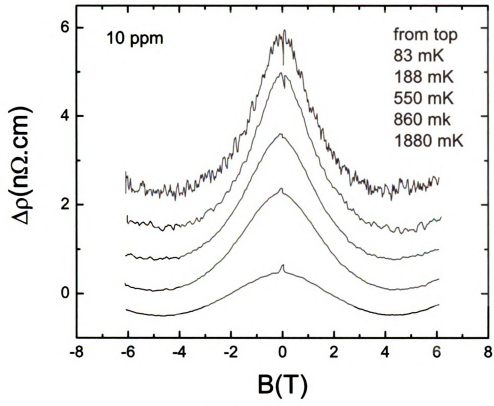

Figure 6.6: High field magnetoresistivity for 10 ppm Fe impurities in Ag measured at temperatures of 83, 188, 550, 860, and 1880 mK, from top to bottom. The last four data sets were shifted downward by 0.75 nΩ.cm relative to the 83 mK data set for clarity.

T data shown in the last section for the same sample (see figure 6.4). Actually the two data sets are identical, but for clarity all data sets for $T \geq 188$ mK were shifted downward by 0.75 nΩ.cm relative to the 83 mK data set.

At high temperatures, the Kondo scattering is less effective and dies out gradually with increasing temperature; hence the total magnetoresisitvity will be mostly classical. Figure (6.7) shows the total magnetoresisitvity vs B for the 10 ppm sample measured at 10 K. The B^2 dependence of the magnetoresisitvity is obvious. In the figure, the low-field data points were masked between -1 T $< B <$ 1 T, and the remaining points were fit to the functional form $\Delta\rho(B) = a + b(B - B_0)^2$, where a is the extrapolated value of the magnetoresisitvity at zero field ($\Delta\rho(0)$) and B_0 compen-

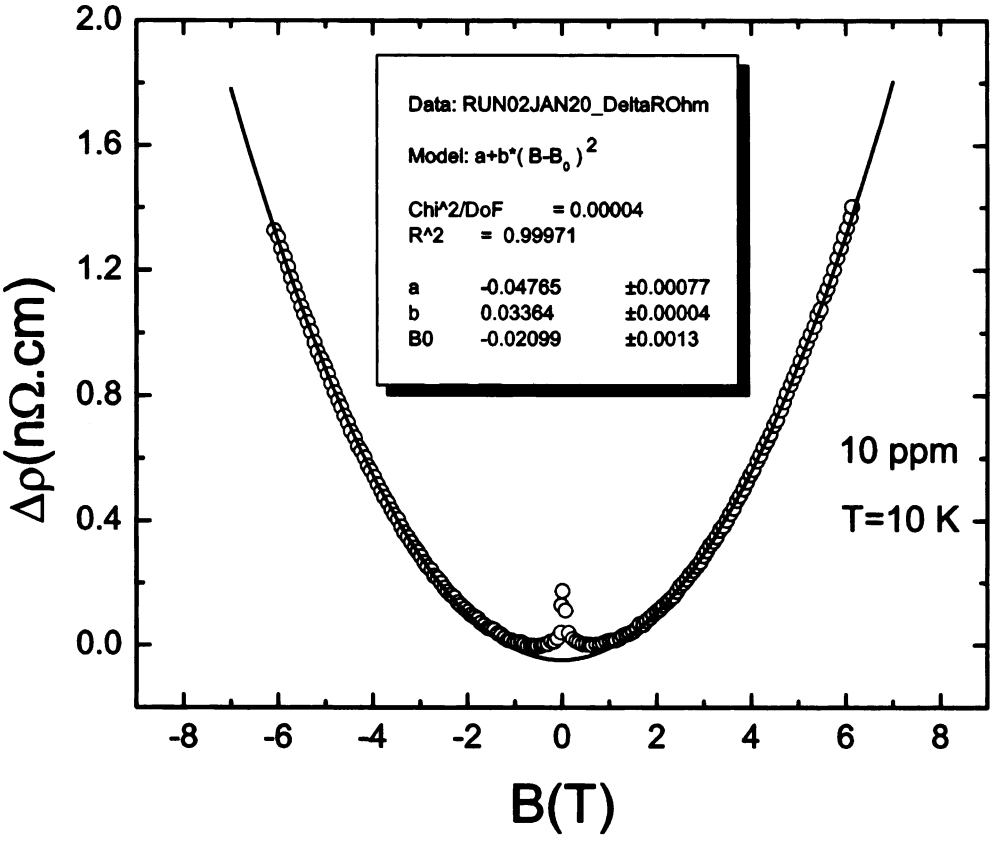

Figure 6.7: High field magnetoresistance for 10 ppm Fe impurities in Ag measured in the dilution refrigerator at 10 K. The low-field data points were masked between -1 T $< B < 1$ T, and the remaining points were fit to the functional form $\Delta\rho(B) = a + b(B - B_0)^2$, where a is the extrapolated value of the magnetoresisitvity at zero field ($\Delta\rho(0)$) and B_0 compensate for the B offset. The solid line in the figure is the fit to this functional form. The window appears in the figure shows the output of the least-square fit with a, b, and B_0 being the adjustable parameters.

sates for the small B offset due to trapped flux in the magnet. The solid line in the figure is the fit to this functional form. The window appearing in the figure shows the output of the least-square fit with a, b, and B_0 being the adjustable parameters. The value of the coefficient b will be used later to subtract the classical MR (figure 6.7) from the total MR (figure 6.6) to extract the Kondo contribution to MR. A typical subtraction example for the 83 mK data set is shown in figure (6.8). Notice that the two curves in the figure are identical between -2 T and 2 T, indicating that the classical MR is weak below fields of 2 T. Figure (6.8) shows also that the Kondo effect

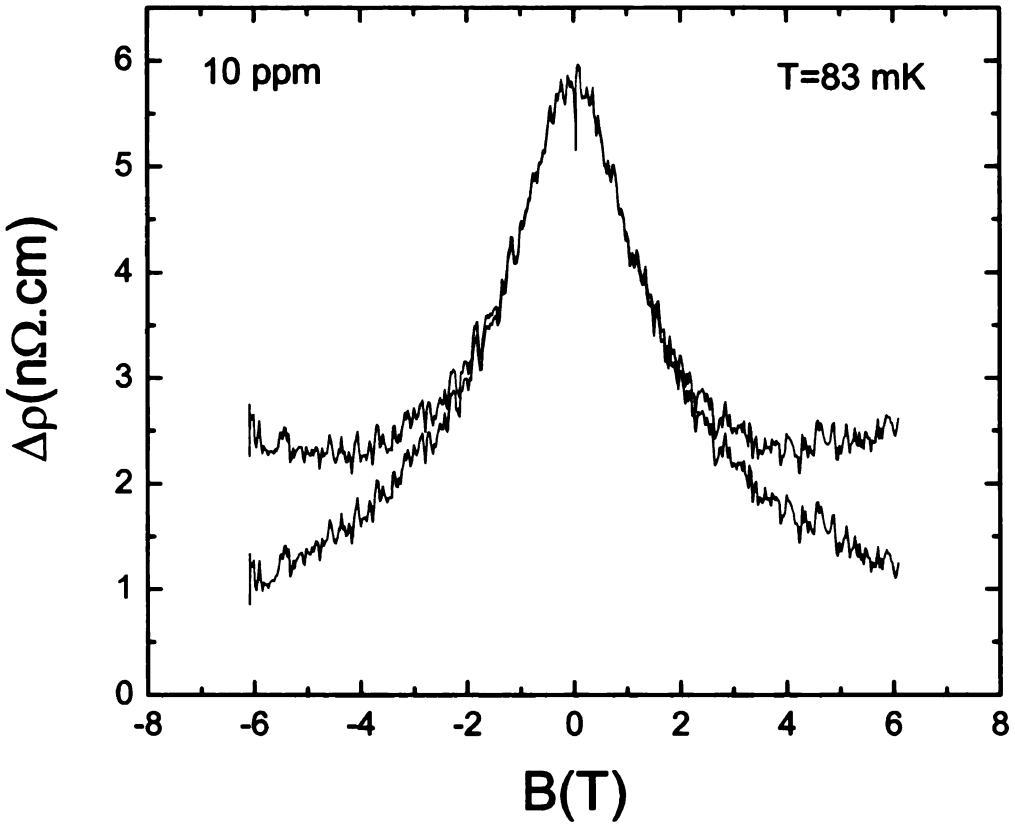

Figure 6.8: High field magnetoresistance for 10 ppm Fe impurities in Ag measured in the dilution refrigerator at 83 mK. The upper curve is the total magnetoresisitvity. The lower curve is the Kondo contribution to magnetoresisitvity, which was obtained by subtraction of the classical magnetoresisitvity (figure 6.7) from the upper curve. Notice that one needs to go to higher fields to completely polarize the Fe magnetic moments, at which the magnetoresisitvity becomes flat (field independent).

still survives in a magnetic field up to 6 T. This means that at this filed (6 T), the Fe moments are not completely polarized to the direction of the applied field, so one needs to go to higher fields to totally kill the Kondo effect.

6.3.2 Theory of Costi for high field MR in dilute Kondo alloys

The theory of Costi [58] describes the magnetic field dependence of the spectral density of a S=1/2 magnetic impurity at both zero and finite temperatures. The

total spectral density of a magnetic impurity, $A\ (\omega, T, B)$, is defined by the sum of spin up and spin down spectral densities, $A\ (\omega, T, B) = \sum_\sigma A_\sigma(\omega, T, B)$. According to this theory, the magnetic impurity contribution to the resistivity, at very small concentrations ($n_s \ll 1$), is given by [58]

$$\rho^{-1}\ (T, B) = \frac{ne^2}{2m} \sum_\sigma \int_{-\infty}^{+\infty} d\ \omega\ \tau_\sigma\ (\omega, T, B)\ (-\frac{\partial f}{\partial \omega}) \tag{6.1}$$

where $\tau_\sigma^{-1}\ (\omega, T, B) = n_s\ A_\sigma\ (\omega, T, B)$ is the inverse transport time of electrons of spin σ, f is the Fermi function, and m, n, and e are the mass, density, and charge, respectively, of the conduction electrons. At $T = 0$, $\frac{\partial f}{\partial \omega} = -\delta(\omega)$, then equation (6.1) reads

$$\rho^{-1}\ (T = 0, B) = \frac{ne^2}{2m} \sum_\sigma \int_{-\infty}^{+\infty} d\ \omega\ \tau_\sigma\ (\omega, 0, B)\ \delta(\omega) \tag{6.2}$$

$$= \frac{ne^2}{2m} \sum_\sigma \tau_\sigma\ (0, 0, B) \tag{6.3}$$

$$= \frac{ne^2}{2m}\ 2\ \tau_\uparrow\ (0, 0, B) \tag{6.4}$$

$$= \frac{ne^2}{m} \left[\frac{1}{n_s A_\uparrow\ (0, 0, B)}\right] \tag{6.5}$$

where I used $A_\uparrow\ (0, 0, B) = A_\downarrow\ (0, 0, B)$. Finally, taking the inverse of the last equation, we end up with an expression for the resistivity as a function of magnetic field calculated at $T = 0$.

$$\rho\ (0, B) = \frac{m}{ne^2}\ n_s A_\uparrow\ (0, 0, B) \tag{6.6}$$

The quantity $A_\uparrow\ (0, 0, B)$ was calculated in reference [58] using the Numerical Renormalization Group method (NRG). The results of these calculations are shown in figure (6.9). The Kondo field, B_K, is defined as the magnetic field at which the spectral function $A_\uparrow\ (0, 0, B)$, shown in figure (6.9), falls to half its value at $T = B = 0$.

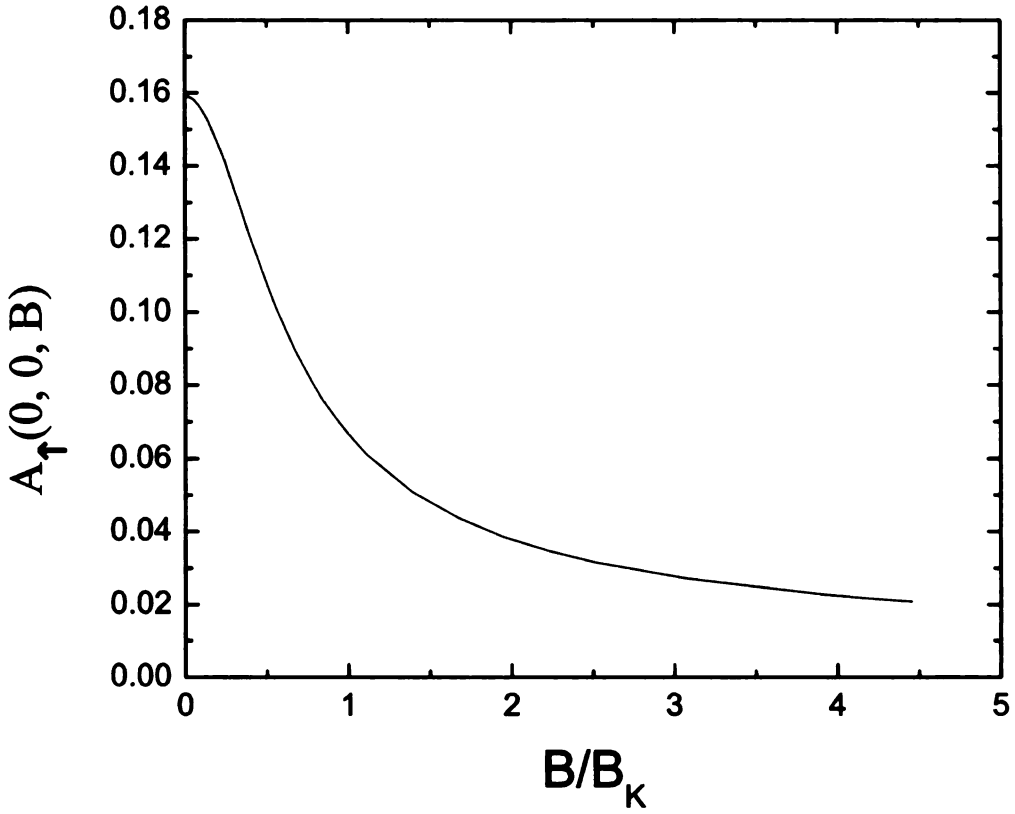

Figure 6.9: The spin up spectral density function, $A_\uparrow\ (0, 0, B)$, vs magnetic field B calculated at $T = 0$ using NRG method. The x-axis is normalized to the parameter B_K, which is related to T_K by $T_K \approx 1.34\ B_K$. The data in the figure were provided by the author of reference [58].

The x-axis of figure (6.9) is normalized to the parameter B_K, which is related to T_K by $g\mu_B B_K = k_B T_K$, where μ_B is the Bohr magneton. Using $g = 2$ and $\mu_B/k_B \approx 0.67\ \text{K.T}^{-1}$, this reads $T_K(\text{K}) \approx 1.34\ B_K(\text{T})$. Here, I want to emphasize again that the numerical calculations shown in figure (6.9) are valid only at $T = 0$. Nevertheless, our resistivity data for 10 ppm Fe impurities in Ag show that the resistivity saturates below 0.2 K, approaching its unitary limit (its value at $T = 0$); hence we can, in principle, fit our lowest temperature high field MR data set, 83 mK, to this model. The following subsection will discuss this fit.

6.3.3 Fitting the 83 mK high field data set to theory of Costi

In this section, we fit the high field magnetoresistivity data of the 83 mK data set using the NRG calculations of reference [58]. As mentioned earlier, below 0.2 K the resistivity of the 10 ppm sample saturates towards its unitary limit. Therefore, below 0.2 K, the high field data of the 83 mK data set are expected to be nearly identical to the $T = 0$ analytical solution of reference [58]. The solid line in figure (6.10) shows the fit of our 83 mK data set to the theory of Costi [58] using the functional form $\Delta\rho(B) = \Delta\rho_{\rm K}\, f(B/B_{\rm K})$, where $\Delta\rho_K \equiv \rho(B = 0, T = 0) - \rho(B \gg B_K, T = 0)$ and $B_{\rm K}$ is the magnetic field at which the magnetoresisitvity falls to its half value at $B = 0$ (i.e $1/2\ \Delta\rho(0)$). The data set were fit with two adjustable parameters, $\Delta\rho_{\rm K}$ and $B_{\rm K}$. The result of the fit gives the values $\Delta\rho_{\rm K} = 0.57$ nΩcm/ppm and $B_{\rm K} = 1.2$ T, which in turn gives $\rm T_K = 1.6$ K [52]. This value of $T_{\rm K}$ is considerably lower than the value of $T_{\rm K} \approx 5$ K obtained from the fit to γ_m, discussed in Chapter 5.

The expected value of the unitary limit for s-wave ($l = 0$) scattering is given by $\Delta\rho_K = 4\pi\hbar n_s/ne^2k_F$ [59], where n_s is the concentration of magnetic impurities, and n and k_F are the density and the Fermi wave number of the host, respectively. The d-wave unitary limit is 5 times the s-wave unitary limit. The factor 5 comes from $(2l + 1)$, where $l = 2$ for the d-waves. In a Ag host, where $k_F = 1.2 \times 10^{10}\ m^{-1}$, the s-wave unitary limit is $\Delta\rho_{\rm K} = 0.43$ nΩcm/ppm. Our measured value of $\Delta\rho_{\rm K} = 0.57$ nΩcm/ppm is larger than the theoretical s-wave value, but smaller than the measured values in other Fe-noble metal Kondo systems: 1.3 nΩcm/ppm in Cu:Fe and 1.0 nΩcm/ppm in Au:Fe [60].

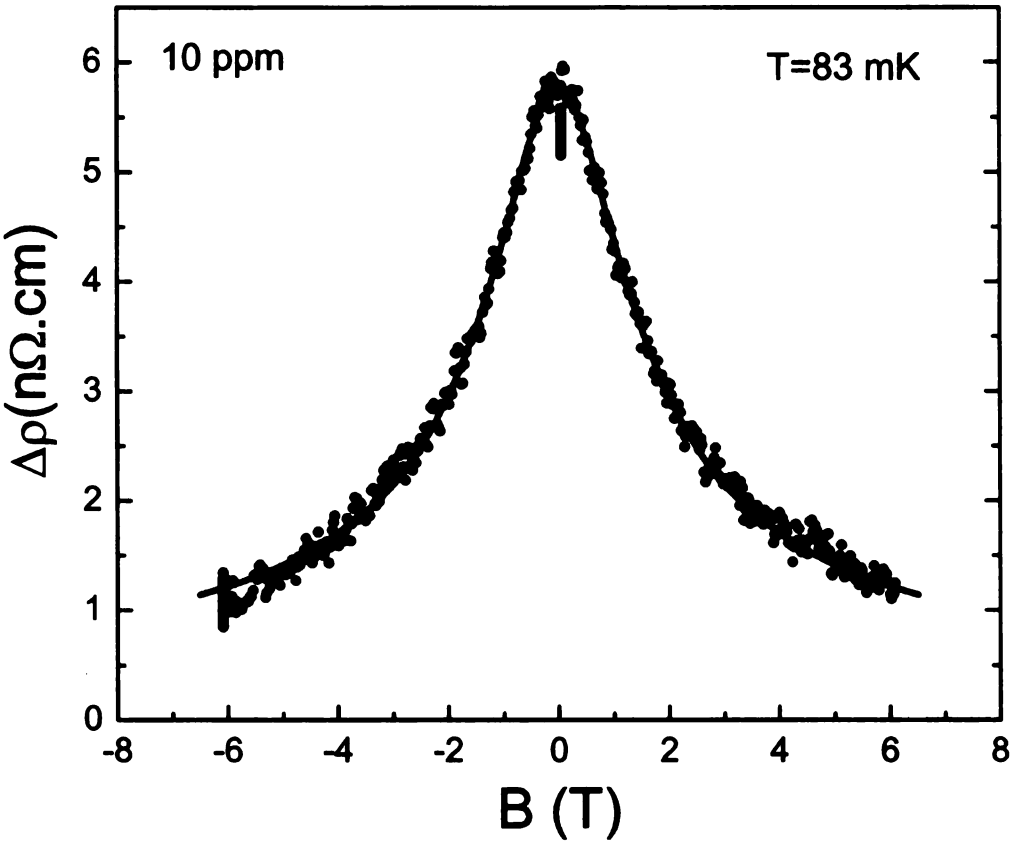

Figure 6.10: Kondo contribution to magnetoresistivity for 10 ppm Fe impurities in Ag measured in the dilution refrigerator at 83 mK. The data were obtained after subtraction of the classical magnetoresisitvity (figure 6.7). The solid line is the fit to reference [58].

6.3.4 Fitting the high temperature MR data sets to theory of Costi

The high field NRG calculations shown in figure (6.9) were good enough to fit the lowest MR data set, 83 mK, since it is close to the unitary limit. However, this approximation is no longer valid at high temperatures ($T > 0.2$ K); hence more NRG calculations at higher temperatures were necessary to fit our high field MR data. Upon our request, the high temperature NRG calculations were provided to us by the author of reference [58] (not shown in this thesis). We tried to fit our high field MR data to these calculations, while fixing $\Delta\rho_K$ to its unitary limit ($\Delta\rho_K = 0.57$ nΩcm/ppm),

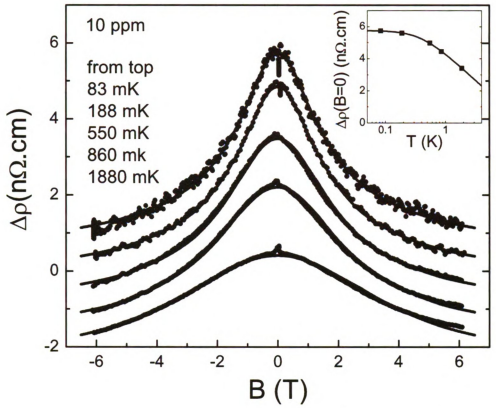

Figure 6.11: Kondo contribution to magnetoresistivity for the 10 ppm sample with fits to the spin-1/2 NRG theory from [58], as discussed in the text. The zero for the 83 mK data is chosen so that the fit curve approaches $\Delta\rho \to 0$ for $|B| \gg B_K$. Subsequent data sets are shifted downward by 0.75 nΩcm for clarity. Top right inset: $\Delta\rho(B = 0)$ vs. temperature [52].

but unfortunately we could not fit them consistently with such a low value of T_K = 1.6 K. The problem is that the temperature scale over which the high-field MR decreases is much larger than the value 1.6 K obtained from the field dependence at $T = 0$. Instead, we have performed a global fit to all the $\rho(B)$ data sets using the functional form $\Delta\rho(B,T) = \Delta\rho_K\, f(T/T_K, B/B_K)$, with only three parameters: $\Delta\rho_K$, B_K, and T_K. The parameter B_K determines the magnetic field scale over which $\rho(B)$ decreases and the parameter T_K determines the temperature scale over which $\rho(B = 0)$ decreases. The solid lines in figure (6.11) are the results of this global fit, with the values B_K = 1.36 T, T_K = 2.96 K, and $\Delta\rho_K$ = 0.58 nΩcm/ppm [52]. The value of

B_K corresponds to a Kondo temperature of 1.8 K, which is close to the $T_K = 1.6$ K obtained from fitting the 83 mK data set alone to the $T = 0$ NRG calculations (see figure 6.10). The Kondo temperature extracted from the temperature scale (2.96 K) is almost twice as that extracted from the field scale (1.8 K).

The discrepancy between the values of T_K extracted from the field scale (1.8 K) and from the temperature scale (2.96 K) highlights the fact that we are using a spin-1/2 theory. In a metal containing small amount of magnetic impurities without Kondo effect, the magnetoresistance is proportional to $- < M_z >^2$, where $< M_z >= N\mu B_J(x)$ is the average magnetization of the system, N is the total number of magnetic impurities, $\mu = g\mu_B J$ with $J = L + S$ being the total angular momentum of the localized moment, and $B_J(x)$ is the Brillouin function given by [61]

$$B_J(x) = \left(1 + \frac{1}{2J}\right) \coth\left[\left(1 + \frac{1}{2J}\right) x\right] - \frac{1}{2J} \coth\left[\frac{1}{2J} x\right] \tag{6.7}$$

where $x = g\mu_B JB/k_B T$ is the Zeeman energy of the local moment in the external field B in units of $k_B T$. The Brillouin function is normalized and varies between 0 and 1. Figure (6.12) shows the calculated magnetoresistance using the function $1 - B_J^2(x')$ for both $S = 1/2$ and $S = 2$, where the function $B_J(x')$ is given by

$$B_J(x') = \left(1 + \frac{1}{2J}\right) \coth\left[\left(J + \frac{1}{2}\right) x'\right] - \frac{1}{2J} \coth\left[\frac{1}{2} x'\right] \tag{6.8}$$

with $x' = g\mu_B B/k_B T$.

In this figure, it is assumed that the total angular moment of the localized moment is due to its spin only, $L = 0$. As seen from the figure, the full width at half maximum of the MR curve with $S = 1/2$ is 1.85 times larger than that with $S = 2$. If a similar relationship holds for the $\rho(B)$ curves in the Kondo regime, then the value $B_K = 1.2$T we found from the s=1/2 fit to the 83 mK data would become $B_K \approx 2.2$ T for s=2, which corresponds to a Kondo temperature $T_K = 3.0$ K [52]. That is consistent with

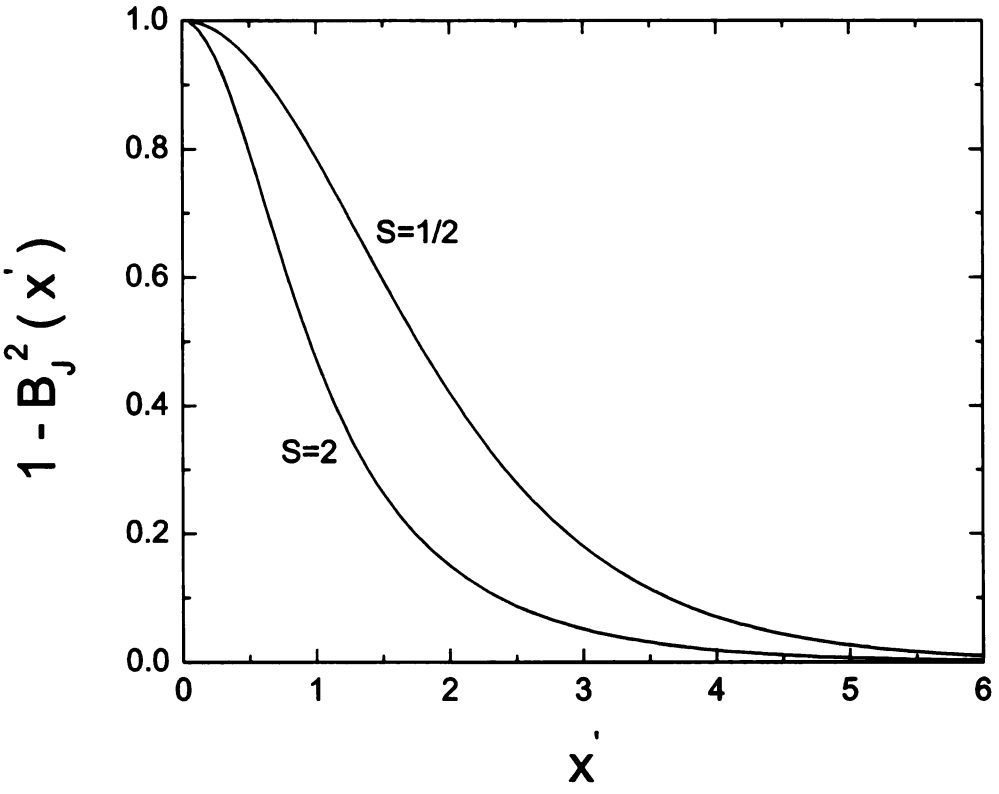

Figure 6.12: Magnetoresistance of a system of magnetic impurities calculated using equation (6.8). In this figure, we assume, for simplicity, that $N = \mu_B = g = 1$, and $L = 0$. Notice that the full width at half maximum of the MR curve with $S = 1/2$ is 1.85 times larger than that with $S = 2$. Notice also that at high fields, the magnetoresistance saturates with the magnetic moments completely aligned with the applied field.

the value of T_K obtained from the temperature dependence of $\rho(B = 0)$, but still lower than the value $T_K \approx 5$ K obtained from the fit to γ_m.

Recently, Mallet *et al.* [56] reported measurements of resistivity and phase coherence in three Ag wires implanted with Fe impurities. The implanted ion concentrations were 1.3, 13, and 33 ppm, respectively. From fitting the resistivity data to the NRG theory for spin 1/2 magnetic impurities, they also obtained a Kondo temperature of $T_K = 3$ K. However, the unitary limit observed in their implanted samples was an order of magnitude less than the expected value of the s-wave unitary limit for this system ($\Delta\rho_K = 0.43$ nΩ.cm/ppm). Their phase coherence results were similar

to ours, where they found a Kondo temperature of $T_K \approx 4.3$ K and observed a low T deviation from theory in the γ_m.

In summary, the Kondo temperature obtained from the resistivity, $T_K \approx 3.0\ K$, is somewhat lower than the Kondo temperature obtained from the dephasing data, $T_K \approx 4.3\ K$ by Mallet *et al.* [56], or $T_K \approx 4.8 - 5.4\ K$ by us [52].

Chapter 7

Conclusions

7.1 Overview

The topic of electron phase coherence in metals at low temperature has been controversial in the past decade. It is important to understand the role of dilute magnetic impurities in this context. In this work, we have studied the inelastic scattering mechanisms of conduction electrons in AgFe Kondo alloys. The concentration of the Fe impurities was very small such that these alloys lie in the regime of the Kondo effect (single impurity limit). The goal of this work was to study the temperature dependence of the magnetic scattering rate, γ_m, not too far below the Kondo temperature, T_K. As discussed in Chapter 1, at the time we started this work, there was neither experimental data nor theory to describe the intermediate regime for T not too far below T_K (see figure 1.5). To study the temperature dependence of γ_m, it was important to have a system with T_K below 8 K, otherwise the Kondo effect would be masked by the e-ph interactions. On the other hand, it was necessary to keep T_K as high as possible to be able to acquire data below T_K. The best Kondo system for this study, then, should have a Kondo temperature between 2 - 5 K. The AgFe system was a good candidate to study the temperature dependence of γ_m; since it has a relatively high $T_K \approx 5$ K. In this work, two types of samples were studied, pure and implanted

samples. It was necessary to perform measurements on both types of samples to be able to extract the effect of adding Fe impurities on the transport properties of our Kondo system.

7.2 Summary of Results

7.2.1 Phase Coherence Results

In this study, we have used the method of weak localization magnetoresistance to measure the total dephasing rate in AgFe Kondo wires. By measuring the weak localization magnetoresistance between 40 mK - 18 K , we were able to indirectly measure the phase coherence length L_ϕ, and hence τ_ϕ. The magnetic scattering rate of the implanted samples, γ_m, was obtained by subtraction of the total dephasing rate of the pure sample from the total dephasing rate of the the implanted samples. The γ_m data were fitted using the Numerical Renormalization Group (NRG) calculations of reference [27]. From the fit, we found that the theory of reference [27] fits the γ_m data resonably well over the temperature range $T/T_K = 0.1 - 2$ [52] (see figure 5.11). Above the Kondo temperature, $T_K \approx 5$ K, the γ_m data were almost constant, consistent with the prediction of reference [27]. The maximum value of γ_m, occurring at $T = T_K$, was almost twice as large as that predicted by theory. Around T_K, the γ_m data has a broad maximum. Below T_K, the γ_m data were found to vary linearly in T. For $T/T_K < 0.1$, we found that the NRG theory of reference [27] deviates strongly from the γ_m data, where the temperature dependence of γ_m was found to be much weaker than that predicted by theory. The T^2 dependence of γ_m was not reached down to the lowest accessible temperatures.

The factor 2 discrepancy in the overall magnetic scattering rate was attributed to the inadequacy of the spin 1/2 theory of reference [27]. As mentioned earlier, the theory of reference [27] was developed for spin 1/2 magnetic impurities in the context

of the single- channel Kondo model ($n = 1$). The strong deviation between theory and experiment for For $T/T_K < 0.1$, could be due to the finite cross-section size of our wires [57]. Further calculations of the magnetic scattering rate due to dilute magnetic impurities with $S > 1/2$ and $n > 1$ might resolve the observed discrepancy between theory and experiment.

7.2.2 High Field Results

To obtain an independent estimate of T_K, we have measured the high field magnetoresistance of the 10 ppm sample in a magnetic fields up to 6 Tesla. The high field MR data were taken between 83 mK - 1.8 K. At an intermediate field scale, the MR data of the 10 ppm sample was found to be negative (see figure 6.6), whereas in the pure films it was positive (see figure 6.5). The negative MR observed in the 10 ppm sample was attributed to the presence of Fe magnetic impurities. From the high field MR data, we found that the unitary limit was reached below 200 mK, indicating that the Fe spin is completely screened by the surrounding conduction electrons; hence the Fe impurity behaves like a static impurity and does not contribute to dephasing processes.

We have fitted our high field MR data of the 10 ppm sample using the the Numerical Renormalization Group (NRG) calculations of reference [58] (see figure 6.10). The theory of reference [58] was also developed for spin 1/2 magnetic impurities. From the fit, we found that the measured value of the unitary limit was $\Delta\rho_K = 0.58$ nΩcm/ppm [52], which is close to the theoretical value for s-wave scattering, $\Delta\rho_K = 0.43$ nΩcm/ppm. The value of the Kondo temperature, T_K, extracted from the fit to the $T = 0$ theory ($T_K \approx 1.6$ K), was found to be smaller than that obtained from the fit to γ_m data ($T_K \approx 5$ K). Again, we attribute the discrepancy between the value of T_K obtained from fitting the γ_m data and that T_K obtained from fitting γ_m data to the inadequacy of the spin 1/2 theories. Estimating the effect of

S=2 by comparing the Brillouin function for S=1/2 and S=2 led us to an estimate $T_K \approx 3.0\ K$, which is consistent with the temperature dependence of the high-field MR data. Future calculations of the Kondo contribution to MR with $S > 1/2$ would be very helpful.

7.3 Future work

The two theories used in this work to analyze our experimental data for both phase coherence and high field MR were mainly developed for spin 1/2 magnetic impurities in the context of single channel ($n = 1$) Kondo model. In reality, the Fe has bigger spin, $S = 2$, which is quite different from $S = 1/2$. New calculations of the inelastic scattering cross-section, due to magnetic impurities with $S > 1/2$ and in the context of multi-channel Kondo model ($n > 1$), might resolve the observed discrepancies between experiment and theory. However, for $n > 1$ one faces a multi-channel Kondo problem which is much more difficult to track numerically [62]. As discussed earlier, Pedro Schlottmann thinks that the weak temperature dependence of our γ_m data observed at very low T might be due to the finite cross-section size of our wires [57]. To test this hypothesis, one has to measure τ_ϕ for films with bigger dimensionality. However, measuring τ_ϕ in thicker films using the method of weak localization magnetoresistance is hard to achieve because the weak localization signal becomes smaller as the sample dimensionality increases.

References

[1] B. Altshuler, A. Aronov, and D. Khmelnitsky, J.Phys. C **15**, 7367 (1982).

[2] S.Wind, M. Rooks, V. Chandrasekhar, and D. Prober, Phys.Rev. Lett **57**, 633 (1986).

[3] P. Echternach, M. Gershenson, H. Bozler, A. Bogdanov, and B. Nilsson, Phys. Rev. B **48**, 11516 (1993).

[4] P. Mohanty, E. Jariwala, and R. A. Webb, Phys.Rev. Lett **78**, 3366 (1997).

[5] F. Pierre, A. B. Gougam, A. Anthore, H. Pothier, D. Esteve, and N. O. Birge, Phys. Rev. B **68**, 085413 (2003).

[6] D. Golubev and A. Zaikin, Phys.Rev. Lett **81**, 1074 (1998).

[7] D. Golubev, A. Zaikin, and G. Schon, J. Low Temp. Phys **126**, 1355 (2002).

[8] D. Golubev and A. Zaikin, J. Low Temp. Phys **132**, 11 (2003).

[9] A. Zawadowski, J. von Delft, and D. Ralph, Phys.Rev. Lett **83**, 2632 (1999).

[10] Y. Imry, H. Fukuyama, and P. Schwab, Europhys. Lett **47**, 608 (1999).

[11] I. Aleiner, B. Altshuler, and M. Gershenson, Waves Random Media **9**, 201 (1999).

[12] F. Marquardt, J. von Delft, R. A. Smith, and V. Ambegaokar, cond-matt/0510556v1 (2005).

[13] N. W. Ashcroft and N. D. Mermin, *Solid State Physics* (Harcourt Brace College Publishers, Fort Worth, 1976).

[14] W. de Haas, J. de Boer, and G. van den Berg, Physica **1**, 1115 (1934).

[15] J. Franck, F. Manchester, and D. Martin, Proc. Roy. Soc. (London) **A263**, 494 (1961).

[16] J. Kondo, Prog. Theor. Phys **32**, 37 (1964).

[17] H. Suhl, *Magnetism, vol.5* (Academic Press, New York and London, 1973).

[18] A. Hewson, *The Kondo Problem to Heavy Fermions* (Cambridge University Press, Cambridge, 1997).

[19] P. Anderson, J. Phys. C:solid st.phys **3**, 2436 (1970).

[20] K. Wilson, Rev. Mod. Phys **47**, 773 (1975).

[21] C. V. Haesendonck, J. Vranken, and Y. Bruynseraede, Phys.Rev. Lett **58**, 1968 (1987).

[22] R. Peters, G. Bergmann, , and R. Mueller, Phys.Rev. Lett **58**, 1964 (1987).

[23] P. Mohanty and R. Webb, Phys.Rev. Lett **84**, 4481 (2000).

[24] F. Schopfer, C. Bauerle, W. Rabaud, and L. Saminadayar, Phys.Rev. Lett **90**, 056801 (2003).

[25] P. Nozieres, J. Low Temp. Phys **17**, 31 (1974).

[26] M. Vavilov and L. Glazman, Phys. Rev. B **67**, 115310 (2003).

[27] T. Micklitz, A. Altland, T. A. Costi, and A. Rosch, Phys.Rev. Lett **96**, 226601 (2006).

[28] G. Zarand, L. Borda, J. von Delft, and N. Andrei, Phys.Rev. Lett **93**, 107204 (2004).

[29] P. Sacramento and P. Schlottmann, Physica B **171**, 122 (1991).

[30] Y. Imry, *Introduction to Mesoscopic Physics* (Oxford University Press, Inc, New York, 1997).

[31] S. Datta, *Electronic Transport in Mesoscopic Systems* (Cambridge University Press, Cambridge, 1995).

[32] G. Bergmann, Solid State Communication **42**, 815 (1982).

[33] S. Hikami, A. I. Larkin, and Y. Nagaoka, Prog. Theor. Phys **63**, 707 (1980).

[34] S. Chakravarty and A. Schmid, Phys. Rep **140**, 193 (1986).

[35] B. Huard, Limits and effects of coherence in conductors, PhD thesis (2005).

[36] R. Meservey and P. M. Tedrow, Phys. Rev. Lett **41**, 805 (1978).

[37] B. Kramer, *Quantum Coherence in Mesoscopic Systems* (Plenum Press, New York, 1990).

[38] J. J. Lin and J. P. Bird, J. Phys.: Condens. Matter **14**, R501 (2002).

[39] A. Sergeev and V. Mitin, Phys. Rev. B **61**, 6041 (2000).

[40] S.Gasiorowicz, *Quantum Physics* (John Wiley and Sons, INC, New York, 1974).

[41] E.Merzbacher, *Quantum Mechanics* (John Wiley and Sons, INC, New York, 1998).

[42] E. Bauer, A script for a lecture given at the Vienna University of Technology, summer semester (2006).

[43] V. Fal'ko, JETP Lett **53**, 340 (1991).

[44] J.A.Mydosh, *Spin glasses* (Taylor and Francis, London.Washington.DC, 1993).

[45] M. Ruderman and C. Kittel, Phys. Rev **96**, 99 (1954).

[46] T. Kasuya, Prog. Theor. Phys **16**, 45 (1956).

[47] K. Yosida, Phys. Rev **106**, 893 (1957).

[48] M. Vavilov, L. Glazman, , and A. Larkin, Phys. Rev. B **68**, 075119 (2003).

[49] P.R.Choudhury, *Microlithography, Micromachining, and Microfabrication* (SPIE press IEE, Washington, 1997).

[50] Nanometer Pattern Generation System version 7.5 User Manual (1996).

[51] O.V.Lounasmaa, *Experimental principles and methods below 1 K* (Academic Press, New York, 1974).

[52] G. Alzoubi and N. Birge, Phys. Rev. Lett **97**, 226803 (2006).

[53] G. Bergmann, Physics Reports **107**, 1 (1984).

[54] C. Bauerle, F. M. and1 F. Schopfer, D. Mailly, G. Eska, and L. Saminadayar, Phys.Rev. Lett **95**, 266805 (2005).

[55] W. Koller, A. Hewson, and D. Meyer, Phys. Rev. B **72**, 045117 (2005).

[56] F. Mallet, J. Ericsson, D. Mailly, S. Unlubayir, D. Reuter, A. Melnikov, A. Wieck, T. Micklitz, A. Rosch, T. Costi, L. Saminadayar, and C. Bauerle, Phys. Rev. Lett **97**, 226804 (2006).

[57] P. Schlottmann, Private Communication.

[58] T. Costi, Phys.Rev. Lett **85**, 1504 (2000).

[59] D. R. Hamann, Phys. Rev **158**, 570 (1967).

[60] J. Loram, T. Whall, and P. Ford, Phys. Rev. B **2**, 857 (1970).

[61] R. Pathria, *Statistical Mechanics* (Pergamon Press Ltd, England, 1972).

[62] A. Rosch, Private Communication.